Surface-Controlled Mechanical Properties of Bulk Nanoporous Gold

Nadiia Mameka

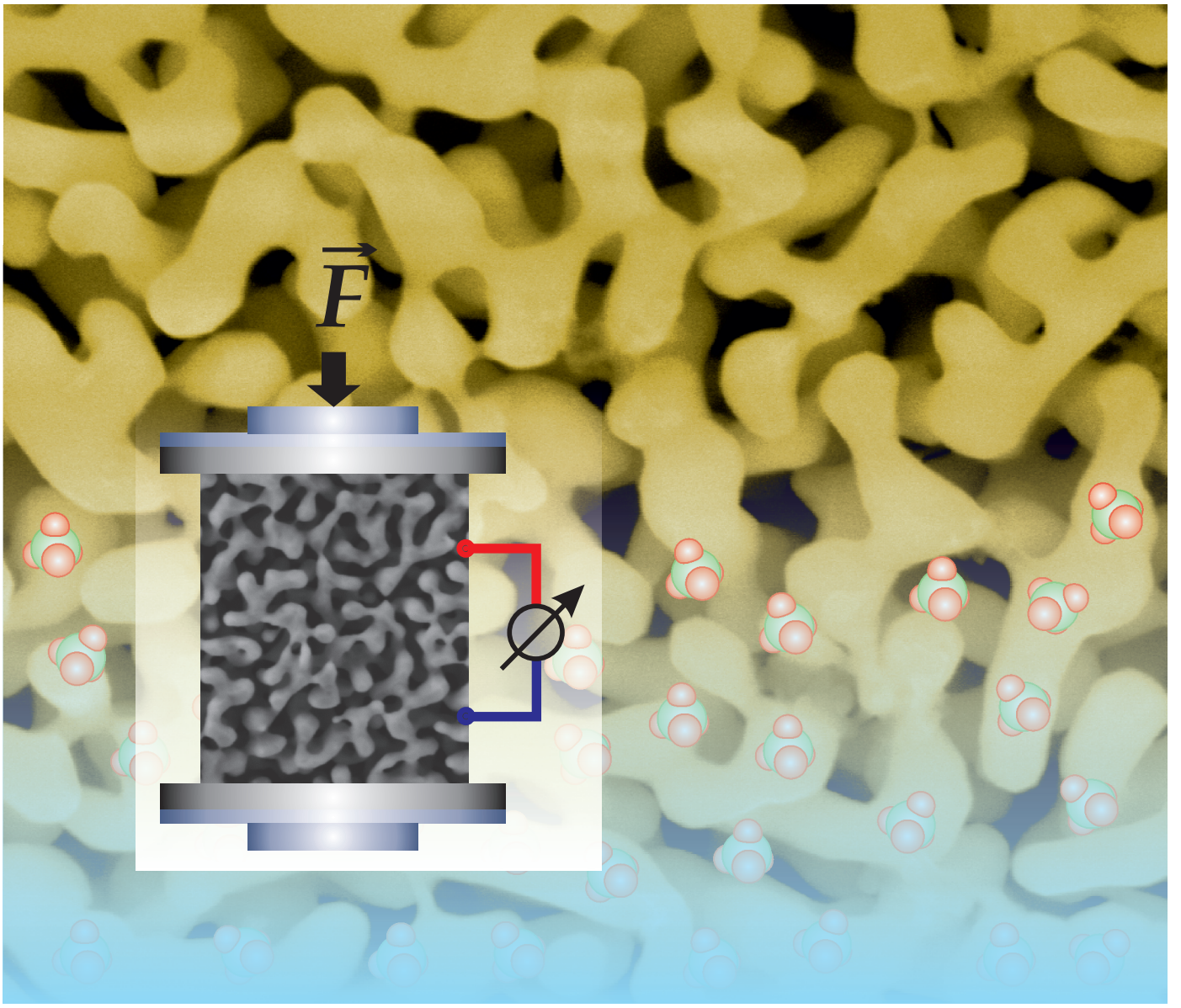

Helmholtz-Zentrum Geesthacht
Zentrum für Material- und Küstenforschung

TUHH
Technische Universität Hamburg

Surface-controlled mechanical properties of bulk nanoporous gold

Vom Promotionsausschuss der
Technischen Universität Hamburg-Harburg
zur Erlangung des akademischen Grades
Doktor-Ingenieurin (Dr.-Ing.)
genehmigte Dissertation

von

Nadiia Mameka

2016

Promotionskommission

Erstgutachter: *Prof. Dr. Jörg Weissmüller, Technische Universität Hamburg-Harburg*

Zweitgutachter: *Prof. Dr. Rainer Birringer, Universität des Saarlandes*

Vorsitzender: *Prof. Dr. Otto von Estorff, Technische Universität Hamburg-Harburg*

Tag der mündlichen Prüfung: *17. November 2015*

Umschlag: *Nadiia Mameka*

Online Veröffentlichung durch TUBdok der TUHH:
urn:nbn:de:gbv:830-88214878

Abstract

This study highlights a smart hybrid material based on nanoporous gold in an aqueous electrolyte whose stiffness and strength are reversibly tuned by external stimuli. The tunability of these effective mechanical properties is realized via application of electric potentials to the large gold-electrolyte interface of the material, and consequent control of the surface state through electrical polarization and adsorption. The experiments are implemented *in situ* under environmental control in a dynamic mechanical analyzer and a mechanical testing device. Novel and interesting findings in the mechanics of the nanoporous metal have been revealed.

First, the effective elastic modulus varies reversibly with the electrode potential by up to 10%. It is found that adsorption of oxygen species as well as a simple excess of electrons on the surface increase the stiffness while oxygen desorption/electron depletion enhance the compliance. Since the electrochemical modification affects the material exclusively at its surface, the changes in the effective elastic response unambiguously testify to the surface excess elasticity phenomena in nanomaterials.

Second, *in situ* compression tests in electrolyte suggest a similar effect of the electrode potential on the flow stress, where the relative variation reached up to 100%. The implications of microstructural size and electrochemical environment on these aspects of the material's mechanical behavior is analyzed and discussed. The observations point towards surface tension as the most relevant parameter in controlling the plasticity of nanoporous gold.

Zusammenfassung

In dieser Arbeit wird ein intelligentes Hybridmaterial auf Basis von nanoporösen Gold in einem wässrigen Elektrolyt vorgestellt, dessen Steifigkeit und Festigkeit reversibel durch externe Signale eingestellt werden können. Die Durchstimmbarkeit dieser effektiven mechanischen Eigenschaften wird über das Anlegen von elektrischen Potentialen an der großen Gold-Elektrolyt Grenzfläche innerhalb des Werkstoffes realisiert. Auf diese Art lässt sich der Oberflächenzustand durch elektrische Polarisation und Ionensadsorption kontrollieren. Die Verformungsexperimente wurden *in situ* in einer elektrochemischen Zelle, eingebaut in einen dynamisch-mechanischen Analysator und in einer mechanischen Prüfmaschine, durchgeführt. Neuartige und interessante Befunde über die Mechanik von nanoporösen Metallen wurden entdeckt.

Erstens variiert der effektive Elastizitätsmodul reversibel mit dem Elektrodenpotential um bis zu 10%. Es wurde festgestellt, dass die Adsorption von Sauerstoff sowie ein Elektronenüberschuss auf der Oberfläche die Steifigkeit erhöht während Sauerstoffdesorption und Elektronenabreicherung die Nachgiebigkeit verbessern. Da die elektrochemische Modifizierung des Werkstoffes ausschließlich an seiner Oberfläche stattfindet, zeigen die Änderungen der effektiven elastischen Reaktionen eindeutig die Auswirkungen von Oberflächenexzesselastizität in Nanomaterialien.

Zweitens legen *in situ* Kompressionstests in einem Elektrolyt eine ähnliche Wirkung des Elektrodenpotenzials auf die Fließspannung dar, wobei die relative Variation Werte von bis zu 100% erreichen kann. Der Zusammenhang zwischen der Mikrostrukturgröße und der elektrochemischen Umgebung auf diese Aspekte des mechanischen Verhaltens des Werkstoffes wurden analysiert und diskutiert. Die Beobachtungen deuten darauf hin, dass die Oberflächenspannung der relevante Parameter bezüglich der Auswirkung des Oberflächenpotentials auf die plastischen Eigenschaften von nanoporösen Gold ist.

Acknowledgments

I would like to express my gratitude to everyone who encouraged and supported me throughout my doctoral studies. The success of this dissertation would not be possible without their guidance and precious support.

Most of all, I am deeply grateful to my thesis mentor Prof. Jörg Weissmüller for giving me the opportunity to join his scientific team and for the fascinating, cutting-edge research project I had the pleasure of working on. Working under his supervision has been a great honor; I have learned, grown, and gained invaluable research experience. I am thankful to him for the inspiring and considerate guidance, patience, and immense support of my research, all of which have been priceless for me.

My sincere thanks go to Dr. Jürgen Markmann for his constant support of my initiative, help with lab facilities, and many stimulating discussions. For me, as an experimentalist, this experience was inestimable.

I wish to acknowledge Prof. Hai-Jun Jin from Institute of Metal Research (Shenyang, China) for his valuable suggestions on dealloying and mechanical testing.

I appreciate the help of colleagues with whom I have been working during the past few years at Helmholtz-Zentrum Geesthacht and Hamburg University of Technology: Yi Zhong, Charlotte Stenner, Shi Shan, Dr. Maxim Smetanin, Dr. Zhen Qi, Dr. Yahui Xue, Tobias Kitzler, and Nam Ngô. Thank you for sharing your knowledge and fruitful discussions throughout these years. I am also thankful to Claudia Plaumann for the assistance with stereomicroscopy, as well as Jens Timmermann and Farhad Riazi from the Electron Microscopy unit at Hamburg University of Technology, for the technical support with the SEM studies.

Stephanie Koch and Peter Kummerow are acknowledged for their support with official matters during my stay at the Helmholtz-Zentrum Geesthacht. In addition, I thank Mr. Kummerow for organizing wonderful excursions in northern Germany, a place which became my temporary home.

I also take this opportunity to thank my Ukrainian teacher Prof. Sergiy O. Firstov, who introduced me to the field and influenced my academic pursuit in an ineffably positive way, as well as my former colleagues from Institute for Problems of Materials Science (Kyiv, Ukraine), for their encouragement and support during my first steps in research.

The study was financially supported by Deutsche Forschungsgemeinschaft through Grant WE1424/14-1.

Я безмежно вдячна моїй родині та друзям за любов, нескінченну віру та підтримку протягом цих відповідальних і таких важливих років для мене. Ви надаєте наснагу творити краще і рухатися тільки вперед.

Contents

List of Figures

Chapter 1

Introduction

1.1 Exploiting potentials of surface modification for design of interface-controlled materials

Friction, wear, adhesion, catalysis, oxidation, and corrosion are just a few examples of phenomena in which interactions occur at the *free surface* of a material. These important phenomena undoubtedly play a major role in technology, such as chemical processing, energy generation and conversion [1]. Although the surface – or, rather, the surface and electronic structure – govern a material's interactions with its surrounding environment, the influence of surface processes on the bulk of the material is generally considered to be small. This is because the surface constitutes a minimal fraction of the total volume [2]. However, in materials with nanometer scale dimensions (such as nanoparticles, nanowires, and their assemblies in the form of nanoporous or -crystalline materials) surface can start to dominate the overall material behavior. This is due to high density of surface atoms or grain/phase boundaries, which these materials possess [3] (Fig. 1.1a).

The reduced coordination of atoms at or near the surface of a solid relative to interior lattice atoms induces a redistribution of electronic charge and markedly affects the surface electronic structure. Even a perfect "bulk-like" surface, in which surface atoms approach positions of the substrate lattice, exhibits new electronic energy levels and modified many-body effects caused by altered chemical bonding [4]. As a consequence of the lack of coordination and broken chemical bonds (Fig. 1.1b), the surface atoms exhibit a higher energy (*surface excess free energy*), which becomes significant with decreasing feature size or increasing surface-to-volume ratio, and indeed may affect the behavior of the total volume of a high-surface area material [5]. Theoretical studies generally point to the contraction of the first surface layer spacing for most metal surfaces [6], which try to minimize the excess free energy. This surface contraction results in tensile *surface stress*[1] and intrinsic compressive stresses in the core [5] as schematically illustrated in Fig. 1.1c for a metallic nanowire. An example of a circular nanowire with a 4 nm diameter demonstrates that the bulk stresses in its core, which are required to compensate the surface stress, can reach a magnitude of 1 GPa, well above the strength of conventional engineering materials [7].

In bulk nanomaterials, the amount of the surface atoms with reduced coordination can occupy a substantial volume fraction of the solid [8]. Because these surface regions exhibit a local deviation from behavior of the bulk, materials with modified overall properties can emerge. Furthermore, effective manipulation of the surface states and modification the electronic structure would facilitate the design of novel functional materials or devices with *bulk properties controlled by interfaces*.

The concept of tunable macro-properties was first suggested by Gleiter [2, 8]; since then

[1] More about surface energy and surface stress concepts can be found in Chapter 2.

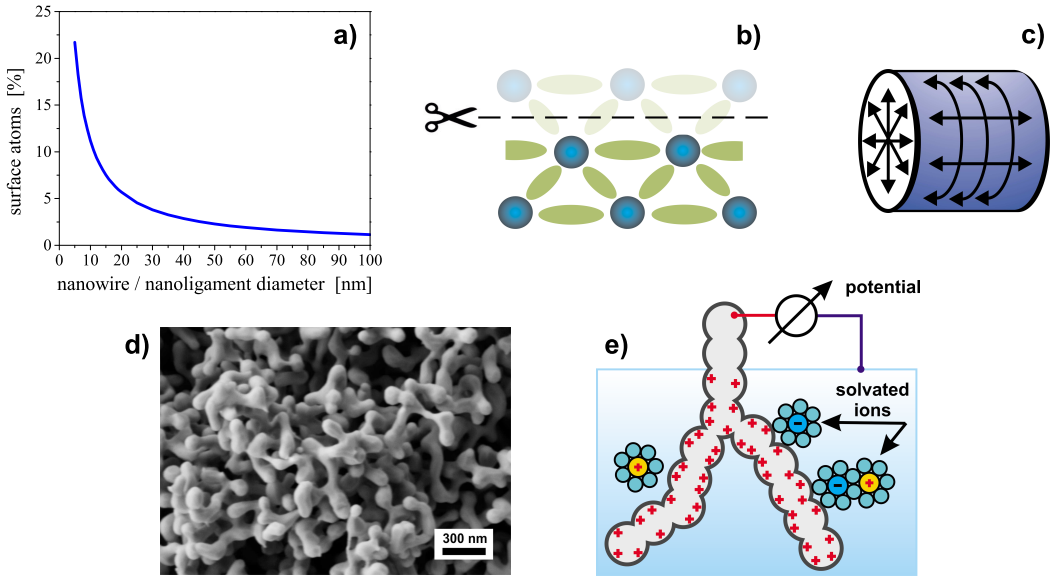

Figure 1.1. Distinctive features of high-surface area materials. (a) Estimated percentage of surface atoms in a nanometer-sized idealized cylindrical Au wire as a function of its diameter, assuming a ≈ 0.3 nm-thick surface layer. (b) Reduced coordination and broken chemical bonds after creation of a surface (schematically) in accordance with Refs. [2, 9]. (c) Schematic illustration of surface stress in a nanowire and the corresponding surface-induced stress in the bulk (adopted from Ref. [2]). (d) Scanning electron micrograph, exposing numerous free surfaces of nanoligaments in nanoporous Au (this work). (e) Interconnected nanocrystalline network immersed in an electrolyte as an example of device with tunable electronic structure (adopted from Ref. [8]).

it has been successfully achieved in many nanostructured solids. Tailoring of the properties can be realized in two ways, depending on the structure arrangements [10]:

- *irreversibly* via tuning microstructure (e.g., grain growth in nanocrystalline materials) *or*
- *reversibly* via reversible altering of the electronic and/or chemical structure of internal interfaces by means of external stimuli (e.g., by varying the chemical composition of a gas in the pores of nanoporous material).

The latter strategy in materials design (which affords a recoverable tuning of properties) is especially desirable for many specific technological applications in modern multifunction devices.

In this respect, *nanoporous metals* (np-metals) are ideally suitable candidates due to the high density (~ 10^{15} mm^{-3}) of their nanoscale constituents – *nanowires or nanoligaments* (Fig. 1.1d), whose entire surface can be addressed through the applied electric potential upon immersion in electrolyte (Fig. 1.1e) or upon exposure to a gas. Thus, the superficial charge density and/or adsorbate coverage controlled [10]. In this way, actuation [11], electric [12], magnetic [13], wetting [14], etc. properties of samples with macroscopic dimensions have been tuned.

Surprisingly, little attention has been paid to exploring the *reversible tuning of mechanical behavior* in these materials. Yet the possibilities for this concept have been probed. Jin and Weissmüller demonstrated that np-Au infiltrated with aqueous acid solution can change its strength when triggered by an electric signal [15]. The material can be switched from a strong, high-strength state to a weaker, a more malleable behavior, and vice versa. Additionally, a potential-dependent creep was reported [16], where a creep rate of np-Au was controlled by varying the applied voltage in the same electrolyte. While the reversible changes in the

plasticity of the nanoporous metal have been observed and possible underlying mechanisms have been discussed, relevant surface parameters that govern the plastic deformation are still under debate. Beyond that, no evidence for the elastic response of nanoporous metal upon electrochemical conditions has been reported so far.

1.2 Surface effects on materials' mechanics

1.2.1 Size-dependence of mechanical properties

Elasticity at the nanoscale

As distinct from micron and higher length scales, at sub-micron and nanometer length scales the *effective elastic modulus* displays a size-dependent behavior, implying that the modulus is no longer constant, but a function of a material's characteristic size [17]. This has been confirmed for many metal and semiconducting nanoscale thin films and nanowires by experimental measurements, including bending in an atomic force microscope (AFM) [18–20], vibrational studies or tensile testing within a transmission electron microscope (TEM) [21, 22], resonance frequency tests [23], theoretical investigations, including *ab initio* and density functional theory (DFT) [24], molecular dynamics (MD) [25–27] and modifications to continuum theory [28, 29]. So far, however, the results of the experiments with nanobeams and nanowires remain contradictory. With decreasing size, both stiffening (Pb, Ag, Pd, ZnO) [18, 20, 30, 31] and softening (Si, Cr) [19, 23] have been reported in different materials. There are also experiments showing no size-dependence [31–33]. These experimental works have acknowledged that surface effects are responsible for the variations in the elastic modulus, although the precise origin of these effects is often elusive [34].

The scale-dependence in elastic behavior and properties at the nanoscale is generally attributed to the surface effects, such as surface free energy [35], surface stress [36, 37], and surface elasticity [24, 38, 39].

The continuum theory of the *surface excess elasticity*[2] is considered to be the most promising tool for interpretation of the size-dependent phenomena in nanoscale materials. It admits a surface elastic modulus distinct from the bulk, viewing the surface as a separate layer with a predetermined thickness. Size-dependent surface modulus is then regarded to be the dominant effect that controls the overall elasticity of nanowires [40]. Atomistic computation using embedded atom method (EAM) potentials generally indicates an enhanced compliance of transition metal surfaces [38, 40], implying the possibilities for softening (reduction of the elastic stiffness) in the experiment. Density functional theory (DFT) also allows for local stiffening, depending on the electronic structure of the surface [24], thereby explaining the experimentally observed enhancement of the elastic stiffness. Studies in continuum mechanics, as reviewed in Ref. [41], have adopted the EAM results to predict the size-dependent effective elastic response for nanoscale objects. However, the applicability of EAM potentials for the problem has not been confirmed, and experimental verification is required. Therefore, the first reliable and generally accepted value for an excess elastic modulus at small size has yet to emerge.

Although the size-dependance has been observed by both theory and experiment, an inescapable gap still remains between two approaches, so a direct comparison between both is problematic [17]. The following factors explain this: *(i)* the scarcity of computational data for atomistic structures > 10 nm, *(ii)* no treatment of important surface phenomena, such as surface defects, surface reconstruction and surface phase transformations in some theoretical methods, *(iii)* experimental challenges in measuring structures < 10 nm, and *(iv)* environmental effects (e.g, surface contamination, native oxide layers, etc.) in experiments.

[2] All relevant details of the theory are given in Section 2.2.1.

Furthermore, it has been demonstrated that higher-order elasticity in the bulk of nanowires may strongly affect their elastic response and control the size-dependence [30, 40]. From an experimental point of view, one may therefore question if the surface excess elasticity has any confirmed impact on the elastic response of nanomaterials at all.

Plasticity at the nanoscale

Effect of length scale on strength for submicron and nanometer-scale samples is also discussed intensively. Recent nanomechanical measurements on small single crystal metal micropillars or nanowires with diameter < 10 μm have revealed substantially larger strengths relative to their bulk counterparts, which also increase dramatically with decreasing pillar or wire diameter [42, 43]. The strength of Au nanowires with 40 nm in diameter was found as high as 5.6 GPa by bending with an atomic force microscope (AFM) tip [32]. This value is up to 100 times greater than was reported for bulk Au (55 – 200 MPa) and attains the maximum theoretical shear stress for Au. Similar results are also for submicron Au columns machined by focused ion beam (FIB), around 500 or 800 MPa for 200−400 nm diameter, measured using a nanoindentation setup with a flat-punch tip [43–45]. In general, for face-centered-cubic (fcc) metals at micron and below length scales, the pillar flow stress (under uniaxial compression and tension) scales with a pillar diameter D as $\sigma \propto D^n$, where $n = -0.5... - 1.0$ [46]. Besides the size-dependent (yield) strength another interesting aspect is that, in contrast to bulk samples (that typically show a smooth transition from elastic to plastic flow and a steady rate of strain hardening), the single crystalline pillars exhibit drastic changes in the macroscopic stress-strain response. The compression curves consist of a number of large and discrete strain bursts separated by elastic loading segments, without significant reduction in the flow stress as the strain increases [42, 43]. The appearance of the elastic loading sections suggests a lack of dislocations throughout the deformation rather than their multiplication, like during strain hardening in metallic systems of the larger scale [44].

Several models have been suggested to interpret the size-dependent strength of submicrometer metallic pillars. A brief summary of the proposed mechanism in fcc metals follows.

The most widely discussed mechanism is the *dislocation starvation scenario* [43, 44], in which the mobile dislocations are considered to have a higher probability of annihilating at a free surface than of multiplying and being pinned by other dislocations. That is, plastic deformation in confined sample volumes is realized through the nucleation and motion of new dislocations, and not by interaction or storage of existing dislocations, as is the case for bulk crystals. The creation of a new dislocation by the nucleation would require very high stresses (either at surfaces or in the bulk of the crystal), leading to the observed high strengths. The predictions of the dislocation starvation hypothesis were supported by the *in situ* transmission electron microscopy (TEM) studies, where egression of preexisting dislocations at free surfaces during compression of a Cu pillar was observed [47]. This resulted in the crystal becoming starved of dislocations.

The *dislocation source truncation model* [48] is another commonly used theory to explain the effect of sample size on the yield strength. Contrary to the previous one, it argues that the pillar is not starved of dislocations. Given the limited dimensions in finite samples, double-ended Frank-Read sources (usual for bulk solids) upon operation interact with the surfaces and result in "truncated" single armed sources (FRS). The size effect is then attributed to the dependence of the critical stress required to activate and move the truncated arms on the dislocation length, which scales with the pillar diameter [49]. An evidence for this mechanism was obtained experimentally as well [47].

The size-dependence of strength and stochastic strain bursts were also predicted by *dislocation dynamics (DDD) simulations* [50]. The active mechanisms suggested by DDD include (a) single source-controlled plasticity, (b) reaction-controlled plasticity, and (c) dislocation multiplication-controlled plasticity.

At present, the relative importance of the different models are under debate, and a quantitative prediction of flow stress at small scales is yet challenging. Moreover, the deformation mechanisms of freestanding structures at a scale below 100 nm is not well explored [50], where dislocation nucleation, in fact, may turn out to be a tremendous deformation-limiting factor.

Beyond the dimensionality, environmental effects such as surface contaminations, impurities, and native oxide layers could all be influencing the mechanical behavior at sub-micron and nanoscales [50]. Thus, in the next Section the effect of environment and surface chemistry on deformation is considered.

1.2.2 Environmental exposure and surface condition on mechanical properties

Effects of surface condition and chemical or (electro-)chemical environment on the strength and fracture of solids, known as stress-corrosion cracking, corrosion fatigue, liquid metal or hydrogen embrittlement, etc. are well documented in engineering materials and widely discussed in literature (see for instance [1]). All these phenomena occur under stresses in a reactive, corrosive medium, normally resulting in detrimental impact on the mechanical behavior. Since the focus of the present study is on the *reversible variation of surface state*, here solely the influence of *reversible, non-corrosive processes* on mechanical properties will be shortly reviewed.

The early studies, which originate from work of Rehbinder [51], revealed pronounced changes in the plasticity and fracture induced by adsorption ("Rehbinder effect"). Decrease in the yield stress, rate of work hardening, stress and strain at fracture were reported for metals (Al, Co, Pb, Sn, Zn) while in contact with surface-active liquids. According to Rehbinder ([1, 52] and references therein), the environmentally-induced strength reduction or plasticizing is a consequence of the decrease in free surface energy of the solids (or work of formation of new surface during deformation). This would consequently promote dislocations movement out of crystals and the growth of microcracks at the surface [53]. Yet, Andrade and Randall [54] have suggested that the surface-active substances only remove an oxide film, which in its original condition strengthen the surface, and not penetrate deep into the crystalline microcracks, as supported by Rehbinder. Overall, these and the latter hypotheses, as well as similar experiments which intended to clarify the phenomena, were often controversial and even contradictory. This is most likely due to the samples specific surface area was too small and the environment was not sufficiently well controlled [55].

Nevertheless, intense investigations of the chemomechanical effects in the past gave rise to studying the mechanical response, when the surface is charged via electric polarization in electrolyte solutions. There is evidence of impact applied electrical potential on hardness [56, 57], friction [58], creep rate [52, 59, 60], and fracture [61] of metal electrodes (Fig. 1.2). Although the explanations here were controversial like in the "Rehbinder effect", important suggestions were made. First, it has been pointed out on the similarity between the potential-dependent mechanical characteristics and the electrocapillary parameters (surface tension and surface stress) of a metal/electrolyte interface. Second, it has been recognized an importance of dislocation interactions with free surfaces and species from solutions.

More recent data in the context of surface chemical effects on mechanical behavior have been obtained by nanoindentation combined with control of surface chemistry. Dramatic changes in the load-displacement data were observed for single crystal Au surfaces, which were chemically modified with a monolayer of oxide, Ag or Pb [63]. However, in accordance with the authors, these results are suspected since a change in the adhesion between used W indenter tip and the Au surface can promote variations in mechanical properties. A similar investigation of Au (111) films modified by self-assembled monolayers (SAMs) of alkanethiols manifested the "Rehbinder effect" [55]. The results revealed a significant impact of a SAM on contact geometry and plastic deformation during nanoindentation testing, suggesting that

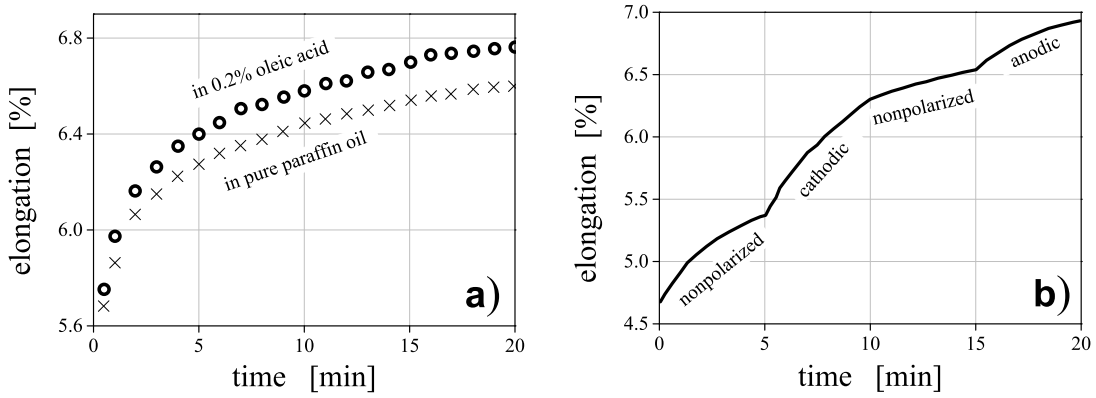

Figure 1.2. Impact of the (electro-) chemical environment/surface state on creep of 0.1 mm polycrystalline Au wire (after [59, 62]): (a) "Rehbinder effect" manifested by increasing of the creep rate after adding a surface-active 0.2% oleic acid into the pure paraffin oil, (b) creep rate tuned by electrochemical polarization in KNO_3 electrolyte.

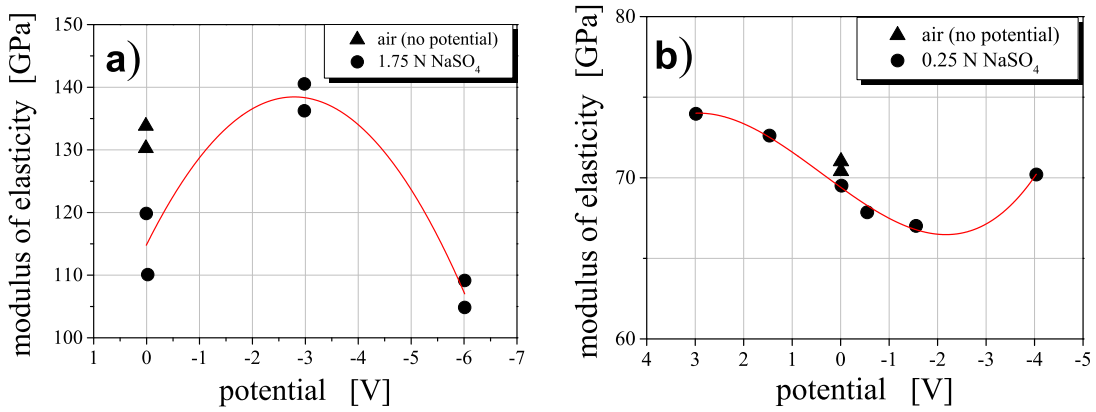

Figure 1.3. Modulus of elasticity vs. applied potential for polycrystalline, ≈ 0.9 mm thick metal sheets in dilute aqueous electrolyte of $NaSO_4$ (after [64]): (a) Cu (99.99%), (b) 6061-T6 Al alloy.

the presence of the SAM coating on the Au surface does enhance the ductility of the metal.

In contrast to rich reports on the environment-sensitive plastic deformation, much less is known about the impact of surface condition on the elastic response. The earliest relevant work of Eisner and Ottlyk indicates a 3% change in the elastic modulus for mm-thick sheets of polycrystalline Cu and Al alloy upon static tensile loading in sodium sulphate electrolytes with potential control (Fig. 1.3) [64]. The data, however, is questionable, owing to a negligible fraction of surface atoms. Besides, these metals have narrow polarizable windows, so oxide films may form and play a role.

1.3 Deformation behavior of nanoporous Au

A class of nanoporous (np) materials that are of interest in the present thesis are fabricated by *dealloying* [65], a corrosion process in which the less noble component is selectively dissolved from an alloy, chemically or electrochemically. The resulting morphology is characterized by a three-dimensional bicontinuous and uniform structure of nanoscale pores and solid ligaments (Fig. 1.1d), whose dimensions can be easily adjusted over a wide range from a few nanometers to several microns. This length change is directly related to surface area and curvature, so that nanoporous materials are considered as new model systems for studying length scale effects on the mechanical behavior [66]. Even without influence of environmental conditions or applied

signals, the mechanical behavior of nanoporous solids formed by dealloying itself represents a fascinating area of study. Nanoporous materials exhibit an entirely new phenomenology in comparison with conventional macroscopic foams or nanocrystalline materials due to the following noticeable aspects [67]:

- the grain size is much larger that the pore and ligament sizes. For instance, in a nanoporous sample with a ligament size of 5 nm and a grain size of 50 μm, each grain contains ~ 10^{12} nanoligaments [67], making them a part of the same, coherent crystal lattice and, as a result, adding an intriguing side to nanoporous materials deformation mechanism. This has no analogy in macroscopic foams or individual nanowires.

- The elastic response of a nanoporous solid reflects the action of capillary forces, which are neglected in macroporous materials, but have been appreciated for nanowires as discussed above, in Section 1.2.1.

- In view of recent studies on submicro- and nanowires, the plastic behavior of the local building blocks, such as the ligaments in dealloyed np-metals, deviates from that of macroscopic matter (Section 1.2.1).

Currently, nanoporous structures by alloy corrosion have attracted considerable attention and have been successfully obtained in a number of metals and alloys, including Au [68–71], Pt [72], Pd [73], Ag [74], Cu [73], Ni [75], Au-Pt [76], Au-Pd [77], Pt-Ru [78], and Pt-Ni [79]. Specimens in the form of nanowires, thin films or bulk macroscopic samples could be prepared. Yet, most of the mechanical investigation have been concentrated on np-Au due to ease of fabrication of monolithic mm-sized samples and control over structure size as well as no formation an oxide layer at ambient conditions.

Below is a summary of recent reports on the mechanical behavior of np-Au.

Early studies have revealed the macroscopic brittleness of np-Au with brittle-ductile transition dependent on the microstructural length scale [68]. The catastrophic fracture behavior is typically a consequence of high density of cracks that originate from a large volume shrinkage occurred during dealloying (up to 30% for np-Au [69]). This has prevented the experimental study of intrinsic behavior of macroscopic bulk samples and all subsequent investigations were focused on a small volume of the material using nanoindentation [80–84], column microcompression [85], and film or beam bending tests [86, 87]. Effective strength values determined from these studies were found to be one order of magnitude higher (70, 90, 145 MPa) than typically obtained in the conventional metallic foams at a similar density (below 5 MPa for Al foam [88]).

For a conventional macroscale foam with open porosity and cell size < 1 μm, the yield strength is governed by the properties of the base material, σ_y^{B}, and the solid volume fraction, φ, in accordance with the scaling equation developed by Gibson and Ashby [89]

$$\sigma_y = C_1 \sigma_y^{\mathrm{B}} \varphi^{3/2}, \tag{1.1}$$

where $C_1 \approx 0.3$ is the fitting constant for foams with small solid fraction ($\varphi \leq 0.3$); the solid volume fraction (or relative density), φ, is defined as a ratio between the density of a porous material to the density of the base material. Although an applicability of this law to nanoporous structure is doubtful (see comparison of Eq. 1.1 with experimentally obtained values from different studies in Fig. 1.4b), the strength of the individual ligaments that was estimated on its basis (σ_y^{B}) using the experimental data for np-Au revealed a striking result – the yield stress of a nanoligament approached the theoretical shear strength of Au (4.8 GPa [32, 66]) [80, 85, 87, 90]. Moreover, it also showed size-dependence, where smaller ligaments led to the higher strength [81] consistent with similar observations on Au microcolums or nanowires as has been discussed in Section 1.2.1 (see also Fig. 1.5b). In contrast, studies on

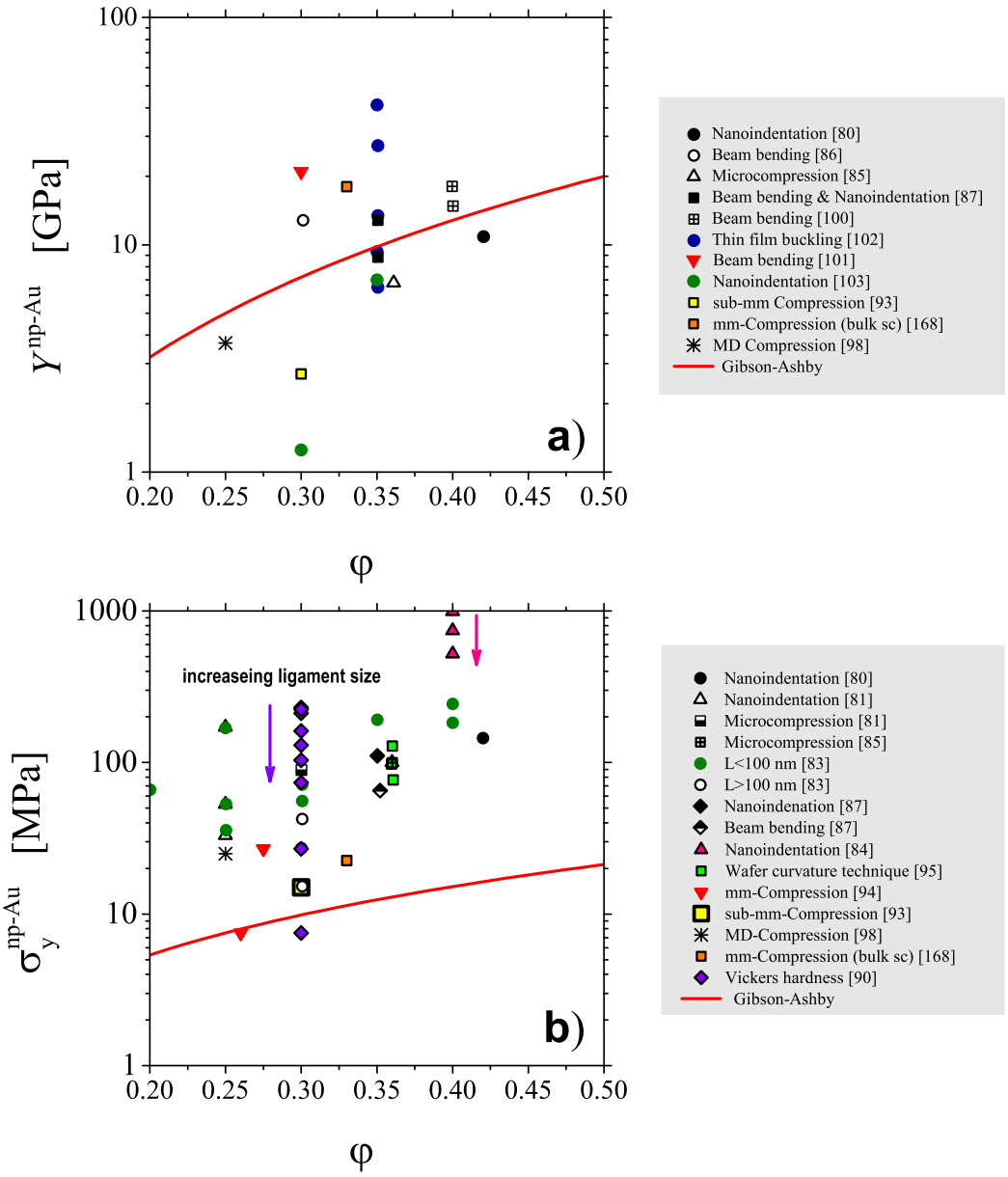

Figure 1.4. Experimental (*symbols*) and predicted by the Gibson-Ashby scaling relations (*lines*): (a) Young's modulus, $Y^{\mathrm{np-Au}}$, and (b) yield strength, $\sigma_y^{\mathrm{np-Au}}$, of np-Au as a function of the solid fraction of the material, φ. The experimental data have been collected from different studies as indicated in the Figure. Parameters in the Gibson-Ashby curves for Au: Y^{B} = 80 GPa and σ_y^{B} = 200 MPa. Arrows indicate decreasing of the ligament size for the samples with the same solid fraction. Mm- and sub-mm-compression stand for the compression of respectively millimeter- and submillimeter-sized samples, MD denotes molecular dynamics simulation. Adopted from Ref. [66], including the most recent available data.

macroscale foams found a negligible effect of the cell size at a given porosity on the mechanical behavior. This underlies the distinction between conventional and nanoporous foams.

Despite macroscopic brittleness of np-Au and the large estimated strength of its individual ligaments, it has been observed that the ligaments deform plastically either during nanoindentation [80] or during loading in bending or tension [92, 93], confirming the intrinsic ductile behavior of nanoligaments in np-Au.

Later on, the development of the improved dealloying methods (through minimization the volume shrinkage and crack formation) permitted deformation of mm-sized samples up to strain of 80 and 0.3% in compression [94] and tension [93], respectively. These experiments reported the effective yield stresses < 30 MPa, that is significantly lower than deducted from the nanoindentaion and micropillar compression tests. The discrepancy has been suggested to originate from overestimates while converting hardness into yield stress [94] or from structure morphology [93]. However, it is significant that the macroscopic np-Au samples with low yield strength from those studies still reproduces the size-dependent behavior of the ligament strength (Fig. 1.5b).

The size effect on plasticity has stimulated the transmission electron microscopy (TEM) investigations of structure defects in np-Au. A motion of dislocations generated within individual ligament during *in situ* TEM nanoindentation has been detected by Balk *et al* [95]. The dislocations were gliding to the ligament nodes, where they interacted with dislocations from other ligaments. Dou and Derby arrived at the same conclusion. During a TEM study of a deformed nanoporous nanowire (diameter of $\sim 5-10$ nm) they observed localization of a large number of defects near to the ligament junctions [96]. These deformed regions showed large densities of microtwins and Shockley partial dislocations. Significant dislocation activity inside the ligaments have been also seen by molecular dynamics simulations, upon tension [97, 98] and compression [98, 99]. Besides, the presence of pore channel dislocations has been confirmed by direct observation via the high-resolution TEM [69] and their consequences for the possible deformation mechanisms have been discussed [94]. This evidence therefore indicate that the plastic deformation of np-Au is governed by dislocation activity as in conventional massive metallic materials. Nevertheless, the relevant deformation mechanism(s) in np-metal in terms of dislocation behavior have not been elaborated yet, and a comprehensive study of defect evolution during mechanical loading by both experiments and simulations are highly required.

Young's modulus of np-Au was also determined using nanoindentation, film bending, and microtensile or -compression tests. The values in the range $3-13$ GPa are reported for ligament sizes of $20-100$ nm and solid volume fractions of $0.3-0.42$ [80, 84–87, 93, 100, 101]. Atomistic modeling revealed the lower values of the elastic modulus – within $3-4$ GPa both for tension [97] and compression [98] at $\varphi = 0.24-0.36$ and significantly smaller ligament diameters of $\sim 2-4$ nm. Contrary to the effective yield strength, most experimentally found values of the effective stiffness agree with the Gibson-Ashby prediction for the respective solids fraction. Even though the lesser [83, 93] as well as extremely higher values [102] have been reported. Figure 1.4a compares the elastic modulus of np-Au, $Y^{\mathrm{np-Au}}$, calculated according to the corresponding Gibson-Ashby scaling equation for an open cell foam

$$Y = C_2 Y^{\mathrm{B}} \varphi^2, \tag{1.2}$$

with experimental data in literature, using a constant $C_2 = 1$ and Young's modulus of fully dense Au, $Y^{\mathrm{B}} = 80$ GPa. While some single values from these reports approach the prediction, the overall agreement with the scaling law seems to be unsatisfactory. A systematic study of the solid fraction impact on the elastic modulus of np-Au by nanoindentation [103] indeed verified the observation. The deviation is however expected since the scaling expressions valid only for cellular materials with low densities ($\lesssim 0.1$) and with the assumption that bending of the cell walls dominates. Whereas the solid fraction investigated in [103] were in the range

0.25–0.4, i.e., different geometry of ligaments (thicker and shorter dimensions) would probably contribute to the effective stiffness via other deformation modes (axial or shear).

Regarding the nanoscale effects on the effective elastic properties of np-Au, so far only a few experimental data are available that indicate absence of those [66, 103] (Fig. 1.5a). An exception to this is a work by Mathur and Erlebacher [102], who revealed a dramatic 4-fold increase in the effective Young's modulus of np-Au, from ~ 10 to ~ 40 GPa, when ligament size drops below 10 nm. Among factors that caused the enhanced stiffness, the authors discussed density increase that occurred during dealloying, action of surface stresses, and a higher bending stiffness of thiner ligaments [66]. Continuum mechanics studies [104–106] elucidate this experimental observation by incorporated surface effects (surface energy, surface stress, and surface elasticity) into their models. They suggest that the elastic properties of nanoporous materials depend principally on *surface elasticity*. Altogether, there are still a lot of open questions relative to elastic response of np-Au. Like in case of the strength probed in small sample volumes, testing issues as well as uncertainties of solid fractions variations (after synthesis and during testing) might lead to erroneous results. A careful examination through conventional mechanical testing on macroscopic samples with well defined geometry, solid fraction, and surface state is thus needed.

It is natural to expect that the mechanical properties of nanoporous material is governed by the simultaneous contribution from their individual, nanometre scale building blocks – nanoligaments – on the one hand, and from the interfaces that connect them with the environment on the other hand.

Size and dimensionality may indeed affect the behavior of the building blocks themselves, rather just the whole volume of the material. Therefore, it is instructive to compare the trends in mechanical behavior of np-Au with findings reported for Au submicron- and nanowires.

Figure 1.5 compiles the calculated data of ligament modulus and yield strength of np-Au as a function of the ligament diameter along with selected data on Au nanowires (adopted from Refs. [66, 67]).

Emerging consistency of both data sets in Fig. 1.5 is noteworthy, meaning that two trends – scatter of the modulus values and obvious enhancement of the strength for smaller sizes – can be explained by referring to studies of small-scale systems.

1.4 Research objectives and experimental approaches

As has been emphasized in the previous sections, the underlying processes for the elasticity and plasticity of metals measured at the nanoscale are not well understood, and specifically the role of the surface – for instance in stiffening or softening of nanostructures – is the subject of debate. It has been also demonstrated that changes in the surface electrochemistry can strongly affect the mechanical behavior of solids.

This thesis therefore aims to develop a robust and sensitive research method in order to probe the *role of the surface in elastic and plastic deformation of nanomaterials*. The experimental approach employed during investigations combines two aspects, in which

- the amount of the surface area is tuned by varying a structure size
- the state of the surface is *reversibly* and *cyclically* modified by external stimuli.

As a suitable model material with large specific surface area, nanoporous Au (np-Au) made by alloy corrosion is studied. By adopting recent synthesis routes, np-Au millimeter-sized specimens that are highly deformable in compression can be prepared (> 60% strain).

Unique properties of a np-metal, as a bulk-nanostructured material, rest on its morphology – three-dimensional bicontinuous network of nanosized metallic ligaments and pore channels – which provides good electrical conductivity and large effective surfaces (Fig. 1.1d). The

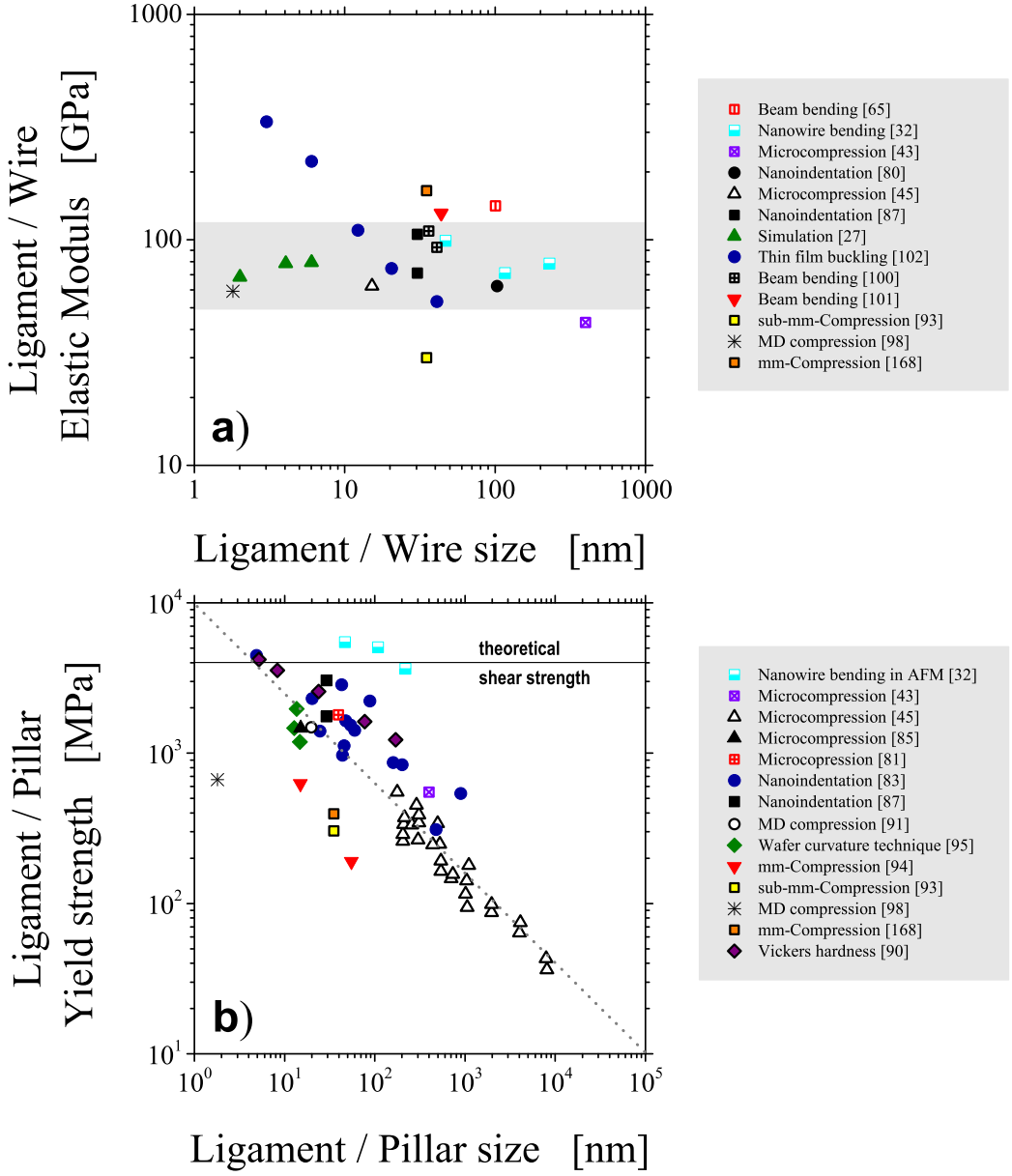

Figure 1.5. (a) Calculated ligament modulus and (b) yield strength of Au nanoligament (Y^{B} and σ_y^{B} in Eqs. 1.2 and 1.1, respectively) as a function of the ligament diameter. The experimental data were collected from different studies on np-Au and Au nanowires (corresponding references indicated in the Figure). Shaded area in (a) represents range of Young's modulus values for single-crystal gold in various crystallographic directions. In (b), the solid line marks theoretical shear strength, and the dashed line is a power law with exponent −0.6. Mm- and sub-mm-compression denotes the compression of respectively millimeter- and submillimeter-sized samples, MD stands for molecular dynamics simulation. Adopted from Ref. [67] with the most recent available data added.

characteristic lengths (ligament and pore size) are easily controlled by synthesis conditions and the pore space is penetrable for fluids and gases. Besides that, the np-metal provides an opportunity to study the mechanisms of plastic deformation at the nanoscale, as it has been well illustrated in Fig. 1.5b.

In the work, the surface modification of np-Au was realized via infiltration the metallic "skeleton" with an aqueous electrolyte and controlling the Au-fluid interface by application of electric potentials (Fig. 1.1e). In this way, two very different components – gold and water – are intermixed at close to atomic dimensions, resulting in a *hybrid material* with tunable interfacial properties. Utilization of aqueous alkaline or acid solutions is particularly preferable, since the achieved specific capacitance of a metal-electrolyte interface is higher than for organic electrolytes (typically $5-20$ μF/cm^2) [107] and as the result, the effect of the surface charging during reversible adsorption of ions of an electrolyte can be more pronounced.

The advantage of using np-Au as an electrode here is based on unique electrochemical properties of gold among other solid metal electrode materials [108]. The range of potentials where it displays ideal or nearly ideal polarizable behavior (no dissolution, formation of oxides or hydrides) exceeds 1 V [60], appearing to be electrochemically stable.

The thesis focuses on **three primary objectives**:

- implementation of *in situ* environmental control during compression experiments on np-Au in a dynamic mechanical analyzer (DMA) and mechanical testing device
- experimental probing of the surface excess elasticity effect on the elastic response of the material
- identifying the phenomena at the surface that govern plastic deformation.

The outcoming research findings are expected to promote understanding of the size-dependent and environmentally-controlled mechanical behavior of nanomaterials.

1.5 Outline of thesis

The thesis is organized as follows.

Chapter 2 provides a necessary theoretical background for discussion of the results obtained in this work. It presents basic aspects of clean and electrochemically-modified metal surfaces, starting out from introduction to important concepts in thermodynamics of solid surfaces, namely *surface tension* and *surface stress*. These capillary forces are especially substantial for np solid, in which surface stress can induce a significant stresses in the bulk. The essentials of a continuum theory of *surface excess elasticity*, the relation between the surface stress and surface strain, is presented as it has been profitably employed for analysis the elastic behavior of np-Au.

The second part of the Chapter focuses on structure and mechanics of solid/electrolyte interface. A brief review of relevant experimental measurements of the interfacial tension of solids (zero creep experiments) and surface stress (potential-strain response measurements) are outlined.

The purpose of **Chapter 3** is to describe the details of synthesis of np-Au specimens and the experimental procedures followed in the work. Since the current study employs some of the electrochemical methods, a brief introduction to these techniques given. *In situ* mechanical testing setups that have been developed in the work are described in detail.

Chapter 4 presents the results of compressive mechanical tests on np-Au in air and electrolytic medium, focusing on the two key themes: electrochemical modulation of the elastic modulus and flow stress. It begins with a description of microstructure and specific surface area of np-Au specimens. The latter is a crucial parameter since the functionality of

the material relies on the amount of the free surface. The next Section focuses on the stress-strain behavior, with an emphasis on the elastic properties in air. These results have been served for qualitative comparison with computational studies by finite element modeling in Ref. [109] and by molecular dynamics [99]. Both approaches allow to identify the underlying mechanisms responsible for the mechanical behavior of np-Au in air observed in this study. The followed Sections narrate the important findings of the electrically modulated stiffness and strength in aqueous electrolytes, including anions with different adsorption behavior (weakly and strongly adsorbing).

In **Chapter 5** the mechanical response of np-Au in air and electrolytic medium will be discussed, taking into account the action of capillary forces.

Chapter 6 summarizes the results, suggesting potential applications and place of the work in context of importance for nanotechnology. Finally, outlook is given in **Chapter 6**, stating new ideas for exploring an amazing world of phenomena occurring at solid-fluid interface.

Chapter 2

Fundamental aspects of clean and electrochemically modified metal surfaces

2.1 Surface tension and surface stress of a clean solid surface

2.1.1 Main concepts and definitions

The central thermodynamic quantity that characterizes a surface (or interface) is energy of the formation of its unit area [110]. The process of surface formation or changing its area can be performed in two different ways – elastically or plastically[1]. When the surface of a liquid increases, the number of surface atoms increases in proportion, since they can flow freely from the interior of the liquid to its surface. Due to the high mobility of liquid atoms, their average density and configuration in the surface remain unchanged and will be identical to the surface structure before deformation. In that sense, the liquid surface deforms plastically. By contrast, in solids an increase in the surface area can also entail *elastic* stretching. The surface atoms are forced to remain coherent with underlying bulk lattice, so that the stretching will increase the average distance between the atoms while keeping the number of surface atoms constant. Therefore, the different physical nature of the plastic and the elastic formation of a surface area lead to two fundamentally different concepts in surface thermodynamics introduced by Gibbs: the *surface free energy* and the *surface stress*[2] [113]. Below, the definitions of these thermodynamic parameters will be given for the case of a one-component system at constant temperature, volume, and chemical potential (composition).

The surface tension (γ) is defined as a change in the Helmholtz free energy ∂F of the system, resulting from the reversible change of surface area ∂A at constant elastic strain $\mathbf{E}^{\mathsf{S}}$, constant temperature T, and chemical potential μ_i [113]:

$$\gamma = \left.\frac{\partial F}{\partial A}\right|_{\mathbf{E}^{\mathsf{S}},T,\mu_i}, \tag{2.1}$$

where $\mathbf{E}^{\mathsf{S}}$ is the tangential strain tensor at the surface, which denotes directions of the elastic

[1] It must be underlined that here and therein in this Chapter *plastic* means a *reversible* change in surface area by adding atoms to the surface without changing their relative distances, i.e. at constant structure. This is different from the meaning of "plastic deformation" in metal physics, where it relates to *irreversible* processes, involving dislocations, diffusion, etc. [111].

[2] The terms "surface free energy", "surface tension", and "surface stress" often cause confusion and misinterpretation in literature (a good discussion of this is given in Ref. [112]). For that reason, in this work, the Gibbsian "surface free energy" (or excess free energy) and "surface tension" will be called "surface tension" and "surface stress", respectively.

deformation in the surface plane[3].

In general, the surface tension γ of a solid depends on orientation of its different crystal faces [111]; this anisotropy is responsible for the faceted shape of crystals [114].

While the surface tension γ is related to the reversible work per unit area required to create a surface, the surface stress $\mathbf{s}$ is related to the reversible work per unit area required to strain an already existing surface. The latter is given by the derivative of the excess free energy of the surface (γA) with respect to the strain $\mathbf{E}^{\mathrm{S}}$ at constant temperature [114]

$$\mathbf{s} = \frac{\partial(\gamma A)}{\partial \mathbf{E}^{\mathrm{S}}} = \gamma \mathbf{I} + \frac{\partial \gamma}{\partial \mathbf{E}^{\mathrm{S}}}. \tag{2.2}$$

Here, $\mathbf{s}$ is the second-rank tensor reflecting the directional dependance of the straining, $\mathbf{I}$ is the second-order identity tensor, and γ represents the surface free energy per unit area of the actual (strained) surface. Equation (2.2) is the Shuttleworth equation, which states that for solids the surface stress will differ from the surface tension. For liquids, a term $\partial\gamma/\partial\mathbf{E}^{\mathrm{S}}$ vanishes, and the surface stress is the same as specific surface energy.

Equation (2.2) can be represented in a simpler form [115]

$$\mathbf{s}^{\mathrm{L}} = \frac{\partial \gamma^{\mathrm{L}}}{\partial \mathbf{E}^{\mathrm{S}}}, \tag{2.3}$$

where $\mathbf{s}^{\mathrm{L}}$ and γ^{L} are measured in an undeformed state ($\mathbf{E}^{\mathrm{S}} = 0$), i.e., with respect to the unstrained reference area A_{L} (Lagrangian coordinates[4]). The surface areas in both states are connected via $A = A_{\mathrm{L}}(1 + \mathrm{tr}\mathbf{E}^{\mathrm{S}})$ with $\mathrm{tr}\mathbf{E}^{\mathrm{S}}$, the trace of the surface strain [115].

Due to the tensor character of $\mathbf{s}$, the surface stress in general anisotropic and can have negative components, whereas the surface tension γ is always positive scalar quantity for a given surface orientation. Equation (2.3) defines a sign convention for the surface stress: a tensile stress is positive (contraction in the surface plane at lowered γ) and a compressive stress is negative (expansion of the surface plane).

For conciseness, a scalar surface stress, f, defined as half the trace of the surface stress tensor $\mathbf{s}$ ($f = \frac{1}{2}\mathrm{tr}\mathbf{s}$), will be mainly used during discussion in this work.

2.1.2 Determination in experiment and theory

The absolute value of the surface tension of solid materials is a fundamentally important energetic quantity in many materials science applications [116]. It is essential for understanding many processes occurring at surfaces or interfaces, such as adsorption, phase transformations (crystal nucleation, growth, and coarsening, recrystallization, grain-boundary phase transitions, etc.), mechanical properties and failure (brittle fracture) [117]. The parameter γ is especially of great importance for crystals of nanometer size by affecting their faceting, roughening, surface segregation, and equilibrium shape [118]. However, despite its well-recognized significance, methods of *direct* measurement of surface tension for solids so far are not reliable enough [114]. This is in contrast to a large variety of techniques to measure surface tension of liquids that reached high accuracy until now [111]. Moreover, all of the known values of γ obtained for solids are considered to be averaged over a range of crystallographic orientations owing to difficulties in experimental determination of the surface tension anisotropy [118].

One of the most consistent and commonly used techniques to measure the surface tension of a free surface of solid is the *zero creep method* developed by Udin *et al* [119, 120]. It has provided quantitative values for surface tension for a limited number of solids, mostly metals [121].

[3]The surface is allowed to relax in the direction normal to the surface.

[4]In the case where the Lagrangian coordinates will be used further in the text the index L will be omitted for brevity.

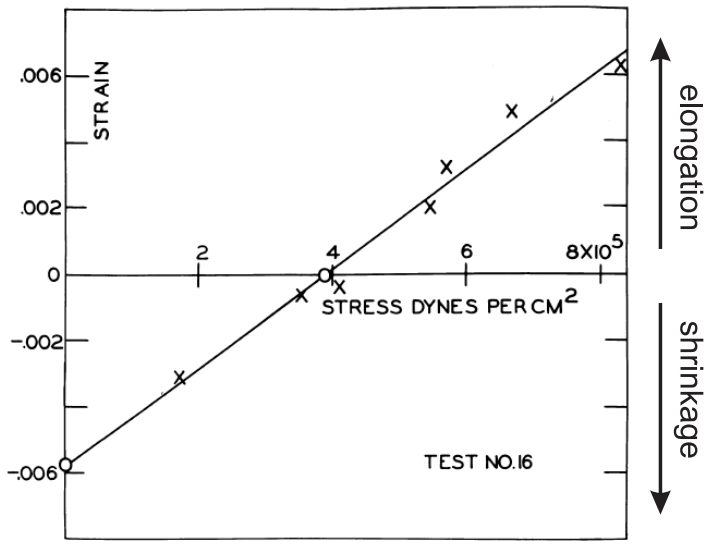

Figure 2.1. Stress vs. strain of Cu wire specimen (ø = 72 μm) at 950°C [122]. Stress of zero creep occured at 0.04 MPa (corresponds to 4×10^5 dyn/cm^2 in the diagram).

The zero creep technique rests on the high temperature creep, a plastic flow of a material subjected to a constant load at constant elevated temperature. A slow deformation accomplished during creep does not change the average density and configuration of the atoms in the surface, so that all deformations in the material can be considered as fully plastic (Section 2.1.1). In this case, $\partial\gamma/\partial\mathbf{E}^S = 0$ in Eq. (2.2), and the surface stress and surface tension become identical. At the point when the creep deformation stops, a *zero creep point*, the applied load will be balanced by the contracting force of the surface tension. In the original experimental procedure of Udin *et al.* [119, 120], a set of variously weighted metal wires of uniform length and diameter are allowed to extend or contract at temperatures around $0.7T_m - T_m$ in vacuum. By plotting stress vs. strain for a wire array in one test, the stress at zero strain, $\sigma_{\varepsilon=0}$, can be determined from a linear fit of the stress-strain plot (under the assumption that the wires deform viscously). The surface tension γ is then obtained via

$$\gamma = \sigma_{\varepsilon=0} r, \tag{2.4}$$

where r is the radius of the wire. Figure 2.1 illustrates a stress-strain diagram of a typical zero creep experiment.

The method, however, provides surface tension values at high temperatures, sometimes approaching the melting point T_m [121]. For metals, surface tension for a range of temperatures well below T_m are almost exclusively available from computer simulations [123]. Yet, these values should be viewed with caution, taking into account different simulation artifacts that might arise from time-scale limitations and inaccuracies of the used interatomic potentials [124].

According to Buttner *et al* [120] and Kumikov and Khokonov [121], an absolute experimental value of the surface tension for Au (purity 99.98 – 99.999) is obtained by the zero creep near T_m is around 1.4 N/m. An estimate based on measurements in the liquid phase gives $\gamma \sim 1.3$ N/m for Au at T_m and $\gamma \sim 1.5$ N/m at $T = 0$ K (the latter was obtained by extrapolation from experimental γ data at higher temperatures [125]). First-principles calculations yield 1.25 and 1.42 N/m for (111) and (100) Au clean surfaces at $T = 0$ K, respectively, whereas semi-empirical calculations result (using embedded atom method, EAM) in a γ–value of 0.79 N/m for the Au (111)- and 0.92 N/m for (100)-configurations [113]. In general, the agreement between the experimentally derived and the theoretical values is reasonably good.

Similar to the surface tension, the surface stress plays an important role in many structural and morphological phenomena. Surface reconstruction, shape transitions in nanoparticles, surface alloying, surface diffusion, epitaxial growth, and self-assembled domain patterns are only few examples [6]. Direct experimental measurements of f also remain a challenge, and data on the surface stress of clean surfaces originate mainly from theoretical calculations [113, 114]. Earlier attempts to experimentally determine the absolute value of the surface stress relied on electron diffraction measurements of the lattice parameter of small particles, a. Contraction (or expansion) of the surface layer induced by the surface stress leads to measurable deformations in nm-sized particles, Δa, and f was then calculated by [113]

$$f = -\frac{3}{2}\frac{\Delta a}{a}\frac{K}{r}, \tag{2.5}$$

where r, the radius of a solid particle, K, the compressibility. This method, however, suffers from uncertainties in the orientation of the particle surfaces and other experimental difficulties (the issues are discussed in Ref. [113]) that impair its accuracy significantly. By contrast, *changes* of surface stress due to adsorption or charging in electrolytes can be measured quantitatively and with great sensitivity for a number of metal-electrolyte systems[5].

To date, *ab initio* calculations of surface stress of clean surfaces are considered to be the most reliable method of determining the absolute values of f [113]. For clean (111) and (100) Au surfaces these data indicate values of 2.77 and 4.56 N/m, respectively [113]. The positive values of f in this case imply an attractive interaction between atoms in the first layer and tendency of the surface to shrink (tensile stress) [113].

It should be pointed out that real surfaces frequently do not exhibit the atomic structure of a truncated bulk: surface atoms may relax away from their bulk positions (*surface relaxation*) or more dramatically change their lateral distances (*surface reconstruction*[6]) [113]. These structural changes of atomic positions in the surface layer are considered to substantially influence both f and γ, and the calculations taking into account relaxation and reconstruction are concerned to provide more reliable results [114].

2.2 Deforming a clean solid surface

2.2.1 Elastic description of a free solid surface. Surface elastic constants

When describing elastic properties of a macroscopic solid B within classical theory of elasticity, the surface effects are usually ignored, and no specific elastic behavior is attributed to its surface S. The surface is solely considered as a simple boundary at which external forces are applied to the solid. Yet, for a nanoscale material with large surface/bulk ratio, the overall effective elasticity can be considerably affected by changes in the interatomic bonding at the surface. This is well manifested by numerous experimental reports on the size-dependance of the elastic properties (Section 1.2.1). A simple way to interpret this phenomenon is to assign to surface S the elastic properties that differ from those of the bulk core B. A continuum theory that describes the elastic behavior of surfaces (*theory of surface elasticity*) has been developed by Gurtin and Murdoch [126]. In this theory, a surface can be viewed as a two-dimensional thin film perfectly attached to an elastic body and all fundamental equations of the classical theory of elasticity hold for the bulk core, namely

[5] A brief discussion of these results will be presented in Section 2.3.2.

[6] *Surface relaxation* is a compression (or extension) of the topmost (or top few) layer separations normal to the surface while in-plane spacing of the surface atoms is preserved. When the latter is changed, this is called *surface reconstruction* [4].

- strain-displacement equation

$$\mathbf{E}^{\mathsf{B}} = \frac{\left(\nabla \otimes \mathbf{u}^{\mathsf{B}} + \mathbf{u}^{\mathsf{B}} \otimes \nabla\right)}{2}, \tag{2.6}$$

  where $\mathbf{u}^{\mathsf{B}}$ denotes the displacement in the bulk and infinitely small deformations are assumed in the solid ($|\nabla \mathbf{u}^{\mathsf{B}}| \ll 1$);

- constitutive equation (Hooke's law)

$$\boldsymbol{\sigma} = \mathbf{C}^{\mathsf{B}} : \mathbf{E}^{\mathsf{B}} \qquad \text{or} \qquad \mathbf{E}^{\mathsf{B}} = \mathbf{S}^{\mathsf{B}} : \boldsymbol{\sigma}, \tag{2.7}$$

  where $\boldsymbol{\sigma}$ is the the stress tensor of the bulk, the materials elastic constants represented by stiffness tensor $\mathbf{C}^{\mathsf{B}}$ and compliance tensor $\mathbf{S}^{\mathsf{B}}$ of the bulk. For isotropic materials Hooke's law reads

$$\boldsymbol{\sigma} = \lambda(\mathrm{tr}\mathbf{E}^{\mathsf{B}})\mathbf{I} + 2\mu\mathbf{E}^{\mathsf{B}} \qquad \text{or} \qquad \boldsymbol{\sigma} = \frac{Y}{1+\nu}\left(\mathbf{E}^{\mathsf{B}} + \frac{\nu}{1-2\nu}(\mathrm{tr}\mathbf{E}^{\mathsf{B}})\mathbf{I}\right) \tag{2.8}$$

  with only two independent elastic constants: λ and μ, the Lamé or Y and ν, the Hooke's constants, respectively;

- equilibrium equation

$$\nabla \cdot \boldsymbol{\sigma} = 0. \tag{2.9}$$

In order to account for the presence of the surface with surface stress, the boundary conditions need to be modified, so that instead of Eq. (2.9) one uses:

- surface equilibrium equation

$$\boldsymbol{\sigma} \cdot \mathbf{n} = -\nabla_{\mathsf{S}} \cdot \mathbf{s} \tag{2.10}$$

  where $\mathbf{n}$ is the normal to the surface S, $\nabla_{\mathsf{S}} \cdot \mathbf{s}$ is the surface divergence of the surface stress tensor field $\mathbf{s}$. Equation (2.10) is similar to the Young-Laplace equation that describes a stress balance at an interface between a fluid and air at equilibrium via $\Delta P = \gamma^{\mathsf{F}}(1/R_1 + 1/R_2)$ with ΔP, the pressure drop across the surface, γ^{F}, the surface tension of the fluid, R_1 and R_2, the principal radii of the curvature. For a solid with complicated geometry and anisotropic surface stress, Eq. (2.10) says that at each point of a curved surface $\mathbf{s}$ creates a force per unit area that must be balanced by a bulk stress underneath the surface [127]. Thereby, it represents the generalized Young-Laplace equation for solids.

The constitutive equation of the surface elasticity is analogous to Eq. (2.7) and expressed as [128]

- constitutive equation of the surface

$$\mathbf{s} = \mathbf{C}^{\mathsf{S}} : \mathbf{E}^{\mathsf{S}}, \tag{2.11}$$

  where $\mathbf{C}^{\mathsf{S}}$ is the surface stiffness tensor representing a measure of the surface stress changes with the surface strain. For an isotropic surface, Eq. (2.11) reduces to

$$\mathbf{s} = \lambda^{\mathsf{S}}(\mathrm{tr}\mathbf{E}^{\mathsf{S}})\mathbf{l} + 2\mu^{\mathsf{S}}\mathbf{E}^{\mathsf{S}}, \tag{2.12}$$

  where $\mathbf{l}$ is the second-order unit tensor in two-dimensional space, λ^{S} and μ^{S} are the Lamé constants for the surface [128].

It has been pointed out in Refs. [38, 129] that in contrast to the bulk elastic constants, the surface elastic constants can be negative. An available theoretical study on the determination of the surface elastic properties by atomistic simulations using the embedded atom method (EAM) potentials confirm this notation [38], suggesting, e.g. for Au(111) a surface elastic constant ≈ -8 N/m. However, these computational values still wait for verification. Since the experimental determination of surface elastic constants is a challenging task so far ([38] and citations therein), reliable calculation methods and careful interpretation are in high demand.

2.3 Surface tension and surface stress of a charged or adsorbate-covered surface

2.3.1 Space-charge regions and electrified metal-fluid interface

It has been mentioned in Section 2.1.2 that the reliable experimental data on surface tension so far are only available from the zero-creep measurements at high temperatures, whereas the data on surface stress is available from measurements of the relative changes induced by charging or adsorption of a surface. At present, experimental dependencies of γ and f as functions of the applied electric potential or superficial charge density serve as the major source of accurate quantitative values of the capillary forces. Therefore, it is expedient first to illuminate a few basic concepts regarding surface states in the presence of charges or adsorbates.

Space-charge regions

If an electric charge brought into the vicinity of a surface of a solid in a vacuum, a perturbation occurs in the electron concentration underneath the surface region. The charge carriers will rearrange to compensate or screen the electric field of that additional charge. Spatial regions inside the solid over which the electrically charged species have to rearrange in order to establish the effective shielding are defined as *space-charge regions (SCRs)* [4]. The SCRs for the case of a metal surface are depicted schematically in the upper part of Fig. 2.2, where an electron deficiency (a) or electron excess (c) appear underneath the surface, depending on the nature of the introduced charge in the near-surface region of the solid. In the lower part of Fig. 2.2, the corresponding electron energy levels bend up (a) or down (c), thus producing a *surface potential barrier*, in oppose to the flat bend condition of the neutral state (b). Such barriers may exert a pronounced influence on the motion of charged species across interfaces, on adsorption equilibria as well as on mechanical properties (the latter has been extensively discussed in Ref. [130] for insulator materials).

The SCRs can form *spontaneously*, without applying external fields. In that case, they arise from the tendency of the system to minimize its free energy by redistribution of the charges in order to adjust energy states at surfaces [130]. The SCRs can also be induced by the application of an external field and/or by adsorption of ions from an environment adjacent with a surface.

Due to the high density and mobility of conduction electrons, which cause the effective screening, metals are characterized by very narrow induced SCRs ($\sim$ 1 Å) as compared to semiconductors (order of hundreds of Å) [4] or insulators ($\sim$ 1 μm) [130]. However, the induced charge per interfacial atom in metals (typically, $\approx$ 0.18 electrons/atom [8]) remains localized near the interfacial atoms, and as result may alter local properties more efficiently than in semiconductors, where a similar amount of charge per area is smeared out over a much larger volume [11]. This leads to the idea about modification of overall properties of *high-surface area metallic materials* via controllable manipulation of SCRs by external means as has been outlined in Section 1.1. In this respect, an effective charge carrier redistribution (and the corresponding formation of the SCRs) is successfully realized in solid-fluid (electrolyte) interfaces, where the SCRs occur in both phases.

Electrified metal-fluid interface

Here, an interface between a *flat* metal surface and a dilute aqueous electrolyte is considered. Figure 2.3 shows a schematic diagram of its structure. The interface known as an *electrical double* or a *Helmholtz layer* and consists of the electrical charge at the metal surface and the charge of the ions (equal magnitude and opposite sign) distributed in the solution at a small

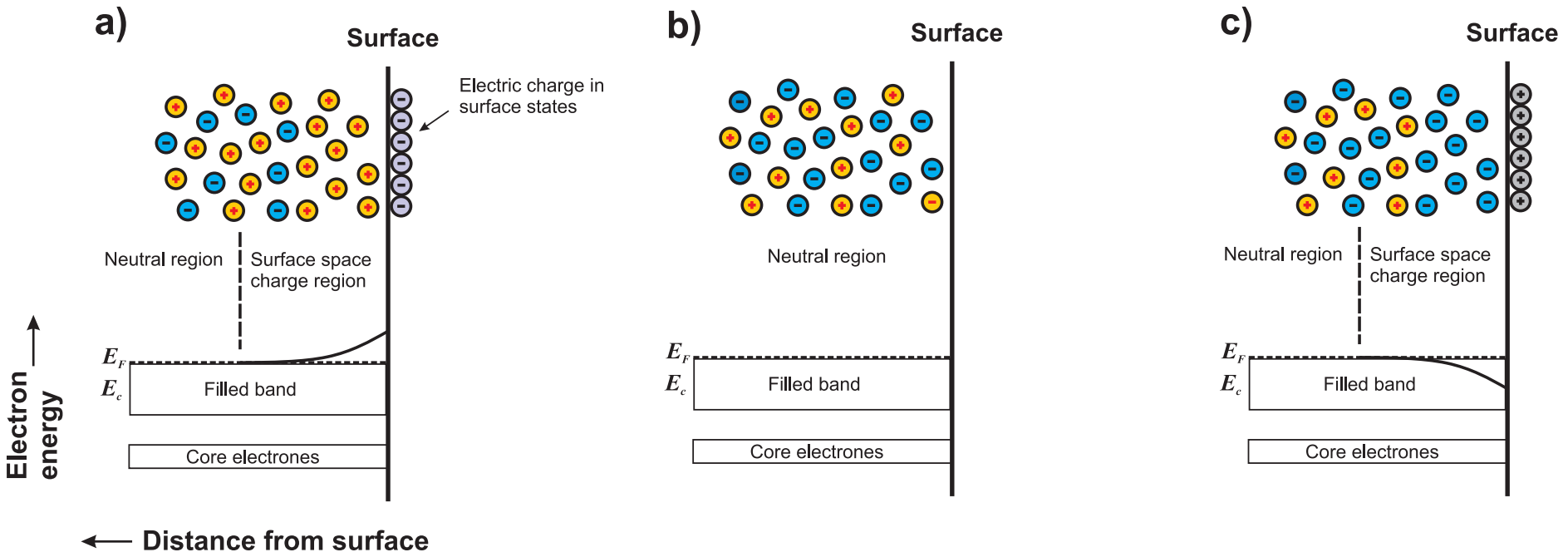

Figure 2.2. Induced changes in a near-surface of a metal due to introduction of an electric charge into the vicinity of the surface (schematic, adapted from Ref. [130]). Upper part: SCRs depending on the nature of the introduced charge (a, c), charge neutrality state (b). Lower part: corresponding energy band diagrams. E_c and E_F is the electron energy at the top of the conduction band and the Fermy energy, respectively. The SCRs separate the near-surface layers (net volume charge density, $Q \neq 0$) from the neutral regions in the bulk ($Q = 0$), as indicated by the vertical dashed lines.

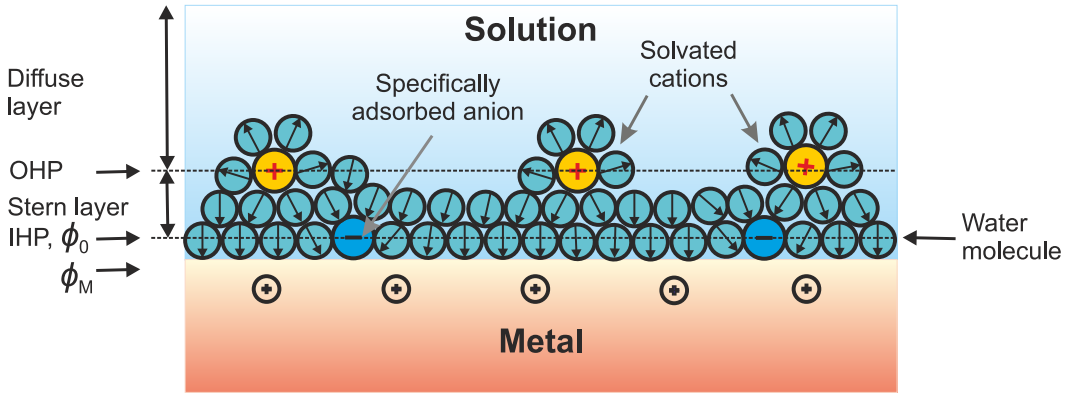

Figure 2.3. A simplified model of a metal-dilute electrolyte interface – *an electric double layer* (after Butt *et al* [111]). The SCR in the metal is not shown owing to its negligibly small thickness compared with one built up in the fluid. The charge distribution in the electrolyte consists of characteristic layers – the Stern, diffuse, and bulk ones (each denotes strength of the metal-electrolyte interaction). ϕ_M is the absolute electrostatic potential of the metallic phase and ϕ_0 is the surface potential (at $x = 0$). The inner (IHP) and outer (OHP) Helmholtz planes are also shown (explanations in text).

distance from the surface. In Fig. 2.3 there is an electron deficiency on the metal surface and the excess ionic charge (more anions than cations) on the solution side of the interface. Since the aqueous electrolyte is considered, water molecules are represented as spheres with a dipole moment. They are bonded to the surface with their dipole moment parallel to the surface as confirmed by theoretical calculations [131]. Ions (larger spheres with a charge at the center) are surrounded by polarized water molecules – *the solvation shells* that screen the fields arising from the ions [131].

Anions that reside in a contact with the surface loose their solvation shells and become desolvated more easily than cations that separated from the surface by the water/solvent molecules [132]. The former are named as *specifically adsorbed ions* and held at the surface by chemical interactions (*chemisorption*), whereas the latter are *non-specifically adsorbed* and considered to interact with the surface only electrostatically [133].

The locus of electrical centers of the desolvated ions is termed the *inner Helmholtz plane* (IHP) while the locus of centers of the solvated ions – the *outer Helmholtz plane* (OHP).

In accordance with Stern theory, an electrolyte in the vicinity of the charged surface can be viewed as one composed of a layer of immobile ions, which directly adsorbed to the surface (Helmholtz or Stern layer) and one, consisting of mobile ions, which obey Poisson-Boltzmann statistics (diffuse or Gouy-Chapmann layer) [111]. Beyond the diffuse layer, the ions are present in concentrations typical of the bulk electrolyte.

Within the Poisson-Boltzmann theory the electric potential $\phi(x)$ distribution in an electrolyte near the homogeneously charged planar surface is described by [7] [111, 134]

$$\phi = \phi_0 e^{-kx} \tag{2.13}$$

with $k = \lambda_D^{-1} = \sqrt{2c_0 z^2 e^2/(\epsilon_0 \epsilon k_B T)}$ the inverse Debye length. Other variables have the following meaning: ϕ_0 – potential at $x = 0$ relative to the bulk solution (a surface potential), c_0 – bulk concentration of each ion in the bulk, z – charge on each ion, e – elementary charge, ϵ_0 – permittivity of free space, ϵ – dielectric constant, k_B – Boltzmann constant, T – absolute

[7] Equations (2.13- 2.14) are derived for a particular case of a symmetric monovalent electrolyte with equal amount of anionic and cationic species (e.g., HCl, NaF). Equation (2.13) is valid for sufficiently low potentials.

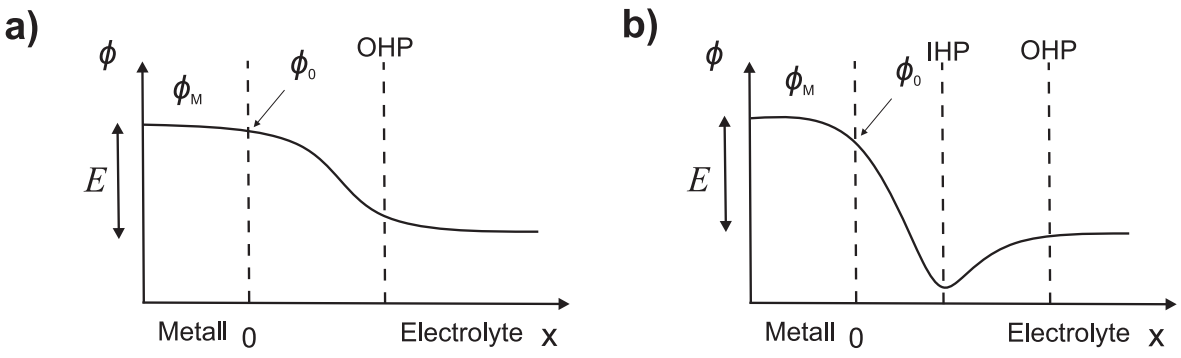

Figure 2.4. Potential profile at the interface between a positively charged metal and a dilute electrolyte in the presence of non-specific (a) and specific (b) adsorption of ions. Redraw after [135].

temperature in kelvins, respectively. Thus, based on Eq. (2.13) the thickness of the SCR built up near the solid surface depends on the charge carrier concentration in electrolyte. In other words, the more ions in a solution, the smaller λ_D and the more effective screening. The diffuse layer becomes essentially compressed into the OHP at high electrolyte concentrations similarly to reducing of the SCRs beneath metal surfaces due to high density of free electrons.

As suggested by Eq. (2.13), the potential in the electrolyte decreases exponentially with increasing distance normal to the surface. Because of the double layer at the metal-electrolyte interface, there is the potential drop across the system, E. Figure 2.4 schematically illustrates the behavior of the electrostatic potential ϕ in the each phase and their boundary in the presence of non-specific (a) and specific (b) adsorption of ions.

The metal-electrolyte interface has been shown experimentally to behave like a capacitor, and its capacitance[8] (per unit area) can be calculated as [111]

$$C_{\mathrm{dl}} = \frac{\mathrm{d}q}{\mathrm{d}\phi_0} = \frac{\epsilon_0 \epsilon}{\lambda_D} \cosh\left(\frac{ze\phi_0}{2k_B T}\right), \tag{2.14}$$

where q represents an excess charge at the metal surface. For sufficiently small potentials Eq. 2.14 simplifies to

$$C_{\mathrm{dl}} = \frac{\epsilon_0 \epsilon}{\lambda_D}, \tag{2.15}$$

meaning that the electric double layer resembles a plate capacitor ($C = \epsilon_0 \epsilon / d$) with an extremely small effective plate separation distance between the plates given by the Debye length $d = \lambda_D$, and thereby a very high capacitance. For a clean metal surface in an aqueous electrolyte C_{dl} attains $15 - 30$ μF/cm^2 [8].

When a potential is applied across the double layer capacitor, the charging or *capacitive, nonfaradaic* current will flow[9], so that a charge is transferred from one plate to another. The applied voltage (potential) drop between a metal and a solution in aqueous solutions is typically of the order of 1 V. Taking into account a typical thickness of the SCRs in electrolytes ($5 - 20$ Å) and in metals (1 Å), there is extremely high fields of up to 10^9 Vm^{-1} can be obtained [132] and large superficial charge densities up to 0.3 As/m^2 accumulated [8] at the electrochemical interfaces. Therefore, the key to effectively manipulate the charge carrier density in the SCRs (and as a result to generate solids with tunable electronic structures [8]) is in applying an external voltage to a high-surface area nanoporous metal immersed in an aqueous

[8] The thermal motion of ions (the Gouy-Chapman model) is considered.

[9] Only the electrode-electrolyte interfaces that approach *ideal polarizability*, i.e. no charge transfer occur across them regardless of the potential imposed, can behave like a capacitor [134]. In such situation reversible adsorption of ions from a liquid phase on solid electrode surface, being a function of electric potential, is termed *electrosorption*.

electrolyte. Nanoporous Au satisfies all the requirements for this application, including high conductivity, electrochemical stability and open porosity.

2.3.2 Electrocapillarity of metal electrodes

A substantial information about the capillary forces of solids comes from measurements of the surface tension and surface stress of metal electrodes under applied potentials in electrolytes. Below, as relevant to the present work, a metal electrode in a fluid electrolyte which is at constant pressure is considered.

The two capillary parameters surface tension γ and surface stress f respond to changes in the applied potential[10] or in the superficial charge density in distinctly different ways [9]. The variation in γ for an ideal polarized electrode is described by the fundamental Gibbs adsorption equation [9]

$$\mathrm{d}\gamma = -s\mathrm{d}T - \Gamma_i \mathrm{d}\mu_i - q\mathrm{d}E + \mathbf{s}\mathrm{d}\mathbf{E}^{\mathsf{S}}. \tag{2.16}$$

Here, s – superficial excess entropy (entropy per surface area), T – temperature, Γ_i – superficial excess of ith component at the surface, μ_i – chemical potential of the species i in the electrolyte, q – superficial charge density, E – electrode potential, $\mathbf{s}$ – surface stress tensor, $\mathbf{E}^{\mathsf{S}}$ – tangential strain tensor at the surface.

For the case of constant T and μ_i (constant composition), and $\mathbf{E}^{\mathsf{S}}$ (stiff electrode) Eq. (2.16) yields *the Lippmann equation*:

$$\left.\frac{\mathrm{d}\gamma}{\mathrm{d}E}\right|_{T,\mu_i,\mathbf{E}^{\mathsf{S}}} = -q. \tag{2.17}$$

From Eq. (2.17) it follows that the excess charge on the electrode is determined by the slope of a surface tension-potential dependance $\gamma(E)$ (electrocapillary curve). By integrating Eq. (2.17), taking into account the double layer capacitance $C_{\mathrm{dl}} = \mathrm{d}q/\mathrm{d}E$, and assuming that C_{dl} is potential-independent, one obtains:

$$\gamma - \gamma_0 = -\frac{1}{2}C_{\mathrm{dl}}(E - E_0)^2 = -\frac{1}{2}\frac{q^2}{C_{\mathrm{dl}}}. \tag{2.18}$$

This relationship implies the nearly parabolic shape of the electrocapillary curve and at point where $E = E_0$ surface tension passes through a maximum. Since the slope of $\gamma(E)$ is zero there and hence the surface becomes uncharged ($q = 0$), the potential at which the electrocapillary maximum occurs is known as the *potential of zero charge* (pzc) $E_0 = E_{\mathrm{zc}}$.

The variation of the surface stress with the charge density is described by *the electrocapillary coupling parameter* ς, [9]

$$\varsigma = \left.\frac{\mathrm{d}f}{\mathrm{d}q}\right|_{T,\mu_i,\mathbf{E}^{\mathsf{S}}}. \tag{2.19}$$

In contrast to γ, f has been found to show a linear dependence on q at the *pzc*, and whose relative variation is much larger than γ [9, 113]. Experiments on planar metal electrodes in aqueous electrolytes with weak anion adsorption detect ς parameter negative and in the range of $-1 \ldots -2$ V near the *pzc* [113, 136], confirming the tensile surface stress for clean surfaces. For nanoporous metals in the same solutions, ς is in the order of -2 V [137]. Hence, the experiments demonstrate that clean metal surfaces tend to expand laterally when charged positively, and this trend agrees well with density functional theory (DFT) computations ([7] and references therein). In the case where adsorption/desorption of oxygen species is involved at interface, clean metal surfaces or nanoporous metals also have a tendency to expansion.

[10] Here and further in the work, "applied potential" is interchangeably used with "electrode potential".

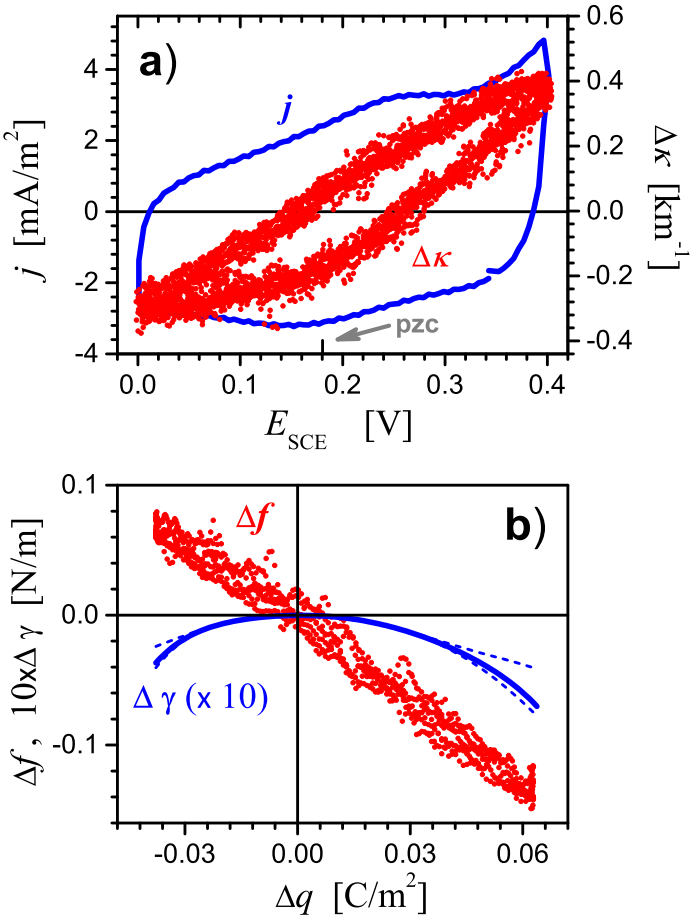

Figure 2.5. Experimental verification of fundamentally different behavior of surface stress, f, and surface tension, γ, for the case of Au electrode under conditions of weak ion adsorption: (a) cyclic voltammogram (blue line) recorded in 7 mM NaF electrolyte vs. the standard calomel electrode, SCE. During the potential cycling changes in a curvature, $\Delta\kappa$, of the electrode was monitored (red dots), from which the surface stress was evaluated [136]. (b) Surface stress, Δf, and surface tension, $\Delta\gamma$ variations with surface charge density q, near the *pzc*. $\Delta\gamma$ was determined based on the cycling voltammogram using Lippman equation (2.17). Note a significant variation of f compared with γ. Adapted from [9].

Figure 2.5b shows the way parameters γ and f behave near the *pzc* for Au(111)-textured electrode in aqueous electrolyte of NaF, confirming a qualitatively different nature of the capillary forces. The variation of the surface stress was obtained experimentally by a cantilever-bending experiment [136] and the surface tension was computed from cyclic voltammogram (Fig. 2.5a) using Lippman equation (2.17) [9].

2.3.3 Thermodynamic description of electrode mechanics

As a background for discussing the mechanics of np-Au/electrolyte interface, an abbreviated account of the thermodynamic analysis of Refs. [9, 112] will be exposed below. The analysis focuses on the equilibrium between a conductive solid and a fluid electrolyte into which it is immersed.

Consider a stress-free solid metal electrode B with the surface S that is surrounded by a fluid electrolyte F, and both the metal and the electrolyte are at constant temperature and constant chemical composition. Assume also that an electric potential E is applied to the electrode and the metal-electrolyte interface satisfies a condition of the ideal polarizability (no electrons/charge are exchanges between the metal and the electrolyte). *The total (Gibbs) free energy* G of the system is defined as

$$G = F - EQ - \mu_i N_i, \tag{2.20}$$

where F is the total Helmholtz free energy, E is the electrode potential, Q is the total electric charge, μ_i is the chemical potential and N_i is the number of charged particles of the ith sort in the system.

The solid undergoes anisotropic and nonuniform elastic deformation caused by the pressure in the fluid and by the surface stresses. The elastic strain in the solid bulk is induced by the surface stress in accordance with Eq. (2.10). Then a variation of G at constant μ_i, E, and V will obey

$$\delta G = \delta F - E\delta Q - \mu_i \delta N_i = \int_{\mathsf{B}} \Psi^{\mathsf{B}} \mathrm{d}V + \int_{\mathsf{F}} \Psi^{\mathsf{F}} \mathrm{d}V + \int_{\mathsf{S}} \psi \mathrm{d}A - E\delta Q - \mu_i \delta N_i. \tag{2.21}$$

Here, a variation of the total Helmholtz free energy δF is described by the sum of *free energy densities* (per volume) of the bulk phases: Ψ^{B} for the electrode and Ψ^{F} for the electrolyte, and by the *superficial free energy density*, ψ (per area of the electrode surface S); $E\delta Q$ is the work done on moving the total electronic charge Q to the metal surface, $\mu_i \delta N_i$ is the work done in adding an ion from bulk of the electrolyte to the SCRs near the surface; V and A denote volume and surface area of the electrode, respectively[11].

Assume further that the elastic deformation imposed on the solid is a small, so that the constitutive assumption for Ψ^{B} can be defined based on results of continuum mechanics with the strain tensor $\mathbf{E}^{\mathsf{B}}$ as a state variable

$$\Psi^{\mathsf{B}} = \Psi^{\mathsf{B}}(\mathbf{E}^{\mathsf{B}}, \mathbf{x}) \tag{2.22}$$

$$\mathrm{d}\Psi^{\mathsf{B}} = \boldsymbol{\sigma} \mathrm{d}\mathbf{E}^{\mathsf{B}}, \tag{2.23}$$

where $\boldsymbol{\sigma}$ the stress tensor in the solid bulk.

The constitutive assumption and fundamental equation for the electrolyte are

$$\Psi^{\mathsf{F}} = \Psi^{\mathsf{F}}(\rho_i) \tag{2.24}$$

[11] Following the notation in Refs. [9, 112], Ψ^{B} and ψ are densities per volume or area in Lagrangian coordinates, whereas Ψ^{F} is in Eulerian (laboratory) coordinates. Changes in the surface area due to *reversible plastic* deformation are not considered in the analysis. This means that V and A measured in the undeformed state of the solid are independent of strain.

$$\mathrm{d}\Psi^{\mathsf{F}} = \mu_i \mathrm{d}\rho_i, \tag{2.25}$$

where ρ_i the density of the i-th component in the electrolyte representing the state variable and μ_i the chemical potential.

The free energy density of the surface ψ in the most general case is allowed to depend on the state of the abutting bulk phases (B and F) through $\mathbf{E}^{\mathsf{S}}$ the strain and $\rho_{\mathsf{S},i}$ the density in the fluid at the surface. Additional state variables for ψ represent merely the state of the electrode surface: $[\mathbf{u}]$ the jump in the displacement and Γ_i the excess (per area) of the species i at the surface, $\mathbf{x}_{\mathsf{S}}$ the position vector on the surface

$$\psi = \psi(\mathbf{E}^{\mathsf{B}}, [\mathbf{u}], \rho_{\mathsf{S},i}, \Gamma_i, \mathbf{x}_{\mathsf{S}}) \tag{2.26}$$

$$\mathrm{d}\psi = \mathbf{s}\mathrm{d}\mathbf{E}^{\mathsf{S}} + y_i \mathrm{d}\rho_{\mathsf{S},i} - \mathbf{p}\mathrm{d}[\mathbf{u}] + \mu_i^{\mathsf{S}} \mathrm{d}\Gamma_i, \tag{2.27}$$

where the coefficients $\mathbf{s}$, y_i, $\mathbf{p}$, and μ_i^{S} are defined as partial derivatives of ψ with respect to the state variables [112]

$$\mathbf{s} = \left.\frac{\partial \psi}{\partial \mathbf{E}^{\mathsf{S}}}\right|_{\rho_{\mathsf{S},i},[\mathbf{u}],\Gamma_i} \tag{2.28}$$

$$\mathbf{p} = -\left.\frac{\partial \psi}{\partial [\mathbf{u}]}\right|_{\mathbf{E}^{\mathsf{S}},\rho_{\mathsf{S},i},\Gamma_i} \tag{2.29}$$

$$y_i = -\left.\frac{\partial \psi}{\partial \rho_{\mathsf{S},i}}\right|_{\mathbf{E}^{\mathsf{S}},[\mathbf{u}],\rho_{\mathsf{S},j\neq i},\Gamma_i} \tag{2.30}$$

$$\mu_i^{\mathsf{S}} = -\left.\frac{\partial \psi}{\partial \Gamma_i}\right|_{\mathbf{E}^{\mathsf{S}},\rho_{\mathsf{S},i},[\mathbf{u}],\Gamma_i}. \tag{2.31}$$

It should be emphasized that the above equations are valid for solid-electrolyte interfaces of *arbitrary curvature*. Therefore, they are suitable to analyze behavior of a nanoporous solid immersed into an electrolyte. The analysis in this work will be restricted to isotropic surfaces with the scalar variables of the surface stress f ($f = \frac{1}{2}\mathrm{tr}\mathbf{s}$) and the surface strain e ($e = \frac{1}{2}\mathrm{tr}\mathbf{E}^{\mathsf{S}}$), which represents the relative change in physical area, A, during deformation $\delta e = \delta A/A$. The restriction is appropriate for surfaces with at least threefold rotational symmetry [138], such as the dense-packed surfaces of face-centered cubic metals in the limit of small strain.

Based on the assumptions above is has been shown in [9] that the fundamental Eq. (2.27) for the surface free energy density function can be simplified to

$$\mathrm{d}\psi = f\mathrm{d}e + E\mathrm{d}q. \tag{2.32}$$

Equation (2.32) will be profitably used during discussion of the elastic behavior of np-Au as a function of varied surface charge.

Chapter 3

Materials and experimental procedures

3.1 Electrochemical equipment and electrolytes for materials synthesis and characterization

3.1.1 Electrochemical cells and electrodes

In an electrochemical experiment, careful cleaning of electrochemical ware and all parts that come in contact with an electrolyte are critically important for preventing contamination by foreign ions and obtaining reproducible results. For these purposes the electrochemical cells (ECs) and all glassware used in the current work were cleaned by soaking in a piranha solution, a mixture of 95% H_2SO_4 and 30% H_2O_2 with a ratio of $5:1$ to clean organic residues followed by through rinsing in ultrapure water (Ultra Clear TWF UV TM, Siemens). Purity of the water was characterized by a resistance of 18.2 $M\Omega \cdot cm$ and total organic carbon content (TOC-value) of $\leq 3-4\ mg \cdot L^{-1}$.

Three-electrode cell configuration was used in all electrochemical studies in this work, whose typical setup is schematically shown in Fig. 3.1. In this configuration the potential of the working electrode (WE), one where the reaction of interest occurs, is maintained relative to the reference one (RE), and the resulting current then passes between the WE and a separate counter (or auxiliary) electrode (CE).

General requirements for a RE as a reliable reference for potential control include stability over time and changing temperature, fixed and reproducible electrode potentials [133]. To synthesize specimens by electrochemical dealloying as well as electrochemical measurements in miniaturized ECs designed in this work for mechanical testing (Sections 3.5.1, 3.5.2) a pseudo silver/silver chloride (Ag/AgCl electrode) was chosen as the RE due to simplicity, nontoxic components, and its compact size in the small cell arrangements compared to standard commercial REs. The pseudo REs were prepared by electrolytic formation of AgCl coating on a Ag wire (0.5 mm diameter, Ag 99.9985%, Alfa Aesar) in 1 M HCl at 1 V constant potential applied against another Ag wire (serving as CE and RE). The deposition was accomplished after ~ 40 s, the coated wire was then immediately washed with ultrapure water and further kept in 18.2 $M\Omega \cdot cm$ water bath. Prior to the deposition, the surface of the Ag wire was renovated from any oxide by mechanical polishing or dipping in the piranha solution followed by careful rinsing with 18.2 $M\Omega \cdot cm$ water. Before inserting a pseudo RE directly into the electrolyte under study, the electrode was calibrated in the same solution relative to the standard hydrogen electrode (SHE, HydroFlex®, Gaskatel), using a voltmeter. The calibrated values are listed in Tab. 3.1 for all used electrolytes. For comparison of results obtained in the different solutions all potentials in this work are quoted vs. SHE.

The third electrode, CE, is generally chosen to be inert under the reaction conditions and

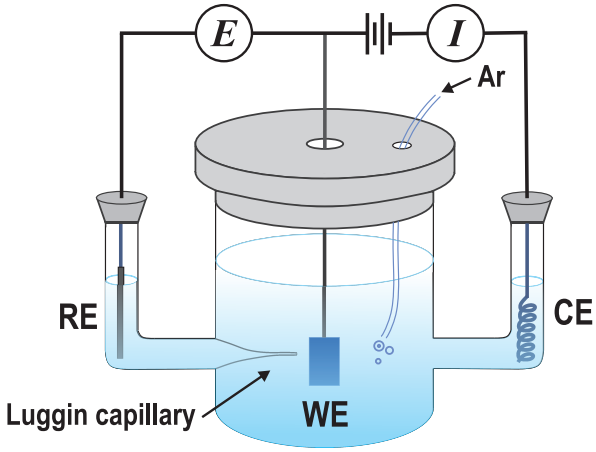

Figure 3.1. Schematic experimental setup of a three electrodes electrochemical cell (EC). Working (WE), reference (RE), and counter (CE) electrodes are indicated. A fine tip of the Luggin capillary allows sensing of the potential in close proximity to the WE. The cell can be purged with inert gas (e.g., Ar or N_2) to prevent oxygen interference in electrode reactions at the WE.

Table 3.1. Selected aqueous electrolytes, their pH values, and potentials of a pseudo RE measured in these solutions with respect to SHE.

Electrolyte	pH	E vs. SHE [V]
0.7 M NaF (99.99%, Suprapur, Merck)	7.28	0.900 ± 0.010
1 M $HClO_4$ (70%, Suprapur, Merck)	0.44	0.515 ± 0.010
0.5 M H_2SO_4 (96%, Suprapur, Merck)	0.29	0.530 ± 0.010
1 M $HClO_4$ + 1 mM NaCl (99.99%, Alfa Aesar)	0.24	0.400 ± 0.010
0.5 M H_2SO_4 + 1 mM NaBr (99.99%, Alfa Aesar)	0.40	0.420 ± 0.010

balance a reaction that occurs at the WE [133]. To supply current density that is constant across the WE, the CE is usually made of similar or larger area. For dealloying, a coiled Ag wire (99.9985%, Alfa Aesar) was used as the CE, which was placed in a separate fritted tube in order to avoid interference of electrode products formed at the CE with a reaction on the WE. For *in situ* experiments a porous carbon cloth (specific surface area 1200 – 1750 m^2/g, Kynol Europa GmbH) was accommodated in the ECs by means of either Pt or Au wires.

Electrochemical measurements were performed using a potentiostat/galvanostat PG-STAT 302N (Metrohm AUTOLAB) equipped with a FI20-integrator module (for a current integration within the staircase cycling voltammetry method, Section 3.2.2) and FRA32M module (for electrochemical impedance spectroscopy, Section 3.2.3), and controlled by the NOVA software.

All the experiments were carried out at room temperature and when exposed to air.

3.1.2 Electrolytes

Within the thesis work, aqueous solutions of 0.7 M NaF, 1 M $HClO_4$, 0.5 M H_2SO_4, 1 M $HClO_4$ + 1 mM NaCl, and 0.5 M H_2SO_4 + 1 mM NaBr were employed, which were prepared from reagent grade chemicals (Merck, Alfa Aesar) in 18.2 $M\Omega \cdot cm$ water. The electrolytes were deaerated with argon for at least 1 h directly before use. The electrolyte 1 M $HClO_4$ used for dealloying (Section 3.3.2) was not deaerated as this has been reported to have no effect on the electrochemical characteristics of dealloying in Ag-Au systems [139]. Acidity/basicity of the solutions are summarized in Tab. 3.1 based on the pH-measurements at $T = 21\,°C$ (pH

meter FE20/FG2, Mettler Toledo).

3.2 Electrochemical techniques

3.2.1 Chronoamperometry

In the thesis chronoamperometry technique (CA) was utilized for materials synthesis by electrochemical dealloying (Section 3.3.2) and for monitoring the effective elastic modulus and flow stress response to the electrode potential changes (Chapter 4).

In this method, a sequence of constant and fixed potential steps with defined time intervals are imposed to WE and the resulting current is recorded continuously against the time. Figure 3.2 exemplifies a CA experiment on np-Au in 1 M $HClO_4$ with three potential-excitation steps and the corresponding current-time curve.

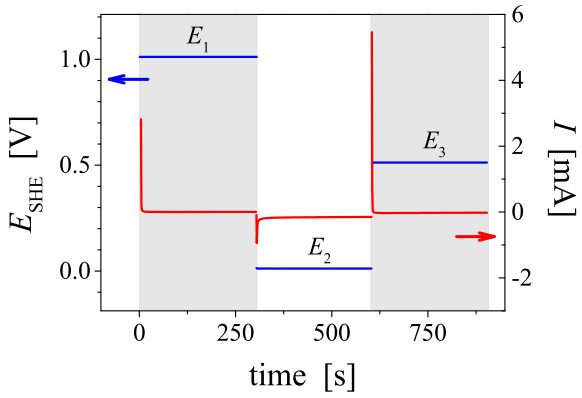

Figure 3.2. Typical potential step chronoamperometry of np-Au in 1 M $HClO_4$: potential step waveform (blue solid line) and current response vs. time (red solid line).

3.2.2 Cyclic voltammetry

Cyclic voltammetry technique (CV) was widely used to characterize np-Au, to coarsen as-dealloyed structure (Section 3.3.3), and tune the material surface state during *in situ* mechanical testing (Chapter 4).

In the method, the potential applied on WE is varied in a triangular manner at a chosen scan rate, $v = dE/dt$, between preselected upper, E_2, and lower, E_1, vertex potentials (Fig. 3.3a). The scan direction is reversed when the potential reaches E_2, returning to the initial value E_1. The resulting current I response plotted vs. potential E for the forward (anodic[1]) and backward (cathodic) potential scans constitutes one cycle of the cyclic voltammogram (CV), and multiple cycles may be recorded.

The CV method generally offers a convenient way of studying electrosorption processes on noble metals, particularly formation of surface oxides [140]. Yet, it should be noted that the sensitivity of resolving different electrochemical reactions on a surface is exclusively determined by choice of the proper v, which sets the timescale of the experiment. Because of the sensitivity of the CV technique to electrochemical experimental conditions different surface processes on WE can be identified[2].

Figure 3.3b illustrates a typical CV of np-Au recorded in 1 M $HClO_4$ electrolyte with a scan rate of 1 mV/s at room temperature. A large peak on the anodic side of the I-E profile

[1] In this thesis, an anodic current is taken as positive.

[2] This includes also signatures of impurities in chemical composition either electrolyte or WE that are manifested on CV by extra peaks.

(region II) corresponds to oxidizing conditions at the electrode/solution interface and this, result in up to a monolayer formation of oxygen species at the Au electrode surface [140]. The peak following after, on the cathodic side, defines the corresponding reduction of the species array from the surface. The entire process of adsorption the surface oxide film and its subsequent desorption is a reversible process. In a potential window denoted as region I the current is associated with charging/discharging of the double layer (Section 2.3.1). An extra peak here, at around 0.6 V in the anodic scan, originates from dissolution of the residual Ag [141] that is usually retained in small fractions in np-Au after synthesis by dealloying.

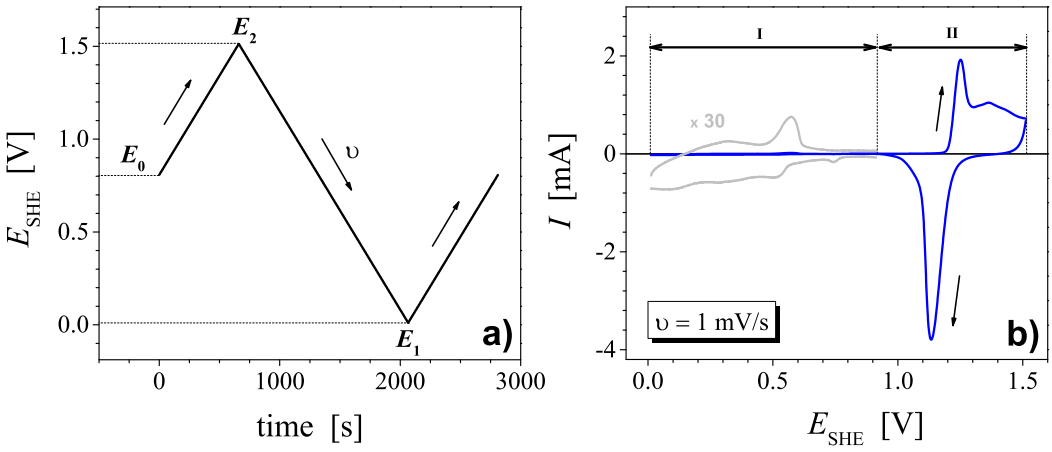

Figure 3.3. Typical cyclic voltammetry experiment on a high surface area np-Au electrode: (a) Potential waveform with the scan rate v showing the starting potential E_0 (OCP), lower E_1, and upper E_2 potential limits. (b) Cyclic voltammogram recorded in 1 M $HClO_4$ with 1 mV/s at room temperature. Surface states are identified by regions I and II (explanations in text). Grey line: magnified current in region I. Anodic and cathodic directions of scan (towards positive and negative potentials, respectively) are denoted by arrows.

In the thesis, *staircase*[3] CV was chosen due to the advantage of using very slow scan rates (< 10 mV/s) in electrochemical experiments as compared with a linear scan mode [142]. This method, however, not desirable when studying fast electrode processes since it minimizes capacitive current that prevails at the beginning of the step. Therefore, *current integration* option was applied within the staircase CV. In this case rather than sampling the current at the end of each step, the total charge, which has passed during the whole interval time, is accumulated in the integrator. At the end of each step, the accumulated charge is then reconverted in current, thereby including both the faradaic and the capacitive components passed during the potential step [142].

In most of the electrochemical experiments, a CV cycle was started from *open circuit potential* (OCP) value denoted in Fig. 3.3a as E_0. OCP is an equilibrium potential of a WE that characterizes an electrochemical state of its surface with respect to a RE at no current flowing through the cell. Within the CV procedure the OCP was monitored vs. time and the average value was used for the consequent potential scans.

3.2.3 Electrochemical impedance spectroscopy

An electrochemical impedance spectroscopy (EIS) technique was performed for determination of a capacitance of np-Au samples. Based on these data an electrochemically active surface

[3]The staircase mode implies imposing small potential steps when going from lower to upper vertex potentials. The current response is then measured at the end of each step contrary to the continuous recording of the current in the linear scan mode [142].

area was estimated (Section 3.4.2). The capacitance of an electrode can be derived from the EIS spectra as follows.

In a typical EIS measurement, WE is subjected to a periodic (usually sinusoidal) AC signal with a defined frequency and a small amplitude, which is superimposed on the applied to the cell DC potential or current [133]. The AC voltage and current components are then analyzed, and the total impedance of the electrochemical cell (Z) is calculated, together with the phase angle shift (ϕ), the real (Z'), and imaginary (Z'') components of the total impedance. The total impedance Z and the phase angle shift ϕ are given by [134]:

$$Z = Z' - iZ'' \tag{3.1}$$

$$\tan\phi = \frac{Z''}{Z'}. \tag{3.2}$$

For a given electrode, in the absence of faradaic processes, EIS measurement can be interpreted via electronic circuit, containing one resistor (R) in series with a capacitor (C_{dl}), where both elements represent the ohmic solution resistance and the capacitance of the double layer, respectively [133, 134]. Thus, the total impedance of the metal-solution interface can be expressed as:

$$Z = R - i\frac{1}{\omega C_{\mathrm{dl}}}. \tag{3.3}$$

By equating Eq. (3.1) with Eq. (3.3) the capacitance can be calculated based on the experimentally obtained imaginary part of the impedance[4], Z'', and the angular frequency of the applied AC signal, ω:

$$C_{\mathrm{dl}} = \frac{1}{\omega Z''}. \tag{3.4}$$

To choose a suitable frequencies range for the EIS experiment on np-Au the following steps were applied, adapting the procedures from Refs. [141, 143–145]:

1. Measurement of the imaginary part of the impedance $-Z''$ as a function of $\nu = \omega/2\pi$ in a wide frequency diapason (in the present work ν = 1 mHz – 1 kHz, Fig. 3.4a).

2. Selection of a frequency range where the $-Z''$ dependence on ν exhibits a slope close to −1. At these frequencies a Nyquist plot ($-Z''$ vs. Z') approaches a straight vertical line, a characteristic of a purely capacitive response [145] (Fig. 3.4b).

3. Fitting a plot of $-Z''$ vs. ω to obtain double layer capacitance C_{dl} as the average value for the preselected frequency range (Fig. 3.4c).

The EIS measurements were conducted at fixed value of the DC potential (potentiostatic conditions) in the capacitive region in order to avoid the occurrence of any faradaic reactions on the np-Au, and ensure only double-layer charging. The impedance spectra were recorded over the range of frequencies 0.1 – 1 Hz with the logarithmic distribution per decade using a peak amplitude of AC potential of 0.014 V amplitude

3.3 Samples

3.3.1 Alloy preparation

This work is a study of nanoporous samples based on the $Au_{25}Ag_{75}$ precursor alloy system. The preparation of the alloy involved the melting of Ag and Au wires (Ag ≥ 99.99%, Au

[4] In electrochemistry, the imaginary part of the impedance in most of the cases is capacitive and has a negative value [134]. In Nova software used in this work for all impedance measurements a sign convention for Z'' is also assumed with "–". However, further in the text Z'' is given with a minus sign to prevent confusion.

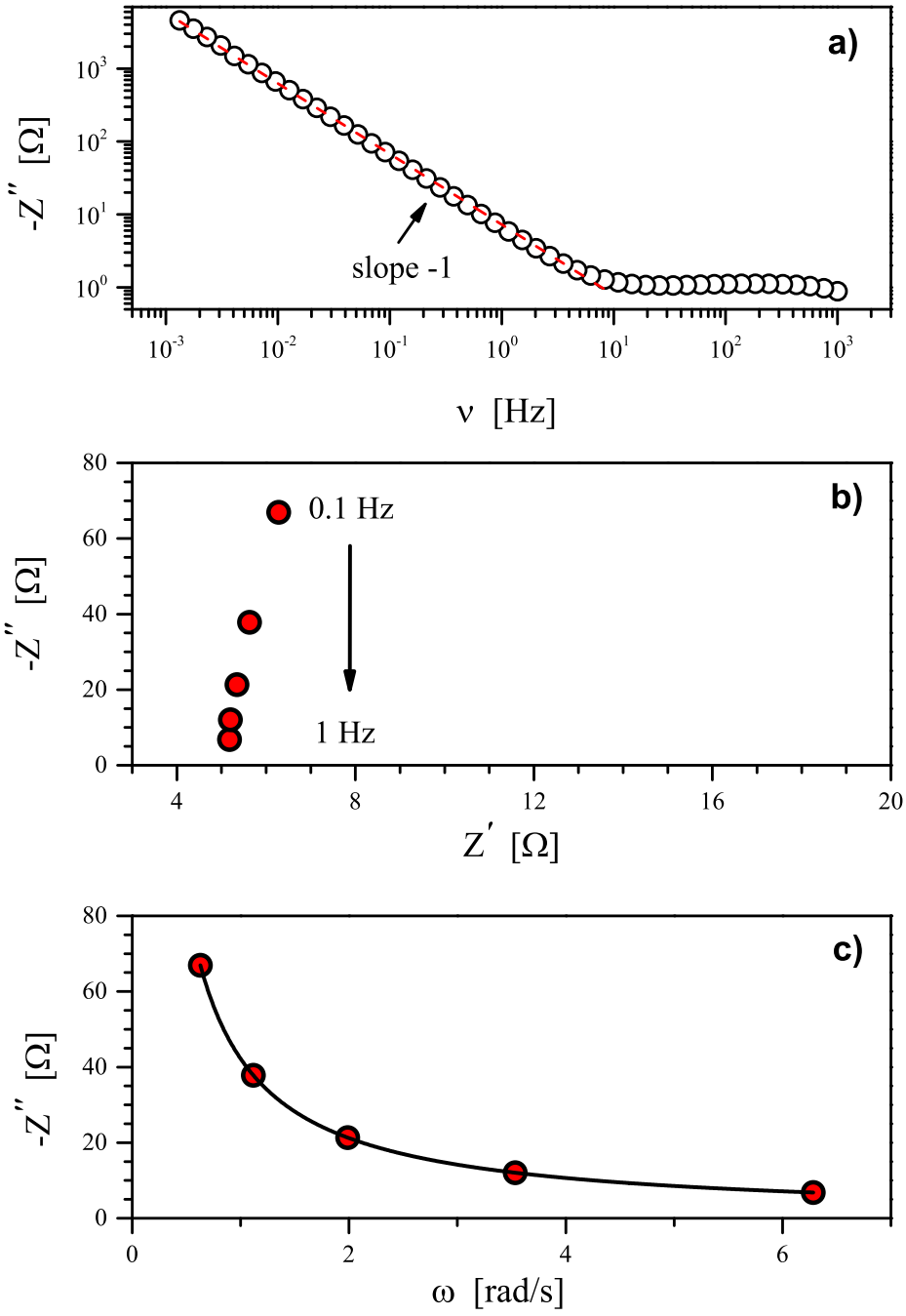

Figure 3.4. Determination of the double layer capacitance of a np-Au/1 M $HClO_4$ interface by electrochemical impedance spectroscopy (EIS). (a) Plot of the imaginary part of the impedance $-Z''$ vs. frequency ν, where a frequency region from 0.1 to 1 Hz is associated with ideal capacitive behavior. (b) $-Z''$ vs. Z' (Nyquist plot) for different values of ν. (c) Dependence of the imaginary part $-Z''$ on the angular frequency ω. The impedance measurement was performed at DC potential of 0.8 V vs. SHE using a peak AC amplitude of 0.014 V.

≥ 99.99%, Sigma-Aldrich) in Ar atmosphere using arc melter (MAM-1, Edmund Bühler). The solidified ingots (≈ 2 – 3 g) were then sealed in an evacuated (~ 10^{-2} bar) quartz tube and subjected to a homogenization treatment between 850 and 900 °C for 120 h (furnace RHF1600, Carbolite). Each ingot was machined into a wire of 1.2 – 1.4 mm diameter by means of a wire-drawing machine. Finally, the wires were sectioned by a diamond wire saw (Model 3032-4, Well) and annealed for 2 h at 650 °C (or for 1 h at 800 °C) in a quartz tube purged with flowing Ar (infrared furnace behr IRF 10, behr Labor Technik) to relieve any residual stresses.

3.3.2 Electrochemical dealloying

The *electrochemical dealloying* was applied to the $Au_{25}Ag_{75}$ alloy to form nanoporous structure. In corrosion science, the process refers to selective dissolution of one or more electrochemically active components out of an alloy, leaving uniform, random, and bicontinuous open structure that consists almost entirely of the more noble alloy constituents [146]. Here, the selective etching of the less noble element is driven by applying an electrochemical potential in electrolytes, where better control over a pore size can be achieved compared to *free dealloying* without applied external potentials [147]. The applied dealloying potential defines the dissolution rate of a less noble component. The finer porosity is usually a result of the higher dealloying potentials, far above the critical value that sets the rapidly rising dissolution current [147]. However, faster dealloying in Au_xAg_{1-x} solid solutions inevitably leads to large volume shrinkage accompanied by crack generation [69]. Therefore, the critical potential for dealloying must be taken with a great care in order to enable a successful mechanical testing of a nanoporous material.

The choice of the alloy composition $Au_{25}Ag_{75}$ in the present work satisfied the main requirements [148, 149] to accomplish selective removing of Ag and to form the uniform nanoporous structure:

- The Ag-Au alloy system displays a single-phase solid solubility across entire composition range and no phase separation occurs during dealloying [69].
- Electrochemical activity of the alloy components measured by the standard reduction potential, E_0, differ considerably, exceeding a generally accepted limit of 0.5 V (vs. SHE) between the active and the noble component [148, 150], i.e.

$$\Delta E_0 = E_0(Au) - E_0(Ag) = 1.42\ V - 0.799\ V = 0.621\ V. \tag{3.5}$$

- The atomic fraction of more noble metal in the precursor alloy (parting limit) is in the range required to fabricate mechanically stable macroscopic nanoporous specimens and to avoid the surface passivation (for most precursor systems, the parting limit within 20 – 60 at. %).
- A surface diffusion of Au (1.2×10^{-14} $cm^2 \cdot s^{-1}$ [151]) is high enough to ensure the evolution of nanoporosity simultaneously with the dissolution of Ag.

The $Au_{25}Ag_{75}$ cylindrical specimens were dealloyed at a constant potential E_D = 1.26 V vs. SHE using CA method (Section 3.2.1) in 1 M $HClO_4$ (60% $HClO_4$, ACS grade, Merck) at ambient temperature, serving as a WE in the three-electrode EC (Fig. 3.1). The choice of the dealloying potential is based on a dealloying protocol of Ref. [15] due to no crack formation during the synthesis and good mechanical stability of the final structure.

As a criterion for completion of the dissolution process, the procedure was interrupted when the current decayed below 10 μA. To remove the residual acid and promote elimination of Ag^+ ions from the nanopore channels, the samples were transferred into ultrapure water and kept for ≥ 12 h. After rinsing with water the as-dealloyed samples underwent further post-dealloying treatment as described below.

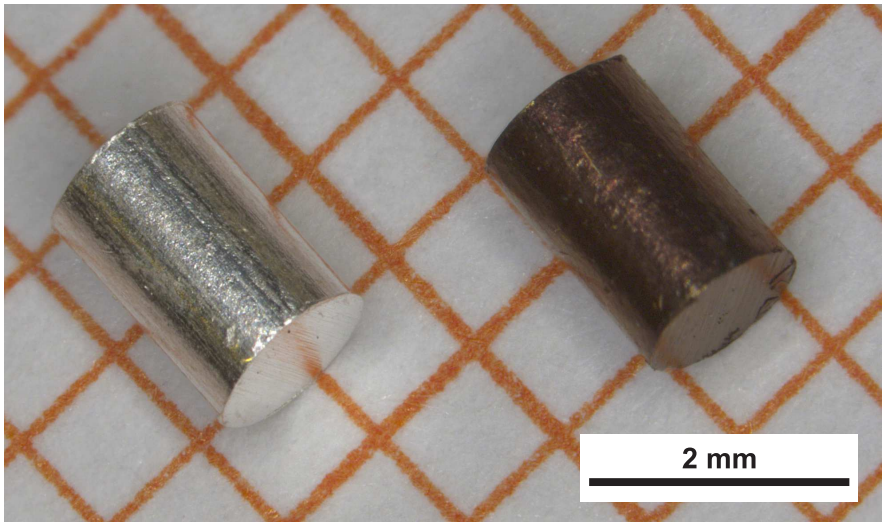

Figure 3.5. A photograph of the $Au_{25}Ag_{75}$ alloy before (left) and after dealloying (right).

3.3.3 Tuning of ligament size

The structure of the as-dealloyed nanoporous samples was tuned by coarsening of ligaments either by electrochemical or thermal annealing. The former treatment is caused by smoothening of the surface in contact with an electrolyte induced by a potential, where the potential exerts a similar effect as a raise in temperature[5]. Although the thermal heating can produce the pore and ligament sizes up to the micrometer scale while maintaining an open porosity [68], the electrochemical annealing was preferable due to capability of controlling the surface state of the as-dealloyed structure. This was realized by monitoring a OCP value and recording a CV (Section 3.2.2) immediately after dealloying.

Due to the fact that the dealloying potential E_D resides near the region of oxide formation on Au (Fig. 3.3b) and in accordance with reports in [70, 153, 154] the presence of an oxide film on the surfaces of ligament (with at least low coverage) is expected. It is vital for thermal stability of a nanoporous structure, but can cause a deleterious effect on its deformability. For that reason, the as-dealloyed specimens were subjected to reduction treatments before mechanical testing or further processing by thermal annealing. As has been pointed out in [147], such reduction is important not only for clean surface electrochemistry but also for reproducible thermal anneals.

This work focused on the following three types of samples with different ligament diameter L_D, adapting the procedures developed in [15]:

1. *Surface oxide layer reduction (SOL reduction),* $L_D \sim 20$ *nm.* The as-dealloyed samples (Section 3.3.2) were underwent 15 potential cycles in the interval 0.01 to 1.01 V with a scan rate of 5 mV/s to ensure removing surface and subsurface oxide and to provide compressive ductility of np-Au for mechanical testing just after dealloying.

2. *Reduction,* $L_D \sim 35-45$ *nm.* Potential cycling in a wider range, between 0.01 and 1.51 V, for 15 cycles with the same scan rate of 5 mV/s. Alternatively, the as-dealloyed samples were first polarized at 1.61 V until the current dropped below 10 μA, and then where reduced by above mentioned method but for 20 cycles. The both approaches were found to lead to similar feature sizes.

[5]The phenomena has been previously observed in smooth Au and Pt electrodes ([152] and references therein).

Figure 3.6 illustrates a typical CV of 20 successive potential cycles recorded in 1 M $HClO_4$ during chemical annealing of as-dealloyed np-Au. The first scan begins at OCP value of around 1.35 V and is characterized by a virtually absent adsorption of OH species. In this case the formation of the gold oxide took place earlier, during the mentioned above polarization, and the metal-electrolyte interface exhibit a capacitive regime on oxygen-covered surface. On the cathodic side of the CV, the first desorption peak is a large and irreversible. The remaining adsorption-desorption peaks display a reproducible behavior with a gradual decrease of the area under the peaks, which is a signature of coarsening of the porous structure [70].

The desorption feature in the first cycle is remarkable. Even though its origin has been attributed to the reduction of a superficial oxide layer, the species that involved in the process were not identified. One can assume that apart gold surface oxides or hydroxides, the reduction also involves the silver oxides. The assumption is prompted by an abnormal positive sign of the surface stress-charge coefficient, ς, for both, Ag electrodes [155] and np-Au covered by an oxygen, just after preparation [70], where a silver passivation layer might have been formed on the surface of the gold. This is, however, not readily consistent with dealloying conditions here (1 M $HClO_4$, pH = 0.29), since – as indicated by the Pourbaix diagram of silver [156] – stable silver oxides can be produced in alkaline solutions at pH > 7. Nevertheless, as has been argued in [157], a pH-value in the pore space, at the corrosion front, can be indeed shifted to more alkaline one due to oxygen evolution that is thermodynamically likely to occur at voltages of > 1.2 vs. SHE. This explanation appears to be adequate here in view of the expected similarity of the corrosion behavior of Ag-Au and Cu-Au alloys studied in [157].

3. *Thermal annealing,* $L_D \sim 150$ *nm.* After the SOL reduction thoroughly washed and dried np-Au was subjected to thermal treatment at 400 °C for 1 h in Ar flow.

All reduction treatments were performed in fresh 1 M $HClO_4$ solution prepared from high purity $HClO_4$ (70%, Suprapur, Merck). Subsequently, the np-Au samples were immersed in ultrapure water for at least 12 h and left for drying in Ar flow for more than two days.

3.4 Samples characterization

3.4.1 Scanning electron microscopy and X-ray energy-dispersive spectroscopy

The morphology and chemical composition of the samples after the dealloying and post-treatments were characterized by a high resolution scanning electron microscope Zeiss Supra 55VP FEG (SEM), equipped with an Oxford X-Max 20 SDD Energy Dispersive X-ray (EDX) detector. The advantage of SEM as the most suitable technique for the microstructural characterization of nanoporous metals lies in simplicity of samples preparation (compared with e.g. TEM) together with excellent imaging properties and analytical capabilities. The EDX point analysis technique was employed for the investigation of residual Ag present in the nanoporous samples after dealloying.

To preserve the original microstructure of the porous material, the samples for the SEM study were polarized at higher potential (1.46 V) for 30 min to form oxide layer which suppresses coarsening of the ligaments prior to SEM observation [15]. Thereafter, the samples were immediately rinsed with ultrapure water and left for air-drying.

The micrographs were taken at the accelerating voltage of 3-5 kV, using either secondary electron (SE) or in-lens detectors at typical working distances of 3-6 mm. EDX microanalysis was performed at the higher accelerating voltages (10-20 kV) and bigger working distances (7-10 mm).

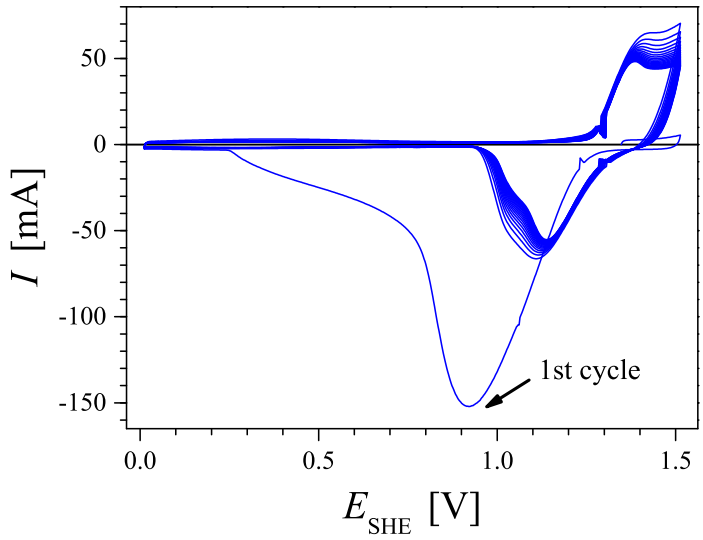

Figure 3.6. Typical CV recorded in 1 M HClO4 during chemical annealing of as-dealloyed np-Au (20 successive potential cycles). Last cycles are characterized by sharper peaks. The area under the adsorption/desorption peaks decreases from initial to subsequent CV cycles, implying increasing of the ligament size [70]. *Note.* The high values of the current is explained by using several samples with total mass of ≈ 35 mg in one experiment.

Average ligament diameter was evaluated from the SEM images by measuring more than 50 ligaments.

3.4.2 Surface area measurements by capacitance ratio method

Generally, surface area of an electrode, A, is referred either to its mass (*mass specific surface area*, α_m) or volume unit (*volume specific surface area*, α_v); both quantities are related by the following equation [158]:

$$\alpha_\mathrm{v} = \frac{A}{V} = \frac{A}{m}\rho = \alpha_\mathrm{m}\rho, \tag{3.6}$$

where V, m, and ρ denote respectively the volume, mass, and density of the solid system (or solid phase in case of a porous electrode).

In this work, the electrochemically active surface area of np-Au electrodes, A, was accessed by a *capacitance ratio method*. The method estimates A through the measurement of the apparent total capacitance C and comparing this value to a reference one C^*, which represents the capacitance (per area) of the corresponding planar surface [158]

$$A = \frac{C}{C^*} \tag{3.7}$$

Here, $C^* = 40\ \mu\mathrm{Fcm}^{-2}$, the capacitance of a smooth polycrystalline Au electrode in the unoxidized state [159] was taken for the area calculations in 1 M $HClO_4$ at potentials in the capacitive region I (Fig. 3.3b).

The pseudo-capacitance of np-Au network, C, was obtained either by EIS (Section 3.2.3) or CV measurements as introduced below.

CVs at different scan rates were recorded in the potential region, where the double layer charging is the only process taking place at a np-Au electrode (Fig. 3.7a). The current in the middle of that potential window I_m was then plotted as a function of the scan rate v (Fig. 3.7b). A linear fit of the plot I_m vs. v in Fig. 3.7b testifies to the condition of the double

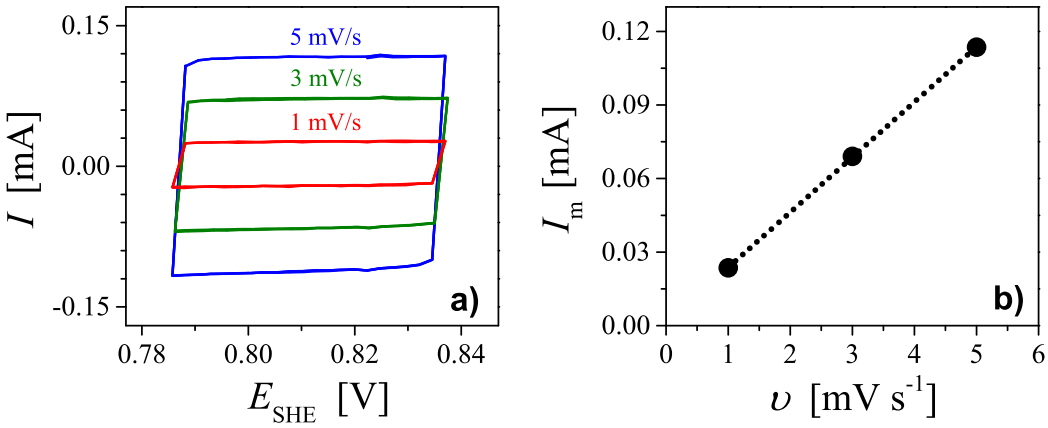

Figure 3.7. Double-layer capacitance of np-Au measured by cyclic voltammetry. (a) Typical CVs recorded at different scan rates v between 0.787 and 0.837 V in 1 M $HClO_4$. (b) Dependence of the average current I_m in the middle of CVs (0.812 V) as a function of scan rate v. The dotted line shows a linear fit to the data.

layer charging and the specific capacitance can be obtained as the slope:

$$C = \frac{dQ}{dE} = I_m \frac{dt}{dE} = I_m \left(\frac{dE}{dt}\right)^{-1} = \frac{I_m}{v}, \tag{3.8}$$

where Q is the total charge associated with the charging of the Au/electrolyte interface.

Both experimental techniques, EIS and CV, yielded essentially the same values of the capacitance, but EIS was preferred in most of the cases due to quicker measurements.

For a nanoporous structure with elongated ligaments of approximately circular cross-section, the volume specific surface area α_v gives a quantitative estimate of a ligament size L_D via two relationships

$$L_D = \frac{4}{\alpha_v} \tag{3.9}$$

$$L_D = \frac{1.63(1.25 - \varphi)(1.89 + \varphi(0.505 + \varphi))}{\alpha_v}, \tag{3.10}$$

where $\varphi = \rho_{np}/\rho$ the solid fraction of a nanoporous sample with the density ρ_{np}. Equation (3.9) follows from a simple consideration of a ligament as an ideal, infinitely long cylinder and using its surface area to volume ratio, A/V. It has been found to be reasonable for estimation a structure size of np-Au with a clean surface [157]. Equation (3.10) has been derived in [99] based on approximation of np-Au structure as a periodic array of diamond-type, tetragonal unit cells, consisting of idealized, cylindrical ligaments and spherical nodes where the ligaments meet [109]. In the work, both formulas have been adopted for a fast check of the characteristic structure size of np-Au samples just before mechanical testing.

3.4.3 Immersion method for estimation of the potential of zero charge

An important characteristic of an electrode/electrolyte interface is the potential of zero charge (pzc), which depends on the nature of anions presented in the electrolyte. To estimate the pzc for np-Au in the studied aqueous solutions (Tab. 3.1) an *immersion method* was applied due to its simplicity and applicability to many systems [160].

In the method, a clean and *dry* electrode which is connected to RE is rapidly immersed into an electrolyte solution at open-circuit conditions, when no charging current flows at the interface [161]. Upon immersion a transient potential is observed between the WE and RE that considered to be the pzc.

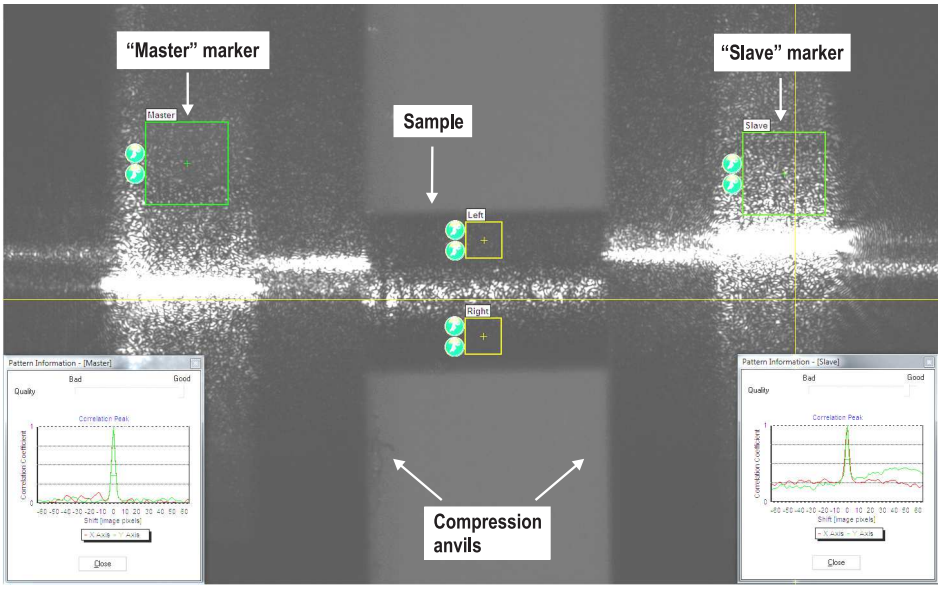

Figure 3.8. A typical speckle pattern of np-Au (inverted image). The displacement is recorded by a shift between markers "master" and "slave". Markers for monitoring the lateral displacements are also shown.

Np-Au electrodes for the pzc study were prepared as described in Section 3.3.3 using the reduction treatment followed by subsequent washing and drying in Ar gas atmosphere before immersion. The samples after the reduction here were preferred in order to avoid any films at the surface and to minimize the faradaic current. The potential of the electrode was monitored by a potentiostat with respect to pseudo Ag/AgCl RE.

3.4.4 Mechanical testing machine

Nanoporous metals normally fail in a brittle manner while tested in bending or tensile modes [93, 94] but have been reported to demonstrate appreciable ductility in compression [94]. The dealloying routes developed to fabricate crack-free millimeter-sized np-Au samples that can be deformed up to high compression strains [15] prompted to choose the compression mode for mechanical testing in this work.

Uniaxial compression tests were conducted using a universal mechanical testing machine, Zwick Z010 TN, with a calibrated load cell (0.5 kN) at constant engineering strain rate between 10^{-5} and 10^{-4} s^{-1} under ambient conditions. The machine is controlled by testXpert II software, supplemented by a graphical programming module which allows setting arbitrary load-displacement-time programs. Two different types of loading were implemented: continuous compression up to engineering strain of 0.6 – 0.7 and compression unload/reload cycles with an incremental increasing of a strain level during reloading.

A displacement was monitored in a longitudinal direction, using a laser speckle extensometer (Zwick laserXtens) focusing on the load surfaces. The laserXtens system enables non-contact strain measurements by generating a specific pattern of speckles from a specimen surface (Fig. 3.8). Selected measuring points of the surface structure (master and slave in Fig. 3.8) are constantly followed and its lateral movements, which are the basis of the speckle pattern, are continuously evaluated during specimen deformation. The displacement was then used for computing true strain as $e = -ln(1 - \Delta l/l_0)$, where l_0 is the input length of a sample and Δl is the recorded change in the displacement. Alternatively, the displacements registered by the crosshead position were used to calculate the strains in cases where the strain monitoring was not readily combined with the electrochemical setup. True stress was determined

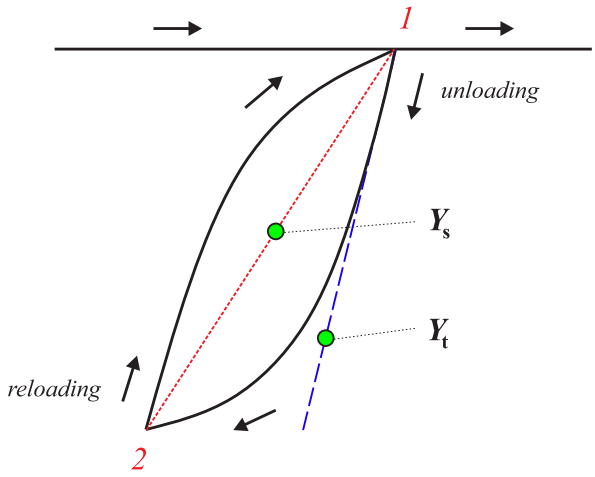

Figure 3.9. Determination of the Young's modulus from an unloading-reloading segment of a stress-strain diagram (schematic, after [163]). Straight lines correspond to secant modulus Y_s (red dotted line) and tangent modulus Y_t (blue dashed ine).

by dividing the applied load to the initial cross-sectional area of a specimen, since a negligible lateral expansion has been reported for np-Au up to high strains [94, 99].

The representative specimens which were straight and uniform in cross section were selected for the compression tests. The dimensions were ranged from 1.17–1.37 mm for diameter and 1.90 – 2.10 mm for length, so that the ratio of length to diameter was within 1.5 – 1.7 to avoid buckling or barreling.

Determination of elastic modulus from load-unload segments

Intermediate load/unload segments during continuously increasing deformation allowed evaluation of the effective (macroscopic) elastic modulus as function of prestrain [109]. The Young's modulus was identified as the slope of the chord drawn between a point of a maximum stress before unloading (point *1* in Fig. 3.9), and a point of a minimum stress, where the unloading and reloading curves intersect (point *2* in Fig. 3.9). In accordance with the ASTM E111 standard [162], this method of the modulus determination defines *chord* or *secant modulus* Y_s. A corresponding amount of the residual strain upon each unloading, e, was obtained by extrapolation of the chord to zero stress. This strain was then converted to the relative density (or solid volume fraction) of np-structure φ via

$$\varphi = \varphi_0 \exp(e), \tag{3.11}$$

where φ_0, the initial relative density of the material in the as-prepared *sufficiently dry* state was determined based on its dimensions, mass, and the density of gold. The relationship (3.11) was derived assuming constant cross section area of np-Au samples in compression, in line with observations in [94].

3.4.5 Dynamic mechanical analysis

Dynamic mechanical analysis (DMA) in compression mode was carried out for quantifying Y^{eff} in a dry state and its changes in response to electrode potential variations (Section 3.5.1).

A DMA 242C (Netzsch) was used at the first stage of the work. Later STARe System DMA/SDTA861e (Mettler Toledo) was employed due to broader range of applied forces. A sample was subjected to a mechanical oscillation predefined by a frequency (ν) and either dynamic force amplitude (F_{dyn}) or displacement amplitude (a_{dyn}). Applying a static force

F_{st} in addition to F_{dyn} was necessary to hold the sample in place during the entire deformation cycle; F_{st} exceeded F_{dyn} by 10% and this ratio ($F_{st}/F_{dyn} = 1.1$) was kept constant.

The raw data, the measured force and displacement amplitudes, F_{dyn} and a_{dyn}, and their phase shifts, δ, were used to calculate the viscoelastic properties of the material:

- complex modulus
$$Y^* = \left(\frac{\sigma_{dyn}}{\varepsilon_{dyn}}\right)\cos\delta + i\left(\frac{\sigma_{dyn}}{\epsilon_{dyn}}\right)\sin\delta \tag{3.12}$$
- storage modulus (the elastic component related to the sample stiffness)
$$Y' = \left(\frac{\sigma_{dyn}}{\varepsilon_{dyn}}\right)\cos\delta, \tag{3.13}$$
- loss modulus (the viscous component related to the sample ability to dissipate mechanical energy)
$$Y'' = \left(\frac{\sigma_{dyn}}{\varepsilon_{dyn}}\right)\sin\delta, \tag{3.14}$$
- mechanical damping factor (a measure of the amount of deformation energy that is dissipated as heat during each cycle)
$$\tan\delta = \frac{Y''}{Y'}. \tag{3.15}$$

Here, $\sigma_{dyn}/\varepsilon_{dyn} = (F_{dyn}/a_{dyn})(l_0/A_s)$ is the ratio of peak stress to peak strain, l_0 is the sample initial length, and A_s is the cross section area. Additionally, the length change of the sample, Δl, was recorded, which represents a variation of the mean sample length, averaged over each of the fast load cycles (static deflection).

The DMA measurements were performed mainly at constant displacement amplitude with the average peak-to-peak value of $\leq 1.3\%$, static stresses ≤ 4 MPa, and constant frequency of 1 Hz. To determine the frequency dependence of the moduli upon charging in electrolytes, the sequential frequency series were applied.

Prior to DMA, samples were predeformed to a true strain in the range of $0.065 - 0.09$ to provide coplanar loading surfaces and to suppress plastic deformation under DMA cyles.

All experiments were conducted at room temperature (isothermal DMA mode).

3.5 *In situ* measurement setups

3.5.1 Electrochemical setup combined with DMA

To study the influence of electric potentials on the viscoelastic characteristics in electrolytic medium, the DMA compression sample holder was equipped with a custom built *in situ* electrochemical cell (a capacity of ≈ 1.4 ml) and fused silica pushrod (Fig. 3.10). The cell represented itself the standard three-electrode arrangement (Section 3.1.1), where np-Au formed WE. The CE was provided by Pt wire wrapped with porous carbon cloth, and Ag/AgCl wire served as RE. In the experiments containing halide ions, commercial Ag/AgCl REs inserted in a chemically inert tube housing with low leakage (Dri-Ref, World Precision Instruments) were used to avoid contamination of Ag/AgCl with chloride or bromide. The potential was controlled via a potentiostat (PGSTAT 302N, Metrohm) attached to the electrodes via thin Au wires. An electrical contact with the sample was realized through sputtered Au coating on the DMA probe. This thin film was found to have no effect on the stiffness of the setup. Any metal surfaces of the instrument were isolated from contacting with the Au wires and electrodes. Prior to a DMA experiment a test CV was recorded in the *in situ* cell to ensure proper wetting and to check cleanness of a sample and electrolyte under study.

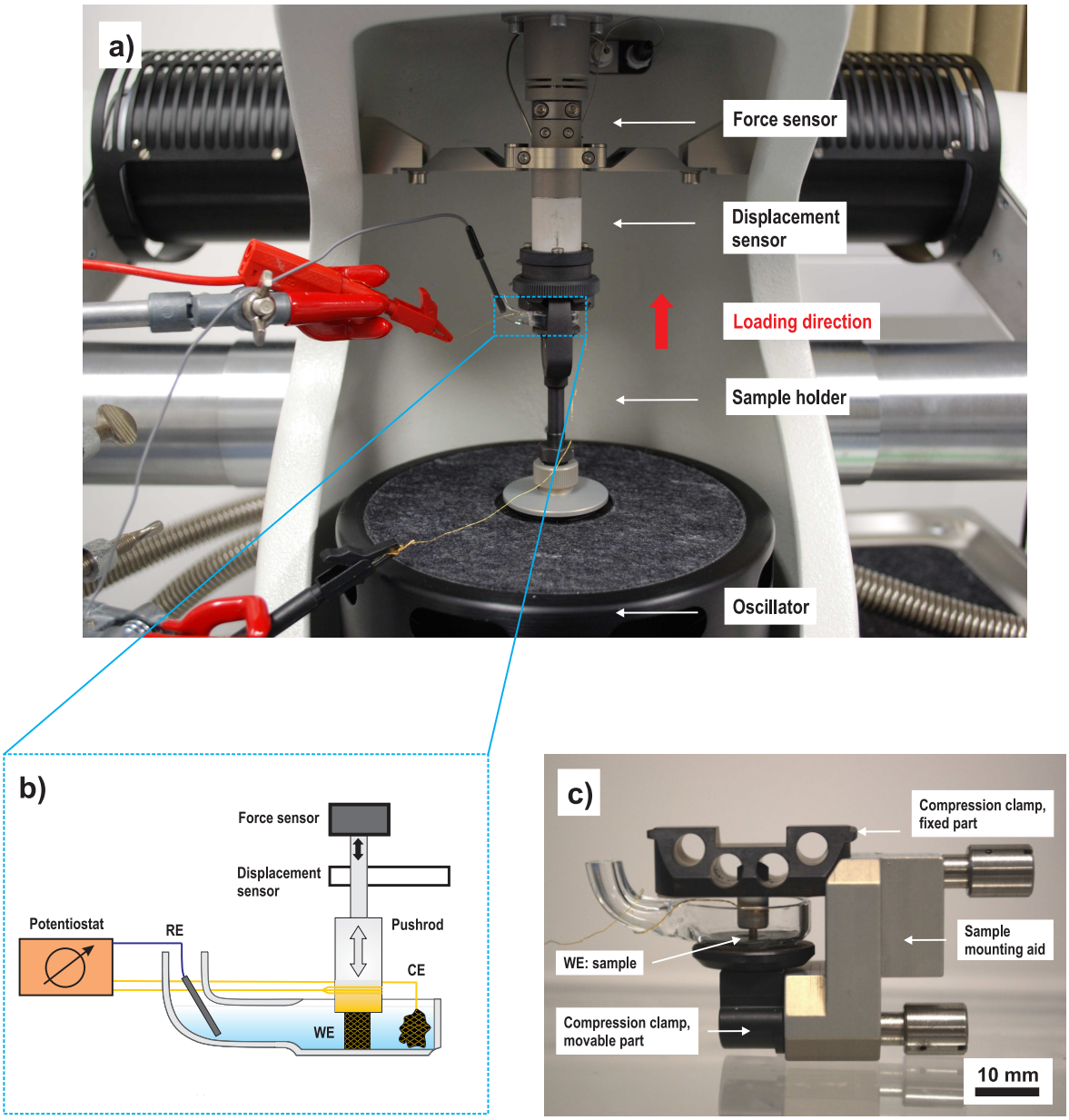

Figure 3.10. *In situ* DMA setup: (a) DMA testing apparatus (STARe System DMA/SDTA861e, Mettler Toledo) with built-in electrochemical cell for *in situ* compression measurements, (b) a schematic of the cell equipped with three electrodes: np-Au specimen (WE), counter electrode (CE), and Ag/AgCl reference electrode (RE), (c) a photograph of the electrochemical DMA cell with a specimen. The cell is filled in with an electrolyte via a side arm, which serves as an compartment for RE.

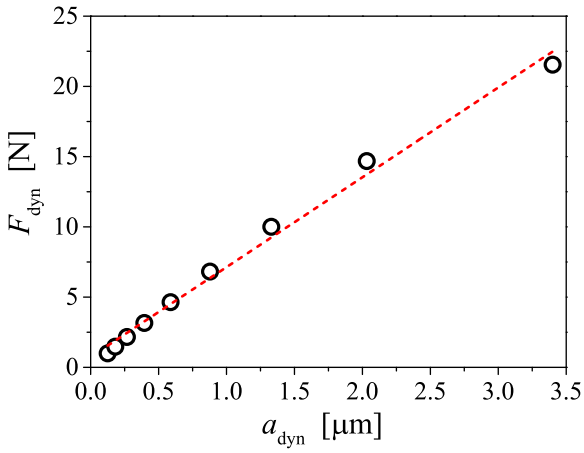

Figure 3.11. Determination of the stiffness of the customized DMA compression sample holder. Dynamic force amplitude F_{dyn} vs. displacement amplitude a_{dyn} measured at constant static force of 25 N. The red dashed line shows a linear fit of the data whose slope defines the stiffness.

Stiffness correction

The stiffness of standard DMA compression sample holder was determined during the mechanical adjustment of the instrument and was typically of ~ 2 MN/m. Since the holder was modified by attaching the quartz pushrod and electrochemical cell to the compression metal plates, a new stiffness was measured experimentally. A steel plate for calibration was placed under the probe tip and the cell. The maximum static force (25 N) was applied, while the dynamic force was logarithmically enlarged between 1 and 21.5 N with 6 points per decade. The resulting displacement amplitude a_{dyn} was plotted vs. the measured dynamic force amplitude F_{dyn} as shown in Fig. 3.11. The actual stiffness was then evaluated as a slope to the linear fit of these data. The method gave a constant stiffness of 6.04 ± 0.58 MN/m, which is higher than the manufacturer's nominal value.

3.5.2 Electrochemical setup combined with mechanical testing machine

The compression tests were performed *in situ* with samples immersed in electrolyte and under potentiostatic control. A glass cuvette (22.5 ml, Hellma) served a three-electrode electrochemical cell while the load was applied via a glass pushrod. The electrodes were the same as those used during *in situ* DMA experiments described above, except that for electrical contact a np-Au sample was placed on a thick platinum or gold plate (strengthened by rolling). A photograph of the setup is shown in Fig. 3.12. An experimental procedure to evaluate changes in the flow stress during variation of the electrode potential is outline below.

Upon continuous loading and after reaching an appreciable level of a plastic strain (~ 0.2 of engineering strain), a np-Au sample was subsequently subjected to a step-wise varied potential (the CA technique, Section 3.2.1) as illustrated in Fig. 3.13. The series of potential steps of increasing magnitude was applied from lower to upper potential vertex in anodic direction, in accordance with a CV recorded in the *in situ* setup just before the mechanical testing. A strain rate was held constant, between 10^{-5} and 10^{-4} s^{-1}, and the strain was determined either from the anvil displacement or via the laser extensometer.

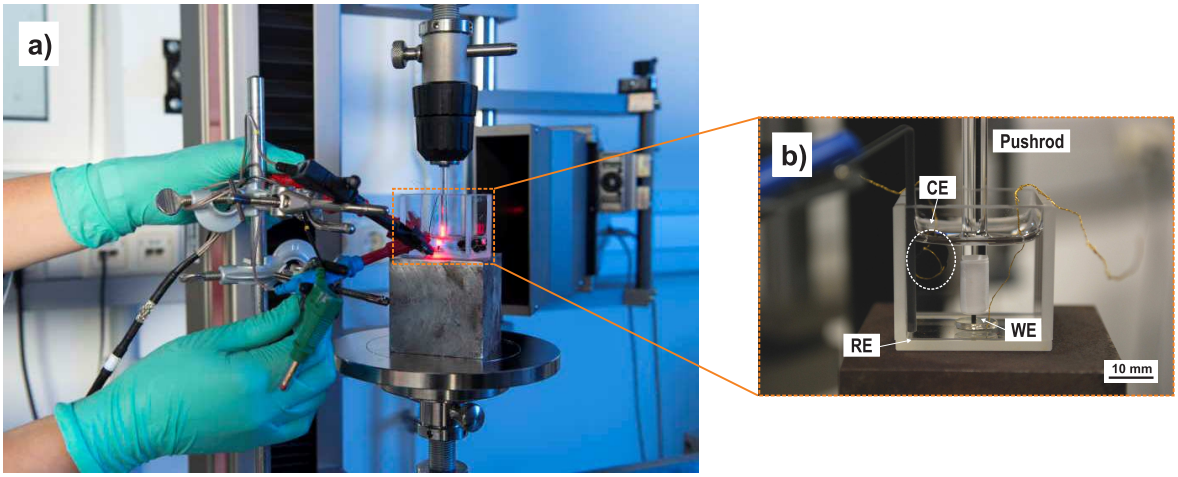

Figure 3.12. *In situ* setup for compression tests under potential control in the mechanical testing machine: (a) connection of the three-electrode electrochemical cell built in the testing device Zwick Z010 TN to potentiostat (a photograph ©SFB986), a sample is illuminated by laser light, (b) designation of the electrodes in the cell: np-Au specimen (WE), counter electrode (CE), and Ag/AgCl reference electrode.

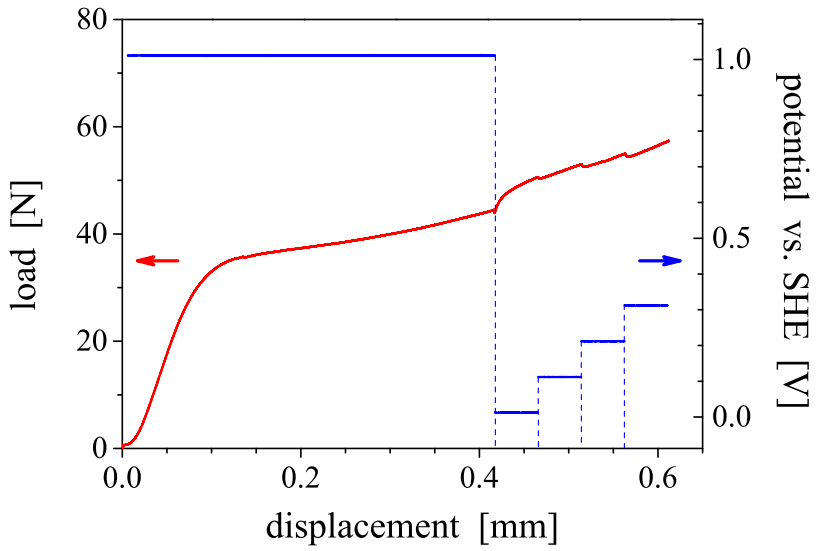

Figure 3.13. A part of a typical load-displacement diagram (red) recorded in *in situ* setup for compression tests. A sequence of the applied potential steps (blue) during plastic deformation is superimposed.

3.5.3 *In situ* dilatometry for assessment of surface stress and surface tension

In situ dilatometry technique [11, 70] was used to estimate an *apparent variation in surface stress*, f, with electrode potential, E. In the method, the dimension changes of a macroscopic nanoporous material during potential cycling in an electrolyte are detected by dilatometer. The potential-induced strain $\delta\varepsilon$ is attributed to the action of the surface stress, whose changes with potential lead to expansion or contraction of the macroscopic sample [164]. The variation in the mean surface stress relative to an arbitrary reference state, δf, can be determined from the changes in the macroscopic strain, $\delta\varepsilon$, via [164]

$$\delta f = -\frac{9K}{2\alpha_{\mathrm{m}}\rho}\delta\varepsilon, \tag{3.16}$$

where K is the bulk modulus and ρ the density of the solid phase, respectively, and α_{m} denotes the mass specific surface area.

Equation (3.16) has been derived and verified for porous materials consisting of monodisperse spherical particles, where the deformation induced by the surface stress is assumed to be isotropic [11, 70]. For np-Au material fabricated by alloy corrosion its structural constituents are elongated so that the local strains are generally anisotropic. Nonetheless, as has been shown in [70] the relationship (3.16) can be used for assessment of the *qualitative* changes of the apparent surface stress of np-Au.

In this study, the length change of np-Au during cycling voltammetry (Section 3.2.2) was recorded in the electrochemical cell (see Fig. 3.1) that was placed in a vertical dilatometer (L75, Linseis). The reference and counter electrodes were analogues to those employed for *in situ* experiments in the DMA or compression testing machine and 1 M $HClO_4$ was used as the electrolyte. The sample was fixed by maintaining a stress of 0.14 MPa throughout the experiment. The strain, $\delta\varepsilon$, was determined as the length change, Δl, normalized to the input sample length, l_0, $\delta\varepsilon = \Delta l/l_0$.

The surface tension variation with the electrode potential $\delta\gamma$ was computed from the cyclic voltammetry data using Lippmann Eq. (2.17).

Chapter 4

Results

4.1 Microstructure and specific surface area

As it has been introduced in Section 3.3.2, np-Au samples can be synthesized free of cracks and with initial ligament thickness of ~ 15 nm. Figure 4.1a and 4.2a confirm this, illustrating scanning electron micrographs (SEM) of a typical interior of a sample dealloyed from $Au_{25}Ag_{75}$ and its structure size, respectively. A smooth morphology of the fracture surface indicates that no native cracks were formed during dealloying.

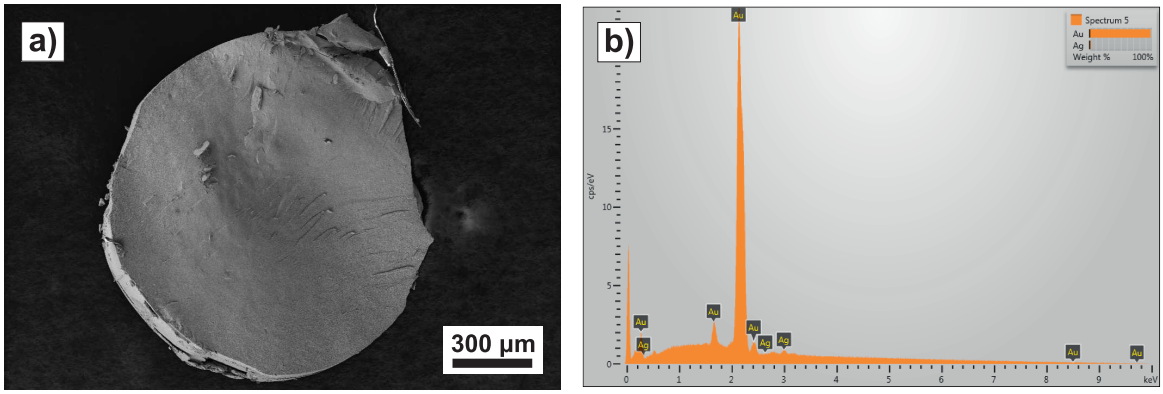

Figure 4.1. Fracture surface and compositional characterization of np-Au prepared by electrochemical dealloying $Au_{25}Ag_{75}$ in 1 M $HClO_4$ at 1.26 V vs. SHE. (a) Scanning electron micrograph (SEM) of a typical fracture surface. (b) Corresponding energy dispersive X-ray spectroscopy spectrum (EDS spectrum) generated from a scan area of ~ 390×475 μm in the center of the specimen. The spectrum resolves the presence of Au and Ag with ~ 96 and 4 at.%, respectively.

Systematic energy-dispersive x-ray spectroscopy (EDS) study in SEM reveals that a relatively high amount of residual Ag remains after dealloying, which can reach ~ 15 at.%. The residual Ag content in the as-dealloyed samples is however significantly reduced after the repeated CV cycles of an electrode potential or *electrochemical annealing* (Section 3.3.3) as presented in Tab. 4.1. Such reduction treatment causes coarsening of the nanoporous structure, so that Ag ions can be released from the bulk of the ligaments into the electrolyte used for the potential cycling [147].

Along with thermal annealing the post-dealloying electrochemical annealing also allows further control of the initial as-dealloyed nanoporous structure. Figure 4.2 illustrates the resulting morphology of the samples employed in the present study for mechanical testing. The corresponding data on the ligament size and residual Ag content after the posttreatments are provided in Tab. 4.1. The SEM EDS data demonstrate that up to ~ 6 at.% can be left in the Au ligaments of the samples after surface oxide layer (SOL) reduction treatment

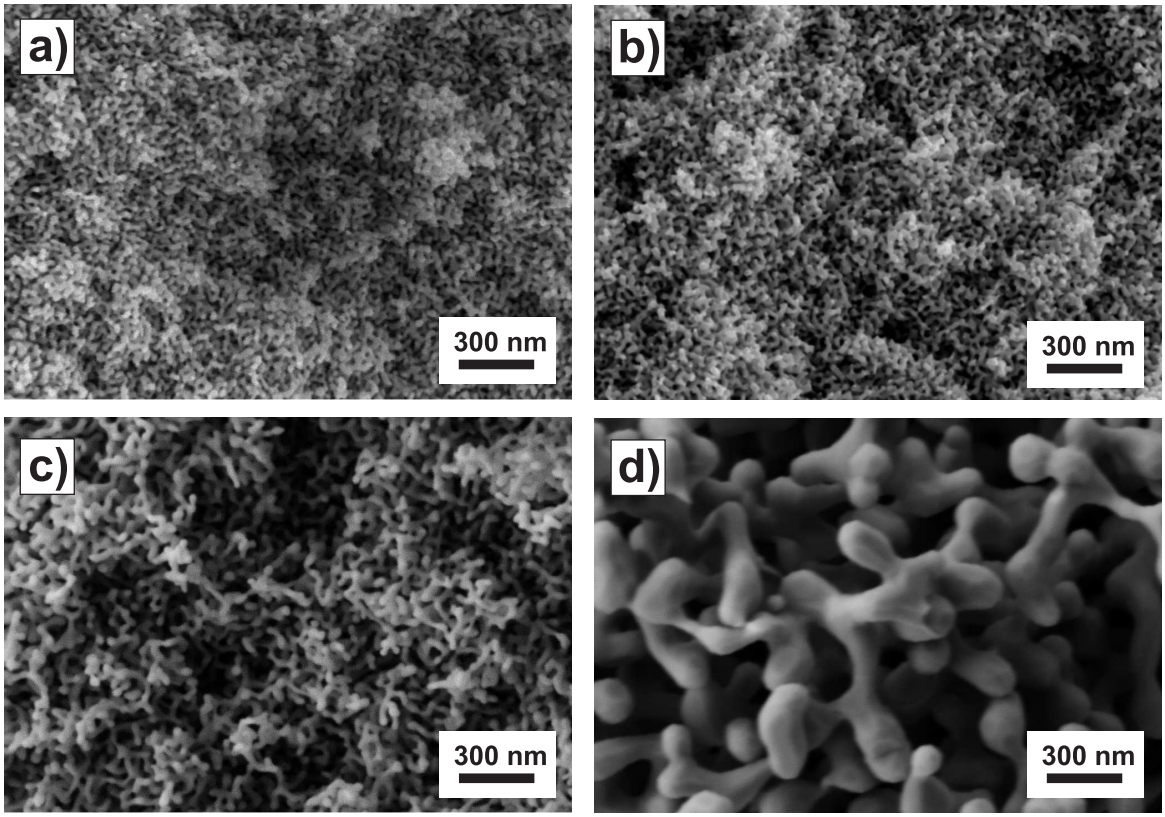

Figure 4.2. SEM images of microstructure (fracture surfaces) of np-Au after dealloying, electrochemical, and thermal annealing. (a) As-dealloyed, (b) after surface oxide layer (SOL) reduction, (c) after chemical annealing in 1 M $HClO_4$ for 15 potential cycles in the interval 0.01 to 1.51 V (reduction), (d) after SOL reduction and subsequent thermal annealing at T = 400°C for 1 h. Three classes of samples (b, c, d) were used for mechanical testing.

(Section 3.3.3) and Ag is almost completely dissolved after the reduction in a broader potential range. Qualitatively the morphological features on the SEM images remain practically invariant while solid fraction increases (Tab. 4.1).

Table 4.1. A summary of samples parameters of np-Au synthesized by electrochemical dealloying and modified by post-dealloying processing. φ – solid fraction, α_m – mass specific surface area, L_D – mean ligament diameter.

Sample state	Residual Ag [at.%]	φ [-]	α_m [g/mm^2]	L_D [nm]	
				SEM	capacitance ratio method[1]
as-dealloyed	15.68 ± 0.20	0.277 ± 0.016	7.21 ± 0.35	15 ± 5	24.8 ± 2.0
SOL reduction	3.13 ± 2.52	0.273 ± 0.013	6.05 ± 1.80	20 ± 5	29.8 ± 7.1
reduction	0.47 ± 0.23	0.293 ± 0.017	3.83 ± 0.40	40 ± 5	45.7 ± 4.5
SOL red + 1 h@400°C	7.27 ± 2.13	0.315 ± 0.025	1.03 ± 0.58	150 ± 5	167.5 ± 2.6

Although there is some evidence on anisotropy of the interfacial morphology during thermal coarsening of np-Au [165], many studies confirm the approaching of np-Au structure to the self-similarity [66, 147, 166]. Hence, the coarsening of the np-structure by potential in acid or thermal annealing enables direct tuning of the morphology of the material, providing a meaningful way of analyzing the size-dependent mechanical properties.

[1]The values obtained using Eq. (3.10).

Additionally, the specific surface area of the samples was quantified by the capacitance method, using both CV and EIS techniques, following the procedures outlined in Chapter 3. Based on these data the ligament sizes were estimated and compared to the analogous values determined by the SEM study. Overall, there is a good agreement between two data sets is observed. At the same time it is found that Eq. (3.10) provides a better correlation with the SEM values as compared to Eq. (3.9) (Section 3.4.2).

4.2 Mechanical behavior under compression in air

Prior to studying the mechanical properties in an electrolytic medium, a stress-strain behavior of dry samples in compression was inspected in air. Figure 4.3 presents the stress–true strain

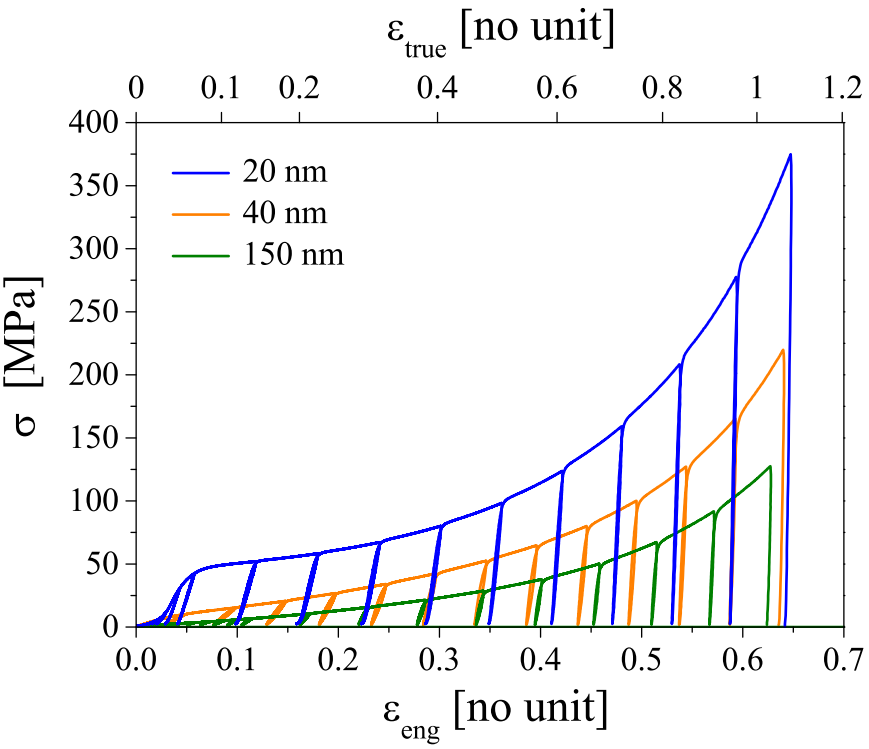

Figure 4.3. Compression behavior of np-Au in air: load-unload stress-strain curves at an engineering strain rate of 10^{-4} s^{-1}. Sample with L_D = 20 nm shows higher stresses and less pronounced yielding than those with coarser structural size (> 40 nm), despite the early plasticity in the initial portion of the curve, which is likely attributed to contact issue at the beginning of the loading. ε_{eng} and ε_{true} denote respectively engineering and true srain; σ is compressive macroscopic stress.

response of the representative specimens with different ligament diameter ($L_D = 20 \pm 5, 40 \pm 5, 150 \pm 5$ nm). The initial portion of the compression curve for L_D = 20 nm reveals an early yielding, most likely due to nonplanarity of the loading surfaces of the sample or contact problem with the compression grips. Since the subsequent loading stages are characterized by a near-linear elastic regime, it would be possible to identify a yield stress in the absence of such effects. The curves at $L_D > 40$ nm exhibit the *immediate plasticity* even at the lowest strain, with no distinguishable yield point.

The early plasticity is further followed by a noticeable strain hardening at larger strains. Comparing stress values at strains ε_{eng} = 0.1 and 0.6 for instance for L_D = 20 nm, it can be seen that the flow stress increases greatly from 50 to 284 MPa. Note also the *excellent ductility* of np-Au samples regardless of the ligament size.

These observations fully agree with previous reports on the stress-strain behavior of macroscopic np-Au samples of similar ligament diameter in compression [15, 94, 167]. However, the data here provide an extension of the earlier studies, presenting multiple loading and unloading cycles during the continuously increasing deformation, allowing identification of an elastic component of the deformation in a single experiment [109].

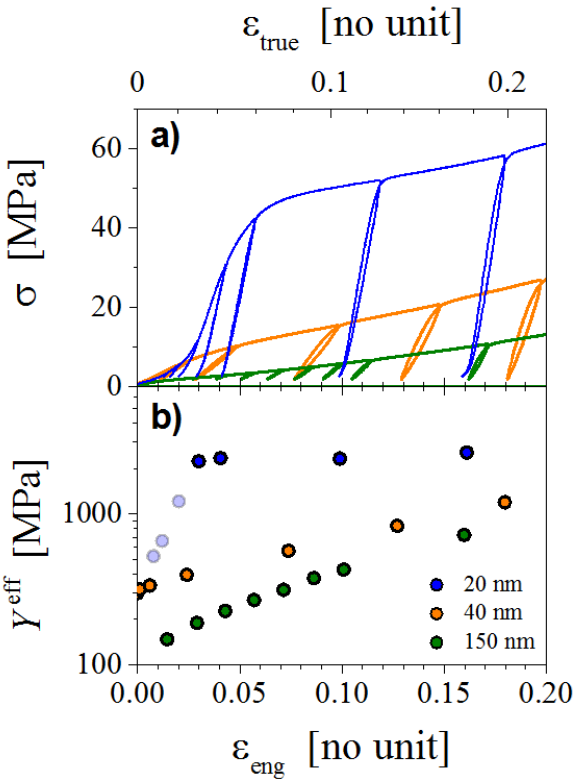

Figure 4.4. Load-unload cycles and the corresponding elastic moduli (secant values): (a) magnified load-unload stress-strain curves up to 20% of deformation. (b) evolution of effective Young's modulus, Y^{eff}, determined from the load/unload segments, as a function of strain. The moduli values determined during first three unloading steps for L_{D} = 20 nm (light blue circles) should be viewed with caution because of the uncertainties at the beginning of the loading.

The load/unload sequence during continuous loading gives the advantage to explore a deviation from the nonlinear deformation at very small loads in detail as well as an evolution of the stiffness under compressive strain. Figure 4.4 magnifies the load-unload stress-strain curves at strains up to 20% and shows the corresponding secant modulus values. Residual strain after unloading even for the finer ligament structure (~ 20 nm) appears already at a small stress (3 MPa), indicating a deviation from the linearity.

Note the extremely low elastic moduli of np-Au at the beginning. The initial values for all three samples in Fig. 4.4b are lower compared to the previously reported values for nanoindentation, film bending, and micro-tensile or compression tests [87, 93, 102, 168]. The unload/load segments implemented during macroscopic compression testing revealed the pronounced stiffening of np-Au as the plastic deformation proceeds, which has been pointed out also in Ref. [109]. As a consequence of the negligible lateral expansion in compression [99], the material densifies and the elastic modulus gradually goes up. This is well illustrated for the sample with L_{D} = 150 nm, whose stiffness increases more than 5-fold after nearly 20% of engineering strain. Besides that the moduli are very low for all samples tested regardless of the ligament size. Referring to the latest literature reports on the effective elastic properties of np-Au, the high compliance of the material in compression is observed for the first time.

In the view of the Gibson-Ashby scaling law for elasticity (1.2), the enhanced stiffness is expected for foam materials with higher relative densities. Yet, the sample with the coarsest ligament structure in Fig. 4.3 and apparently larger initial solid fraction (Tab. 4.1) is characterized by the lowest values of Y^{eff}. This finding, while preliminary, suggests that a ligament size (or specific surface area) and not a solid fraction dominates the elastic behavior of np-Au. Accurate density measurements of nanoporous specimens would facilitate studying the nature and extent of this effect.

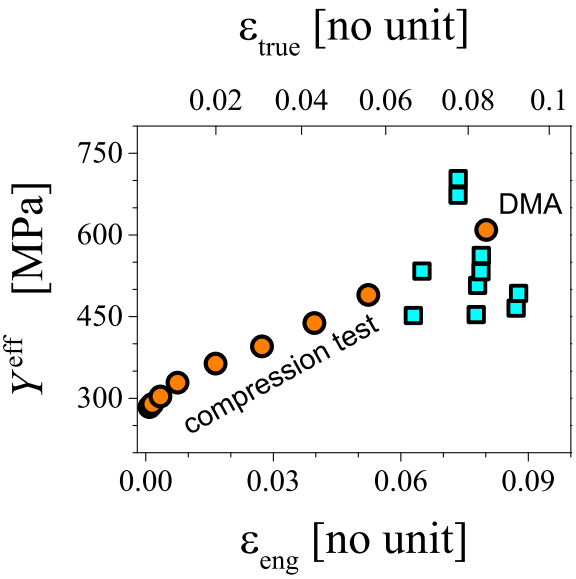

Figure 4.5. Comparison of the effective elastic moduli for np-Au with L_{D} = 40 nm: secant values of Y^{eff} from the load-unload segments (circles) and Y^{eff} measured as the storage modulus in the dynamic mechanical analyzer (DMA), using prestrained samples (squares). Compliance similar to polymers; DMA is valid probe of stiffness [169].

Since the nanoporous samples exhibit the large compliance, their behavior is similar to that of polymers, and thus dynamical mechanical analysis (DMA) is well suited for quantifying their elastic response. Figure 4.5 compares the effective macroscopic stiffness as obtained by DMA on separate specimens predeformed to 6 – 9% engineering strain with the results from the unload/load cycles during the conventional compression test. The consistency of two data sets for Y^{eff} supports the validity of the DMA measurements.

Below a study of the *relative changes* of Y^{eff} in response to different surface states is presented. These changes can be accurately and reliably detected, irrespective of uncertainty in the absolute values that may be induced due to imperfect contact with the load probes.

4.3 Elastic behavior in aqueous electrolytes

4.3.1 Elastic modulus-electrode potential response in $HClO_4$

Dynamic mechanical analysis during potential cycles

The DMA experiment worked with the pore space of the np-Au with L_{D} = 40 nm wetted by 1 M $HClO_4$ as a weakly adsorbing aqueous electrolyte. The infiltrated metal network was wired as the working electrode (WE) and a state of the interface formed between the metal and electrolyte was controlled by a potentiostat. This *in situ* environmental control enabled examination of variations in the elasticity of np-Au as a function of the conditions on the pore surfaces. In this respect, a design of the experiment is similar to that for *in situ* dilatometry,

where the actuation properties of np-Au were studied upon electrochemical cycling [70]. The oscillating mechanical loading in DMA was carried out with a frequency of 1 Hz, whereas the corresponding frequency of the electric cycles of the applied potential was < 1 mHz, being three orders of magnitude slower. In this way, each mechanical cycle was accomplished at constant value of the electrode potential.

Figure 4.6 summarizes results of the DMA *in situ* experiment. Part a) shows a cyclic voltammogram (CV), a dependance of the current on electrode potential at the WE, applied at scan rate of 2 mV/s. The CV well reproduces all features relevant to the behavior of gold in acidic solutions, displaying oxygen species electrosorption peaks at the positive end and a broad capacitive region at lesser E (Section 3.2.2). At the surface of Au, as it has been established from electrochemical studies [140], the electrosorption under the present conditions is constituted by the deposition of 1 atomic monolayer of OH species (a peak potential at $\approx$ +1.3 V). Subsequently, at the potential beyond 1.3 V, this process is followed by desorption of the hydrogen. A remaining peak during the negative-going assigns the reversible reduction of the deposited adsorbate layer. The experiment was started at +0.940 V, a value of the open circuit potential (OCP) of as-prepared samples that corresponds to a state of a clean surface. This confirms removal of all superficial oxide by the reduction treatment (Section 3.3.3). The potential of zero charge (pzc) for Au in perchloric acid aqueous solutions is reported to be +0.470 V on the potential scale here [170], so that the polarization of the Au-electrolyte interface in the capacitive region covered both the positive and negative surface charge.

Figure 4.6b presents various mechanical characteristics measured by DMA simultaneously with the cyclic voltammograms. The static length change, Δl, describes a variation of the mean sample length based on the continuous measurements of the pushrod's position that are averaged over each of the fast load cycles. It can be seen that Δl exhibits cyclic changes, being a monotone function of the potential. Such behavior, as well as the peak-to-peak amplitude of $0.063\% \pm 0.004\%$, are in agreement with previous studies of the potential-induced strain of np-Au [70, 171]. The cyclic strain of the charged electrode is an indication of the surface stress variation, where the electrode expansion with increasing potential agrees with a negative value of the electrocapillary coupling parameter ς for Au surfaces in the inspected interval of the potentials [9] (Section 2.3.2). Taking into account the experimental evidence for the higher order bulk elasticity impact in nanowires at strains of several % [30], it is important that the surface-induced strain amplitude is rather small here. Thus, one may ignore any influence of Δl on the bulk elastic constants in the present experiments.

The most striking result to emerge from the data in Fig. 4.6b is that the effective storage (Y') and loss moduli (Y'') also display a large cyclic variation. The storage modulus, Y', strongly increases upon oxygen electrosorption, near the positive potential vertex. Simultaneously, the loss modulus, Y'', decreases to less than half the value, which corresponds to a condition of the clean surface. At the negative potential vertex, Y' exhibits a second maximum, whereas no significant feature is resolved in Y''. Together the findings imply that two different processes at the surface – oxygen electrosorption and negative charging in the capacitive regime – enhance the stiffness. It should be noted that contrary to the monotonous potential-dependence of the length change, the behavior of both moduli appears to be qualitatively different. The loss modulus stays much smaller as compared to the storage modulus, pointing out a nearly ideal elastic response of np-Au.

Apart cyclic changes Y' shows a slow upward drift to the higher values. This stiffening is accompanied by an irreversible densification of the sample with a total shrinkage $\Delta l \sim -4$ μm or -0.2% of the initial length after the 7 cycles. The shrinkage is typically observed in np-Au during potential cycling and may originate from slow plastic deformation under the action of the surface stress [76]. In view of invariant cyclic variations of Δl, Y', and Y'', the influence of the densification on the material's behavior can be neglected.

Figure 4.7 explores another set of *in situ* DMA experiments with focus on two separate

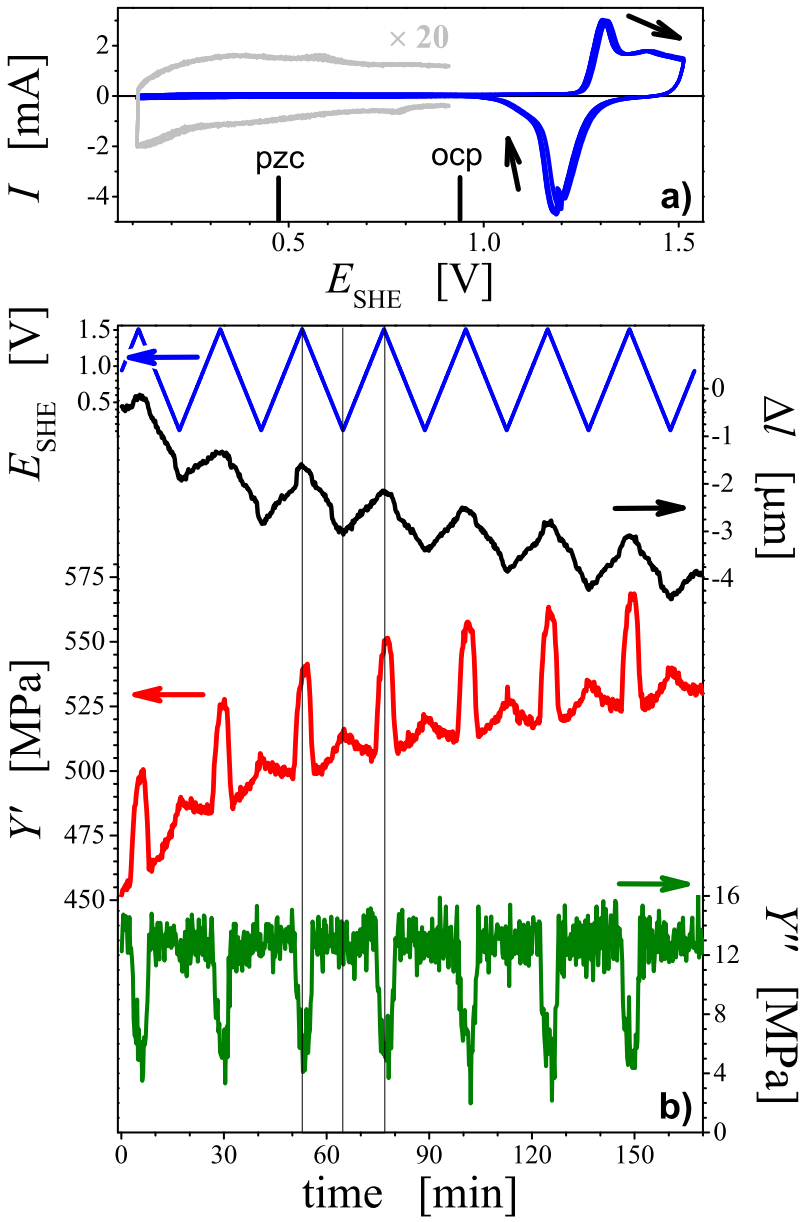

Figure 4.6. Results of dynamic mechanical analysis for np-Au with L_D = 40 nm measured *in situ* during 7 successive cyclic scans of the electrode potential E between 0.1 and +1.5 V, using 1 M $HClO_4$ as the electrolyte [169]. (a) Electrochemical characterization, represented by cyclic voltammograms (CVs) of current I versus electrode potential E at scan rate 2 mV/s, with scan direction indicated by arrows. Potential of zero charge (pzc) and open circuit potential (ocp) are also indicated. Grey line: magnification of current in capacitive regime. (b) Mechanical characterization recorded simultaneously with the CVs, with variation of E with time indicated by blue line and upper left ordinate: length change (black, upper right ordinate), storage modulus Y' (red, lower left ordinate), and loss modulus Y'' (green, lower right ordinate). Vertical lines mark vertex points of CV for one exemplary cycle. The DMA experiment was performed at a peak strain amplitude ε_{dyn} = 0.38% and a static effective macroscopic stress σ_{st} = 1.9 MPa.

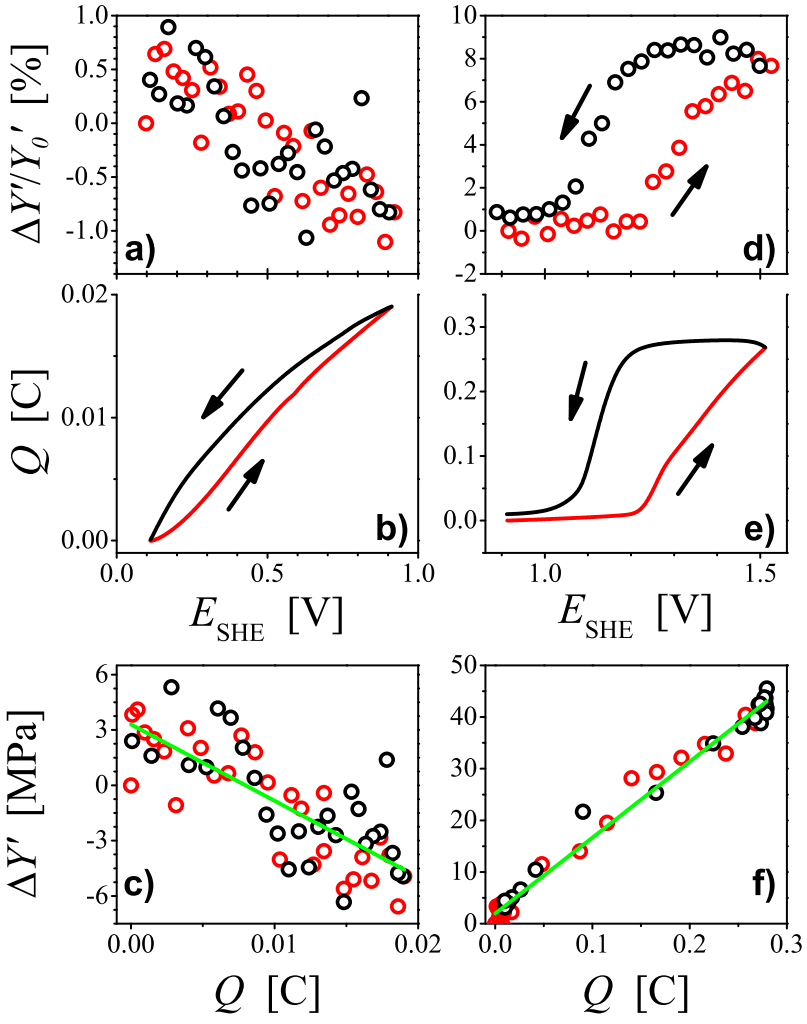

Figure 4.7. Relative variation of the storage modulus $\Delta Y'/Y_0^{'}$ of np-Au electrode with L_{D} = 40 nm at two distinguishable surface states [169]: (a) $\Delta Y'/Y_0^{'}$ vs. E in capacitive double-layer regime and (b) charge associated with charging and discharging processes of electrical double layer. (d) $\Delta Y'/Y_0^{'}$ vs. E in adsorption-desorption region and (e) corresponding charge transfer attributed to the oxidation and reduction reactions. (c) and (f) $\Delta Y'$ as a function of charge Q for both states. $\Delta Y' = f(Q)$ exhibits a reasonably linear behavior with slopes -413.62 ± 43.41 MPa/C and 147.08 ± 2.99 MPa/C. Electrolyte is 1 M $HClO_4$, scan rate is 2 mV/s. Arrows indicate the direction of scan.

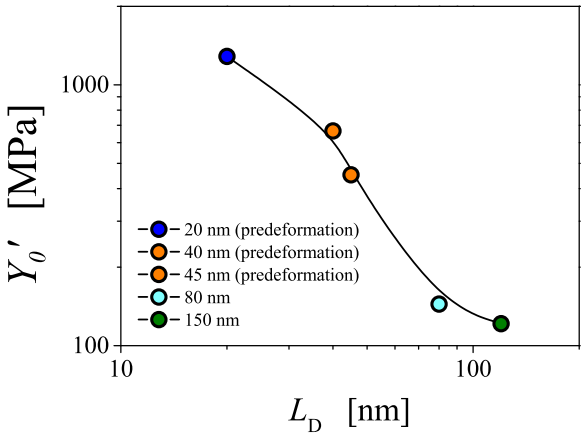

Figure 4.8. The initial values of the storage modulus, Y_0', measured in DMA during potential cycling in 1 M $HClO_4$ for samples with different ligament sizes, L_D, including predeformed and not predeformed ones. The results are in agreement with the data evaluated from the load/unload segments in Fig. 4.4b.

potential intervals from Fig. 4.6, i.e. oxygen species adsorbtion/desorption (E = 0.9...1.5 V) and capacitive polarization (E = 0.1...0.9 V). As can be seen from Fig. 4.7d, a depositon of OH-monolayer on the ligament surface causes increasing of Y', in direct proportion to the electrode charge, Q, as presented in Fig. 4.7e. While scanning back in cathodic direction, the adsorbate layer remains in place and Y' stays constant. Upon reaching the oxygen desorption peak, the stiffness reverts to its initial, lower value. A plot of Y' versus Q displayed in Fig. 4.7f for both scan directions indicates a linear and hysteresis-free relation. Such behavior has been observed in five separate samples from different batches prepared at identical conditions and highly consistent results have been found, with the relative change in storage modulus of $7.8 \pm 0.9\%$.

Part a) of Fig. 4.7 inspects the second potential window of the double layer charging region. Here, a linear dependence of the storage modulus on potential (Fig. 4.7a) and charge (Fig. 4.7b and 4c) has been revealed as well. In contrast to oxygen electrosorption, the slope during capacitive charging is of inverse sign, indicating stiffening of the material by negative charge or surface excess of electrons. The overall changes in Y' as verified independently with five samples attain $1.6 \pm 0.1\%$ in this regime.

4.3.2 Impact of ligament size

One way to improve stiffening during potential cycling would be an increase of the active specific surface area by employing nanoporous materials with pore size below the presented above 40 nm, and as a result to accommodate more surface charge into the pore surfaces. Moreover, inspecting the elastic response as the surface state is cyclically varied for different ligament diameters would provide more insight into the size-dependence of the Young's modulus, which is apparent from Fig. 4.4b. A similar trend of increasing the storage modulus of np-Au with smaller ligaments was also detected by DMA during *in situ* experiments in electrolytes, before an electrode potential was applied (Fig. 4.8). Both, prestrained and nonprestrained samples exhibit the stiffness values that reproduce the secant moduli from Fig. 4.4b with a good coincidence in the order of magnitude. The *in situ* DMA setup offers therefore a possibility to study a correlation between the elasticity of nanoporous metals and a ligament diameter or specific surface area.

Figure 4.9 compares the absolute and relative changes in the electrochemically modulated storage modulus Y' due to electrical polarization and adsorbate coverage as a function of

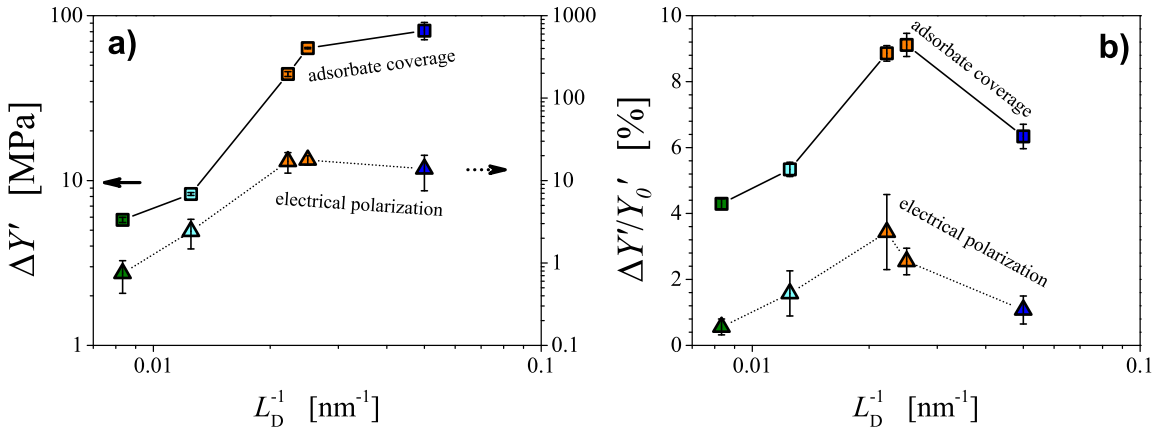

Figure 4.9. Variation of the charge-induced amplitude of the storage modulus as a function of the inverse ligament size, L_D^{-1}, in 1 M $HClO_4$: (a) absolute values $\Delta Y'$, calculated as a height of the peak in Y' occurred due to OH-adsorption (squares) or electrical polarization (triangles), (b) relative values $\Delta Y'/Y_0'$, calculated as $\Delta Y'$ normalized by an actual Y_0' measured just before the peak onset. Here, the color code in the legend and designation of the samples measured correspond to one in Fig. 4.8.

the ligament size. From Fig. 4.9a, one can see that the np-Au structure with the smallest (L_D = 20 nm) and intermediate feature size (L_D = 40 nm) result in the comparable values of the charge-induced modulus that reaches ≈ 100 MPa for the OH-adsorbate-covered and ≈ 10 MPa for the negatively charged surface, respectively. Since the initial absolute elastic modulus for 20 nm is higher than for 40 nm (Fig. 4.8), the relative changes $\Delta Y'/Y_0'$ appears to be smaller for the former structural size (Fig. 4.9b). In other respects, for the samples with L_D > 40 nm, the electrochemically modulated stiffness is a size-dependent, being in agreement with the previous reports on a decrease of the stiffness when the ligament diameter decreases [102, 172].

Even though more research on the size-dependance of the stiffness needs to be undertaken before firm conclusions can be made, the pronounced effect of the length scale on the effective elastic modulus tuned by electrode potential in Fig. 4.9 testifies to the implications for the surface excess elasticity phenomena (Section 2.2.1). The signature of the surface excess elasticity in *in situ* DMA results will be discussed in Chapter 5.

4.3.3 Impact of frequency

Figure 4.6 reveals that the loss modulus values are quite low, but do significantly change with electrosorption. The significant reduction of the loss modulus may suggest a suppression of surface processes (e.g., rearrangements of surface atoms) when oxygen species adsorb. The rearrangement of surface atoms in clean surfaces induced by the applied strain apparently would be rate dependent. To probe whether the dissipative losses exhibit sensitivity to a frequency of the applied mechanical stress *in situ* DMA frequency sweep experiments were performed at different constant potentials, using the chronoamperometry method (Section 3.2.1). Np-Au with L_D = 40 nm underwent tuning between oxygen-covered and clean surface states (corresponds to 1.46 and 0.81 V vs. SHE, respectively) in a frequency window, from 1 to 25 Hz. The potential-time profile is shown in Fig. 4.10a and the resulting response of the storage Y' and loss Y'' moduli is displayed in Fig. 4.10b.

The results indicate that the relative variation of the storage modulus at frequencies from 1 to 25 Hz remains constant, whereas the relative variation of the loss modulus decreases towards larger frequencies. The overall increase in the the absolute values of Y' and Y'' is may be attributed to the irreversible densification as has been discussed in Section 4.3.1.

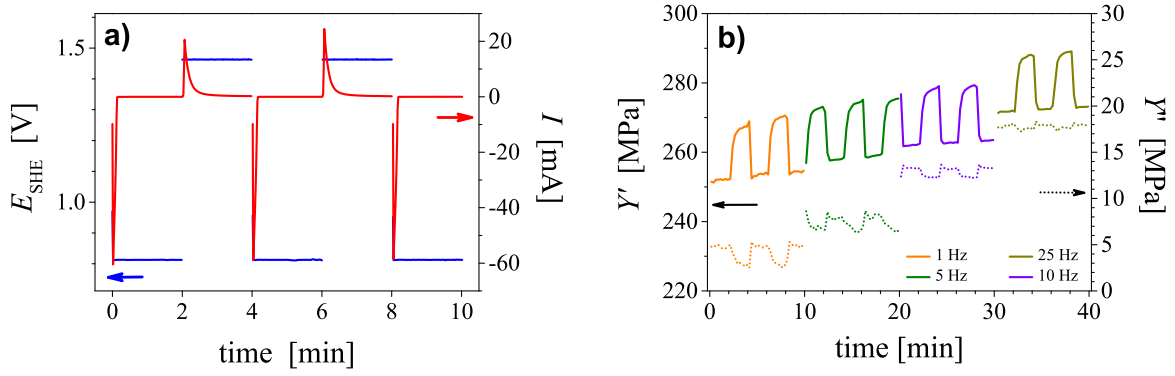

Figure 4.10. A frequency sweep experiment on np-Au (L_D = 40 nm) during the applied potential steps between 1.46 and 0.81 V vs. SHE in 1 M $HClO_4$. (a) Potential E – time t profile and the resulting current flow in the first 10 min of the measurement when a frequency of 1 Hz was applied. The same potential steps were repeated for the subsequent frequencies. (b) Storage E' (left) and loss modulus E'' (right) vs. time. Lower moduli observed here are due to deviations in ligament size of the samples.

As preliminary, the frequency sweep measurement fails to resolve any impact of the frequency on the loss modulus of np-Au upon the clean-surface conditions. This means that experiments which simply investigate this dependency in the limited frequency window may not be sufficient to clarify the microscopic nature of the active mechanism. Measurements that explore frequency dependence along with temperature dependence in an effort to arrive at an activation energy for the dissipative process are thus required. This, however, involves a major experimental effort which is beyond the scope of this thesis.

4.3.4 Impact of anions with different adsorption strength

In view of the specific interaction between the adsorbed species and metal surfaces (Section 2.3.1), the elastic response of np-Au was studied in aqueous solutions, which contained anions with different degree of specific adsorption on Au. These electrolytes were 0.7 M NaF, 1 M $HClO_4$, 0.5 M H_2SO_4, 1 M $HClO_4$ +10^{-3} M NaCl, and 0.5 M H_2SO_4 +10^{-3} M NaBr. Increasing anion-gold interactions of these anions follows a sequence

$$F^- \approx ClO_4^- < SO_4^{2-} < Cl^- < Br^-, \tag{4.1}$$

i.e. the adsorption strength increases by moving from fluoride to bromide. The hierarchy of adsorption effects of these anions reflects the decreasing energy of solvation of these species [173] and emerges in the shift of the potential of zero charge, E_{zc}, of metal by various anions.

Here, the halides (chloride Cl^- and bromide Br^-) were chosen because of their weakly bound solvation shells, so that they adsorb easily on metal surfaces and form a direct chemical bond with it [132, 173]. In contrast, fluoride F^- and perchlorate ClO_4^- ions are considered to be strongly solvated ions and weakly bond to Au [113]. The behavior of the sulfate SO_4^- is attributed as a strongly adsorbed on Au [174], although this anion is less specifically adsorbed than the halides [173].

The specific adsorption of the halide ions was examined in the presence of a large excess of an inert electrolyte with the higher concentration (supporting electrolytes $HClO_4$ and H_2SO_4). This was necessary in order to maintain a sufficient electrical conductivity of the solutions [175] and minimize the amount of the specifically adsorbed species in the diffuse double layer (DL) [132]. Both acids $HClO_4$ and H_2SO_4 are considered as common supporting electrolytes when work in aqueous media [175]. Adding a small amount of Cl^- and Br^- to

these solutions would then enable monitoring of the effect these electroactive anions cause on the mechanical response of np-Au as compared with less active perchlorate or sulfate.

Figure 4.11 shows the impact of the anions on the cyclic voltammetry curves (CVs), the length change variation (Δl), as well as on the moduli (Y' and Y'') measured by the *in situ* DMA. The values of the corresponding peak amplitude ($\varepsilon_{\mathrm{dyn}}$) during mechanical oscillations as well as effective macroscopic static stress (σ_{st}) used for each specimen in each specific solution are given in the caption. The key results of the experiments are discussed below.

Current (I)–potential (E) profiles

The CVs recorded in the presence of the four different anions as depicted on the top of each diagram display very similar forms. The common features of the processes of electrochemical surface oxide film formation and reduction on Au are present on all $I-E$ dependences. On the scale of the oxidation peaks the charging current in the double layer appears to be constant. In general, the CVs are quite similar to the previous reports on planar Au [176–178] or np-Au electrodes [171] in the solutions under the study.

It should be noted that a comparative analysis of the magnified regions of the capacitive regime in the presence of the specific anions becomes complicated because the differences in the CVs between planar and np-Au electrodes can be primarily related to surface roughness. Apart from that, effects of scan rate or trace impurities can emerge in different studies. In the current work it was sufficient to employ the CVs as a monitor for surface reproducibility of the np-Au electrode as well as for investigation of the mechanical properties in a potential region, covering positively and negatively charged surface states. The latter is indicated on the CVs by the *pzc* values as obtained for np-Au by the immersion method (Section 3.4.3). It was found that $\mathrm{E_{zc}}$ on np-Au in the investigated electrolyte solutions follows the order (vs. SHE):

$$\mathrm{F^-} > \mathrm{SO_4^{2-}} > \mathrm{ClO_4^-} > \mathrm{Cl^-} > \mathrm{Br^-}. \tag{4.2}$$

Although the sulfate anion appears to be less adsorbable than the perchlorate here, a trend of shifting the *pzc* value in a negative direction when the specific adsorption of $\mathrm{Cl^-}$ and $\mathrm{Br^-}$ anions occurs is in good agreement with similar studies on planar Au electrodes [179]. Taking into account the fact that to date no systematic assessment of the *pzc* on np-Au has been yet performed, the immersion method seems to be a reliable technique for such measurements. A position of the *ocp* as a starting point of the measurements is also provided in Fig. 4.11.

Length change Δl

One can see a substantial effect of $\mathrm{F^-}$, $\mathrm{SO_2^{-4}}$, and $\mathrm{Br^-}$ anions on the potential-induced variation of the actuation amplitude. Especially, the changes in the shape of the $\Delta l-t$ curve is clearly evidenced from a comparison between measurements in $\mathrm{H_2SO_4}$ and 0.5 M $\mathrm{H_2SO_4}$ +10^{-3} M NaBr. A downward drift of Δl with time also shows up here, being consistent with the analogous observation in 1 M $\mathrm{HClO_4}$ (Section 4.3.1). After subtraction of the drift and averaging over the CV cycles a reversible part of the length change Δl normalized to the initial input length of a sample l_0 (strain amplitude $\Delta l/l_0$) was plotted versus electrode potential E for the acidic (Fig. 4.12) and alkaline (Fig. 4.13) solutions. In excellent accordance with the previous studies [70, 171], for two electrolytes, 1 M $\mathrm{HClO_4}$ and 0.7 M NaF, one recognizes here a various hysteresis between the oxidation and reduction peaks.

By virtue of Eq. (3.16) more positive strain corresponds to more negative surface stress, and in view of Eq. (2.19) a positive sign of a slope to the $\Delta l/l_0-E$ data implies a negative sign of the electrocapillary coupling parameter ς (Section 2.3.2). The change in sign of ς for np-Au is therefore observed only in the OH-adsorption regime of the CV in 0.5 M $\mathrm{H_2SO_4}$ +10^{-3} M NaBr solution (Fig. 4.12d).

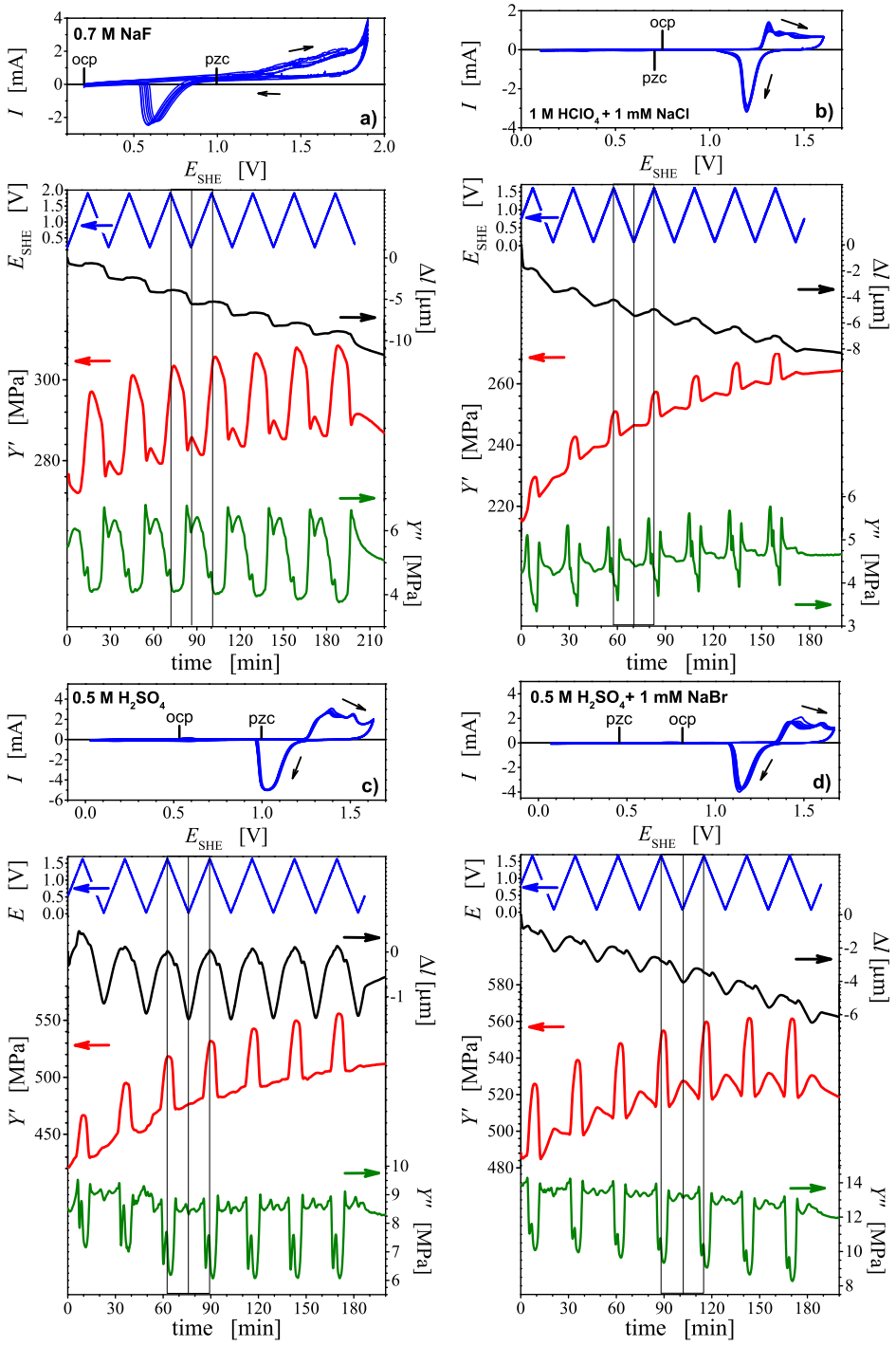

Figure 4.11. Response of np-Au (L_D = 40 nm) to potential cycling measured by *in situ* DMA at a loading frequency of 1 Hz in (a) 0.7 M NaF (ε_{dyn} = 0.66%, σ_{st} = 3.5 MPa), (b) 1 M $HClO_4$ + 1 mM NaCl (ε_{dyn} = 0.70%, σ_{st} = 2.8 MPa), (c) 0.5 M H_2SO_4 (ε_{dyn} = 0.50%, σ_{st} = 2.2 MPa), (d) 0.5 M H_2SO_4 + 1 mM NaBr (ε_{dyn} = 0.57%, σ_{st} = 3.4 MPa). CV in each solution was measured for 7 successive cycles and potential scan rate of 2 mV/s. Vertical lines mark vertex points of CV for one exemplary cycle. Somewhat lower moduli measured in (a) and (b) are due to deviations in ligament size of the samples.

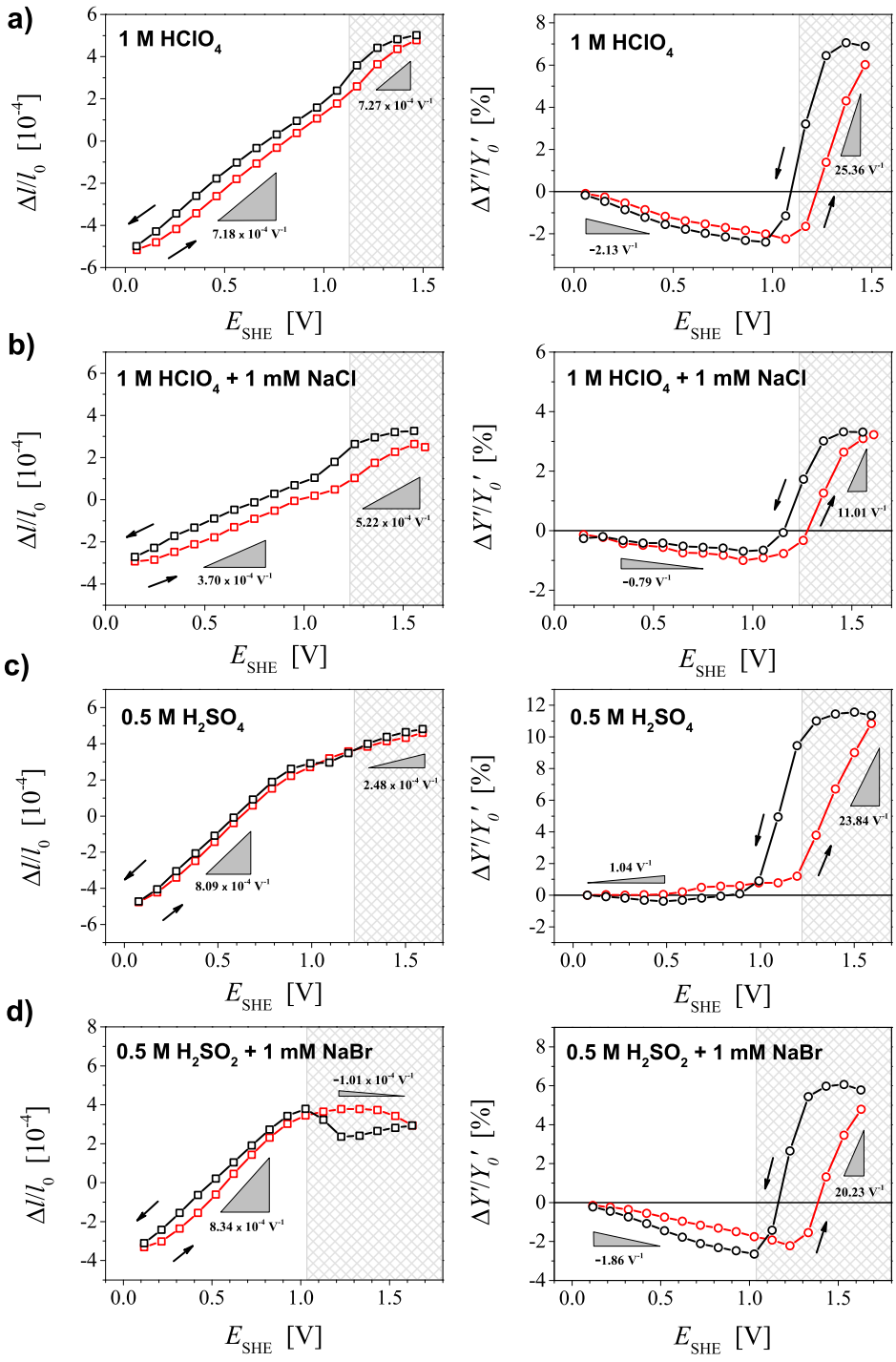

Figure 4.12. Macroscopic strain $\Delta l/l_0$ (left) and relative variation of the storage modulus $\Delta Y'/Y_0'$ (right) of np-Au (L_D = 40 nm) measured by *in situ* DMA in acidic electrolytes (pH < 7) vs. electrode potential, E. The shaded regions denote OH-adsorption/desorption regime. Also shown are the slopes of the linear fit to the anodic part of the data for the two states of the surface, clean and oxide-covered. Arrows indicate the direction of scan.

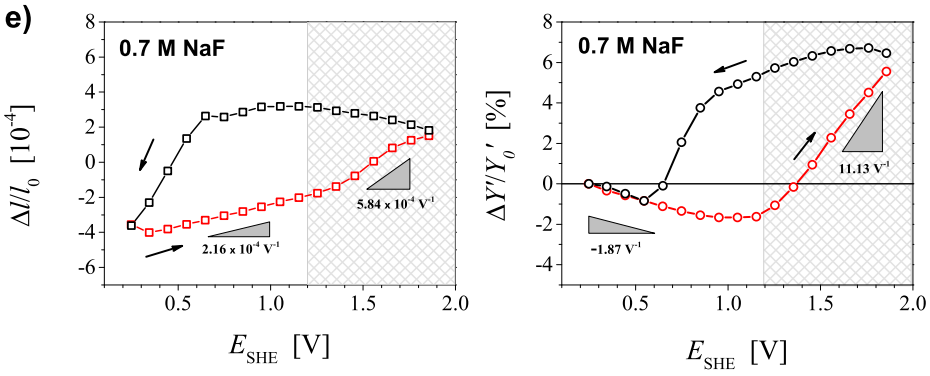

Figure 4.13. Macroscopic strain $\Delta l/l_0$ (left) and relative variation of the storage modulus $\Delta Y'/Y_0'$ (right) of np-Au (L_D = 40 nm) measured by *in situ* DMA in alkaline electrolyte (pH > 7) vs. electrode potential, E. The shaded region denotes OH-adsorption/desorption regime. Also shown are the slopes of the linear fit to the anodic part of the data for the two states of the surface, clean and oxide-covered. Arrows indicate the direction of scan.

Storage modulus Y'

A pronounced increase of the storage modulus around the positive end of anodic sweep on each CV is associated with electrochemical oxidation of the surface. A shape of this first maximum well reproduces one observed in $HClO_4$ (Section 4.3.1). However, when we now turn to the double layer charging region we see the significant differences in the response of Y' from one anion to another, which in particular evident in NaF and H_2SO_4 (Fig. 4.11). A respective comparison of the storage modulus (Y')–electrode potential (E) relationships during anodic scan for all electrolytes is shown in Fig. 4.14. It is apparent from the data that within the double layer potential window the nonspecifically adsorbed fluoride species enhances the compliance of the material most of all, whereas the sulfate enhances the stiffness. This is confirmed by the values of the slopes determined from the straight line of best fit to the $\Delta Y'/Y_0'$-E data in the potential window 0...1 V during capacitive processes (Tab. 4.2).

Table 4.2. Values of the slopes of from straight-line fits to the $\Delta Y'/Y_0'$-E data in Fig. 4.14 within double-layer regime (0...1 V vs. SHE).

Anion	Slope value, V^{-1}
F^-	-2.40
ClO_4^-	-2.18
SO_4^{2-}	0.92
Cl^-	-1.01
Br^-	-1.75

Loss modulus Y''

A form of Y''–t curves resembles that one that is characteristic for $HClO_4$, except one for NaF. A general observation here is a complexity of the changes in the losses for all four anions under consideration. Differences in nature of the anions interaction with Au surface along with their influence on the onset of the oxidation [140, 176] suggest that the Y'' behavior might reflect distinct stages of these surface processes. Moreover, such processes can be rate-dependent and require a supplementary examination on the impact of frequency.

Irrespective of how the behavior of both moduli, Y' and Y'', is affected by the electrolytes,

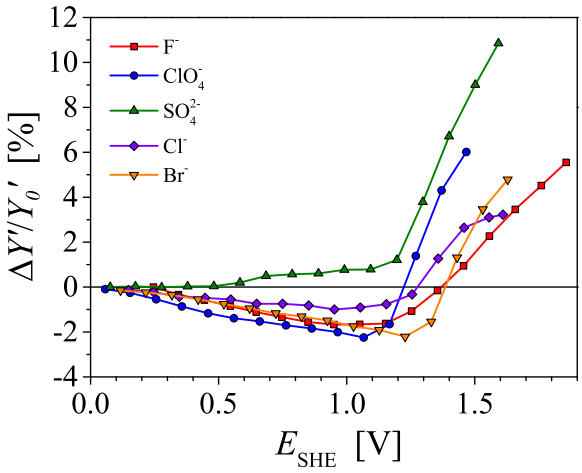

Figure 4.14. Comparison of influence of F^-, ClO_4^-, SO_4^{-2}, Cl^-, and Br^- anions on the elastic response of np-Au electrode (L_D = 40 nm). Variation of the storage modulus $\Delta Y'/Y_0'$ (averaged over all CV cycles) as a function of the electrode potential E measured at 1 Hz in anodic direction. Y_0' refers to the first data recorded as the potential cycling was applied.

the systematic dependence of the induced changes in the effective macroscopic elasticity on the anionic adsorption strength in the whole range of potentials leads to the conclusion that the surface processes do play an important role in elastic response of np-Au.

4.4 Plastic behavior in aqueous electrolytes

4.4.1 Electrical modulation of plastic flow in $HClO_4$ and H_2SO_4

Impact of potential steps

The use of *in situ* compression testing apparatus developed in the current work (Section 3.5.2) made possible a study of a dependance of the plastic deformation of np-Au bulk macroscopic specimens upon the processes at ligament/electrolyte interface. The experimental procedure was nearly similar to that employed for *in situ* DMA investigations (Section 4.3.1) with an exception that during continuous loading in a testing – as opposed to cycles in a DMA – a sample was subjected to a sequence of the potential steps of increasing magnitude in the anodic, and then a reverse cathodic direction. The steps were applied in accordance with a CV recorded in a test solution right before the compression test. An example CV in 1 M $HClO_4$ electrolyte is presented in Fig. 4.15a. In order to study the effect of the polarization on the plastic behavior, the bulk np-Au samples were loaded up to 20% of the engineering strain prior subjecting to the voltage steps (the experimental procedure is described in Section 3.5.2).

A typical stress-strain curve in engineering coordinates for np-Au with an average ligament size of 40 ± 5 nm in 1 M $HClO_4$ is shown in Fig. 4.15b. A holding time of a each potential step corresponded to ~ 2.9% of the strain. By comparing the compression curve in Fig. 4.15b with one recorded for a similar sample in air (Fig. 4.3, orange line), one can recognize the remarkable influence of the test environment, namely the pronounced variations of the flow stress in excellent agreement with the applied voltage. Although tuning of the flow stress by electrical signals in np-Au in $HClO_4$ has been already reported [15], a detailed study of processes in the capacitive region is still missing. The observations in Fig. 4.15b reproduce the following important features:

- The most noticeable variation of the flow stress is observed within the potentials steps of 1.3 and 1.4 V. It is associated with adsorption of OH^- ions on the ligament surfaces.

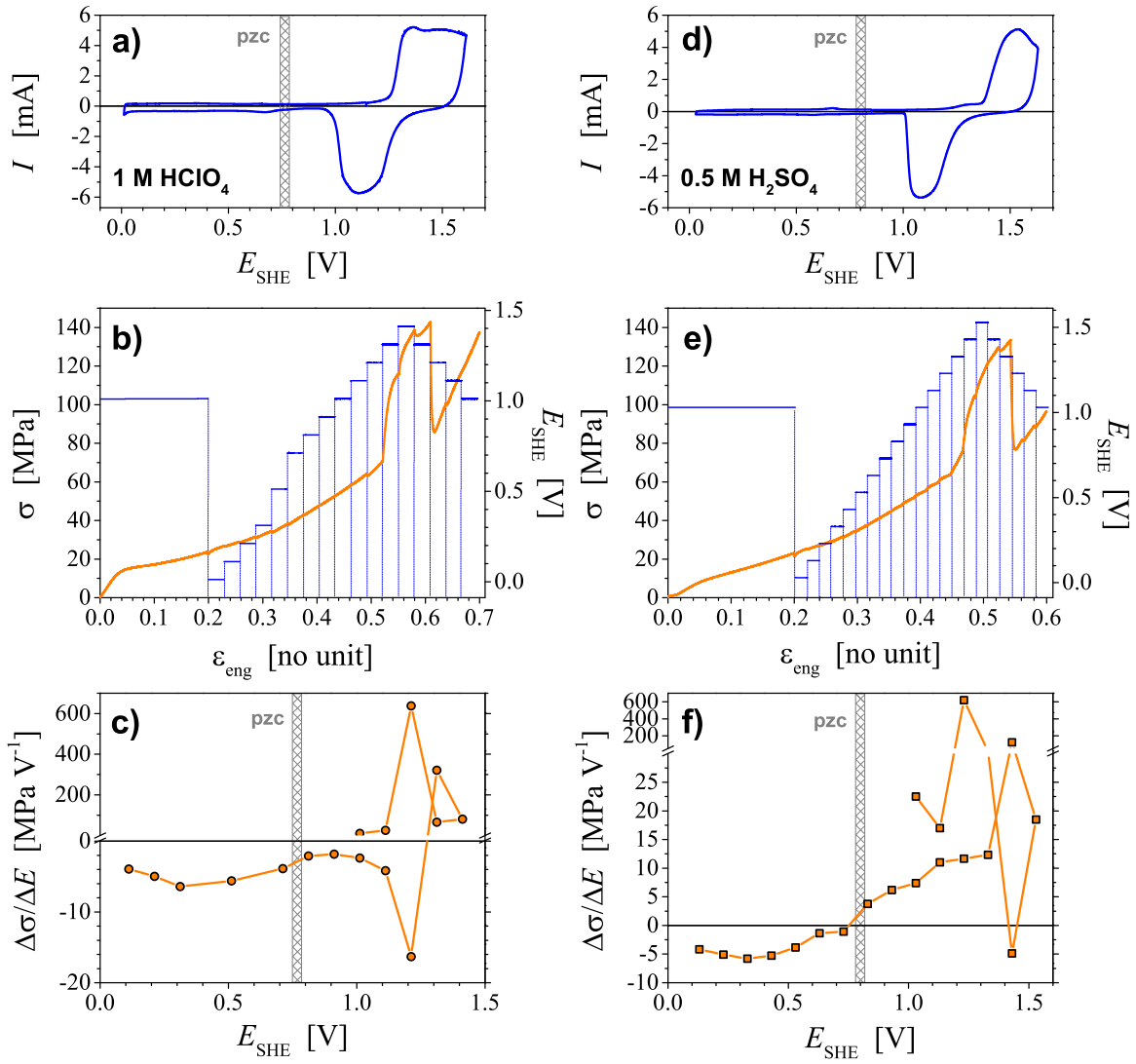

Figure 4.15. Results of *in situ* compression tests of np-Au (L_D = 40 nm) in 1 M $HClO_4$ (left) and 0.5 M H_2SO_4 (right): (a, d) CVs recorded right before the mechanical tests at scan rate of 5 mV/s, (b, e) stress-strain diagrams at constant engineering strain rate 10^{-5}/s (solid orange line) with superimposed potential steps (solid blue line), (c, f) effective response of the flow stress to the electrode potential jumps calculated as $\Delta\sigma/\Delta E$. The potential was modulated over the whole range of the CV with a step of 0.1V. Note a different scale for the capacitive- and OH-regions in $\Delta\sigma/\Delta E$–E dependences. A range of the zero charge potential is marked as "pzc".

- Changes in strength are reversible and large, the adsorption increases the flow stress by factor of two (from ≈ 70 to 140 MPa).

- Smaller but still well reproducible and detectable variation of the flow stress is also produced due to capacitive charging of the surfaces.

The latter is of significant interest since a precise and careful study of flow stress as a function of potential in the electrical double layer could clarify a mechanism responsible for the high strength here owing to its expected "electrocapillary" nature (Section 1.2.2).

Figure 4.15c details the plastic flow behavior in the whole range of the capacitive range (0.1...1.2 V) in 1 M $HClO_4$. To characterize the effect of potential on strength a parameter $\Delta\sigma/\Delta E$ has been introduced. It is determined as a ratio of a drop in the flow stress $\Delta\sigma$ occurred upon switching a potential from E_1 to E_2 to a difference in these voltage values $\Delta E = E_2 - E_1$ (Fig. 4.16). A negative magnitude of the ratio implies weakening of the

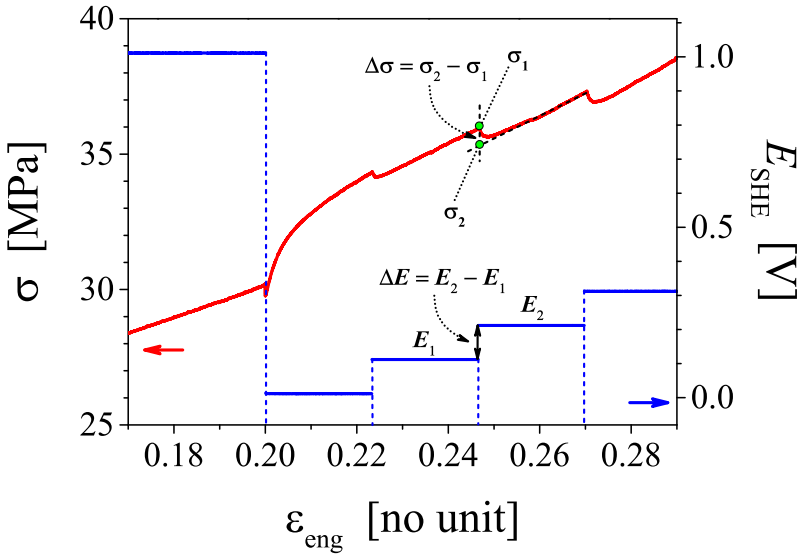

Figure 4.16. An illustration of the evaluation of $\Delta\sigma/\Delta E$ parameter from the stress-strain data for np-Au with L_D = 30 nm. The potential pulses range from 0.01 to 0.31 V vs. SHE RE.

material, while a positive one reflects a trend of increasing strength. It is noteworthy that behavior of $\Delta\sigma/\Delta E$ near the potential of zero charge – a point where a charge changes its sign on the electrode surface – keeps its negative sign.

At potentials between 1.1 and 1.2 V an abrupt drop in $\Delta\sigma/\Delta E$ is observed. Overcoming a potential value of 1.2 V leads to pronounced rise of the effective response of σ due to OH-film formation. Upon reversible potential jumping to 1.0 V the parameter $\Delta\sigma/\Delta E$ almost retained its low value, approaching zero.

Turning now to the flow stress behavior in the presence of sulfate, an anion that adsorb more strongly on Au than perchlorate. A CV in Fig. 4.15d finds essentially the same features that are typical for Au electrode in $HClO_4$, except a shift of the oxidation onset to more positive potentials. The latter is in good agreement with literature reports on Au electrodes in H_2SO_4 solutions [174, 180]. A curve $\sigma - \varepsilon_{eng}$ for H_2SO_4 lies below that one for $HClO_4$ at strains up to 0.2 due to slight differences in the ligament diameters for both samples (Fig. 4.15e). What is interesting in this data is that $\Delta\sigma/\Delta E$ inverses its sign from negative to positive near the *pzc*, in opposition to its behavior in $HClO_4$ (Fig. 4.15f). The strengthening of np-Au here occurs long before the process of OH-adsorption, pointing out to substantial differences between the plastic response of np-Au in $HClO_4$ and H_2SO_4.

Another striking observation emerges from the data comparison between the potential-modulated storage modulus (Fig. 4.14) and flow stress (Fig. 4.15c and f) for the two acidic solutions. Note how precisely the parameter $\Delta\sigma/\Delta E$ replicates the drop in $\Delta Y'/Y_0'$ around 1.1 V in case of $HClO_4$ or rise of the stiffness at 0.6 V in case of H_2SO_4.

4.4.2 Impact of ligament size

Compression tests using potential steps were applied also to the samples with different ligament sizes. The results are summarized in Fig. 4.17.

One can recognize a well-known increase of σ with decreasing L_D in a good agreement with the results from compression tests in air (Fig. 4.3). The coupling parameter $\Delta\sigma/\Delta E$ follows the same trend. It is remarkable that a normalization of the coupling parameter to the actual value of the flow stress, σ_0, the behavior for all three samples coincides and does not dependent on L_D (Fig. 4.17c and f). This observation may suggest the same mechanism for the size-dependent and potential-induced strength. In this respect possible relevant mechanisms that control the plastic deformation will be discussed in Chapter 5.

4.4.3 Impact of anions with different adsorption strength

To check whether the sign-inverted response of the flow stress is observed in other electrolytes, the flow stress-electrode potential coupling parameter $\sigma_0^{-1}(\Delta\sigma/\Delta E)$ was determined during *in situ* mechanical testing in the presence of different anions as in *in situ* DMA experiments in Section 4.3.4. Figure 4.18 reports the results. In the region where OH-adsorption starts in each electrolyte $\sigma_0^{-1}(\Delta\sigma/\Delta E)$ increases rapidly. A gradual decreasing of the coupling parameter $\sigma_0^{-1}(\Delta\sigma/\Delta E)$ after 1.4 V in case of NaF occurs as the oxidation peak in the CV attains a quasiplateau (Fig.4.11a), and is typical for the behavior of $\sigma_0^{-1}(\Delta\sigma/\Delta E)$ in other solutions at such conditions (not shown in the Fig. 4.18a). Figure 4.18b magnifies the intervals where the double layer capacitive charging prevails, indicating that the strongly adsorbing ions (Cl^- and Br^-) have less impact on the plastic flow of np-Au compared to the weakly adsorbed F^- and ClO_4^- or SO_4^{2-}. Overall, the parameter $\sigma_0^{-1}(\Delta\sigma/\Delta E)$ demonstrates a tendency to increase near the *pzc* for fluoride, perchlorate, and sulfate, apparently reflecting an order of these ions in the sequence (4.2). The sign-inversion behavior only occurred in H_2SO_4.

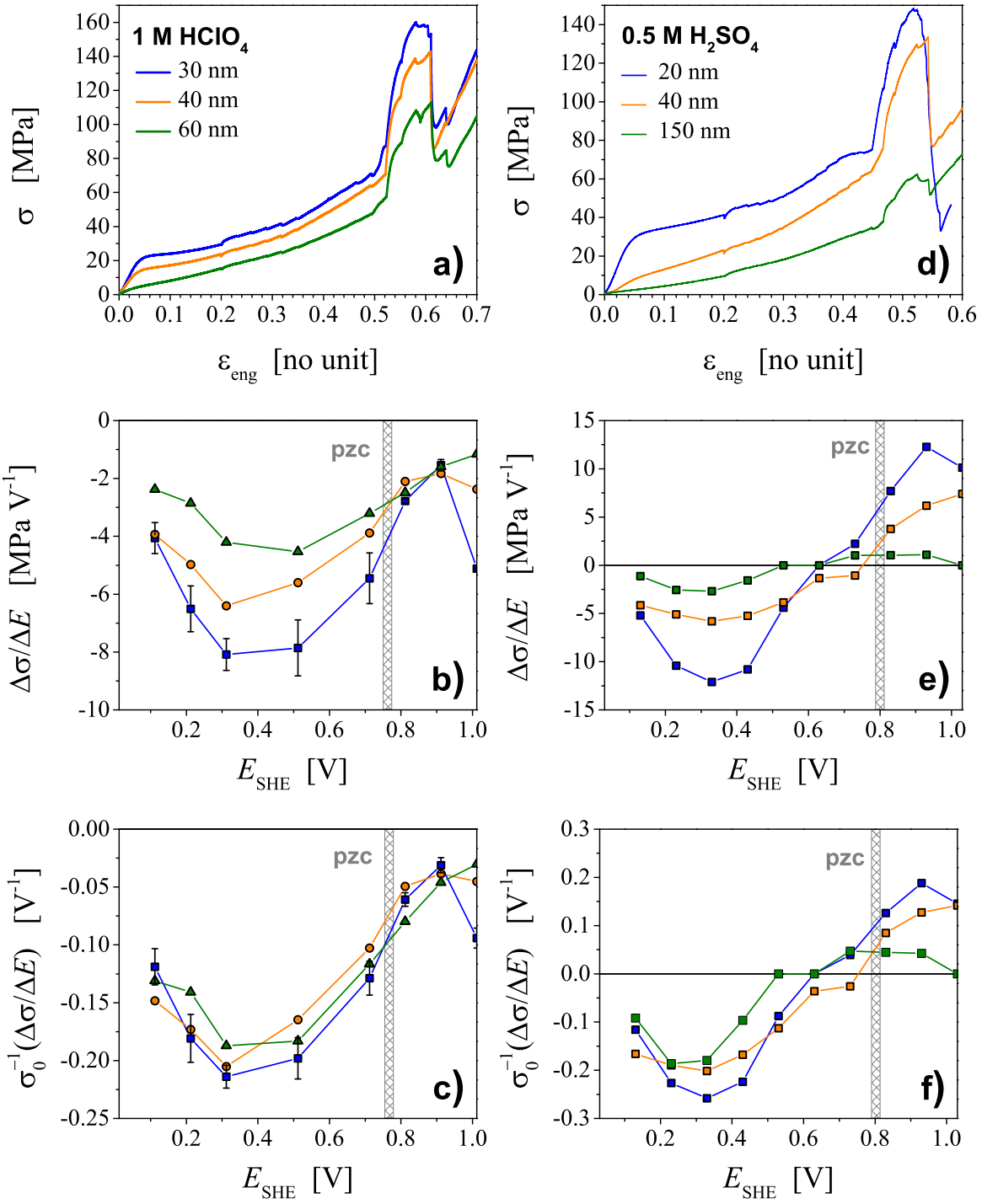

Figure 4.17. Influence of the ligament size on flow stress σ and the coupling between σ and electrode potential E in 1 M $HClO_4$ (left) and 0.5 M H_2SO_4 (right): (a,c) σ vs. strain ε_{eng} during deformation with strain rate 10^{-5}/s in compression for three different ligament diameters, (b,e) effective response of σ to potential jumps, E, calculated as $\Delta\sigma/\Delta E$, (c,f) the parameter $\Delta\sigma/\Delta E$ is normalized to the actual value of flow stress, σ_0. Note no size-dependent behavior in this case. A range of the zero charge potential is marked as "pzc".

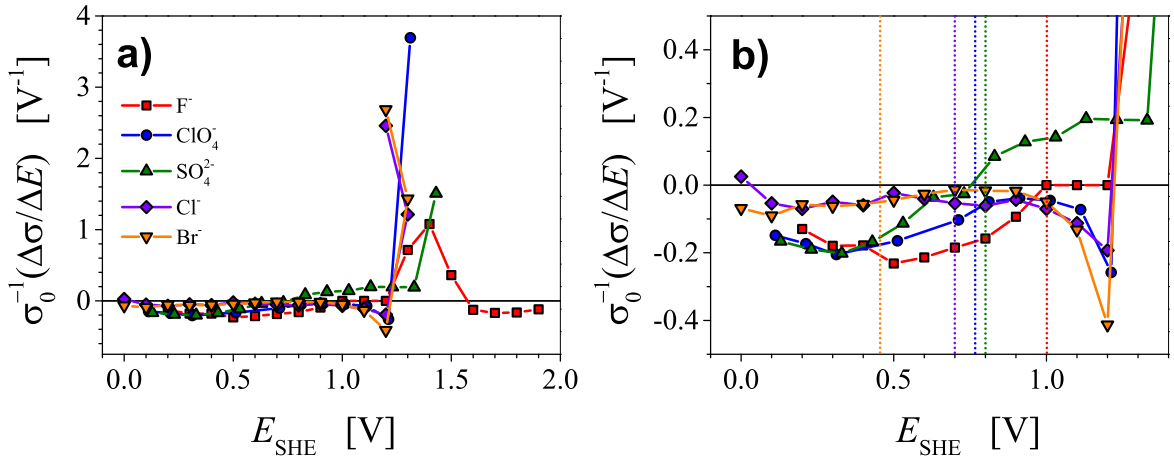

Figure 4.18. Normalized coupling parameter $\sigma_0^{-1}(\Delta\sigma/\Delta E)$ of np-Au (L_D = 40 nm) obtained at different anions during potential steps going in anodic direction vs. SHE: (a) in the whole range of CVs, (b) in the capacitive regime. The zero charge potential of np-Au measured by the immersion method is marked by dotted lines, where a color code for each anion corresponds to one in the legend.

Chapter 5

Discussion

5.1 Mechanical behavior under compression in air

5.1.1 Early plastic deformation

The stress-strain behavior of np-Au during compression (Fig. 4.3, 4.4) already shows yielding at the early stage of the plastic deformation. The unloading/reloading segments accompanied the compression curves resolve this first deformation even for specimens with the smallest ligament size of 20 nm.

This finding agrees with those observed in earlier investigations, in which mechanical testing of np-Au mm-sized samples in compression revealed an extended microplastic regime [93, 94, 167]. Because the deviation from the linearity occurs in the reported stress-strain curves almost instantly, the application of the conventional criterion to define the effective yield strength (at 0.2% strain) becomes problematic. Nonetheless, the authors identified the onset of macroplasticity either at 1% of plastic strain [94] or at the point where the stress-strain curve is no longer linear [93, 98]. As a result, the effective yield strength of np-Au with ligament sizes between 15 and 55 nm appears in the range of 7.5 – 27 MPa.

Such behavior of np-Au with no clearly defined yield point has been well-reproduced by the recent molecular dynamics simulations (MD), where a perfect match between a simulated and an experimental stress-strain curve from this work (curve with 40 nm ligament diameter in Fig. 4.3) has been found [99]. The computer simulations have provided a direct insight into mechanisms involved in the deformation of np-structure at the atomic scale. One can adopt the conclusions suggested by the MD to explain the observed deformation behavior in the experiment, even though the virtual np-Au sample possessed one order of magnitude smaller ligament diameter than the experimental one. The authors used the np-Au samples that display a compatible microstructure with ligaments free of adsorbates. Therefore, the modeling is justifiable to clarify the processes governing the experimentally observed mechanical behavior of the nanoporous material in a "clean" dry state.

The MD study has detected *early dislocation activity* manifested by immediate increase of a dislocation density. Moreover, the dislocations have been found to be already present in the ligaments initially, before the compression. The density of planar defects such as twin boundaries and stacking faults has also increased upon the first loading. Origin of the initial dislocation density has been explained by the stress induced in the bulk through the action of surface stress. This bulk stress can reach a significantly high value of 1 GPa in case of a nanosized ligament [7, 181], provoking sudden dislocation generation and the consequent plastic flow [99, 182].

However, the initial dislocation activity is not the only reason for the immediate plasticity of np-Au. *Heterogeneity* of the np-structure, which arises from differences in shape, size, and orientation of the ligaments, can cause different surface-driven stresses locally. In other words,

while some ligament will already yield, others might still sustain the prestress initiated by the surface stress. Such nonuniform action of the surface-induced prestresses can, therefore, give rise to the spontaneous yielding [99].

It should be noted that analogous features in mechanical response, including the extended microplastic regime, ill-defined yield strength, and heterogeneous deformation have been also recognized in nanocrystalline materials (see for instance [183]).

5.1.2 High compliance

The mechanical behavior of np-Au under conditions of compression with introduced unloading/reloading stages reveals another two remarkable observations: unusually low stiffness at the beginning of deformation and a strong subsequent stiffening as the deformation proceeds (Fig. 4.4). A result for the effective Young's modulus, Y^{eff}, at the onset of strain is at least one order of magnitude lower than what was derived in several previous investigations of np-Au (Fig. 1.4a). Experiments involving nanoindentation, film bending, and micro-tensile or compression tests found Y^{eff} in the range $3-13$ GPa for ligament sizes of $20-40$ nm [87, 93, 102, 168]. In contrast, the samples with similar size of the ligaments tested here exhibit the Young's modulus within $0.3-0.8$ GPa.

The specimens fabricated in the current study are of the crack-free type that the earlier studies have shown to be perfectly deformable in compression [15, 94] and to yield strong and ductile nanocomposites when infiltrated with polymer [167]. Therefore, structural imperfections such as native cracks as the origin of the large compliance can be ruled out here. Moreover, it is significant that the consistent results were obtained both by the mechanical testing machine and DMA with a series of samples from different batches.

The higher stiffness reported by other authors could be attributed to densification during loading (in the case of nanoindentation) or synthesis (thin films). Synthesis by dealloying often entails large volume shrinkage [69], thereby densifying and, hence, stiffening the material. The underestimation of the relative density due to the dimensional changes after dealloying can cause erroneous correlation with properties of nanoporous metal and therefore explain the discrepancy. Even when bulk shrinkage is prevented, np-Au macroscopic samples produced via alloy corrosion may exhibit densified layers at its surface as has been documented in Ref. [141]. One may expect a significant influence of this denser and, hence, stiffer layer on the elastic properties of np-Au films if they are thin enough. Careful and precise density measurements in future studies might reveal a role of this parameter for the stiffness of np-Au samples. Regardless of the origin of the different stiffness values, the conventional mechanical testing of mm-sized samples applied in this work emerges as a conservative and reliable method. Additionally, the excellent agreement between results of the macroscopic compression tests and DMA (Fig. 4.5) further supports the significance of the empirical finding of unusually high compliance.

It is noteworthy that the numerical modeling using the Finite Element Method (FEM) reproduces the low stiffness of np-Au examined in the present work [109]. In the FEM simulation the nanoscale network structure of np-Au is modeled by a diamond lattice of spherical nodes that are connected by cylindrical struts (ligaments). The model implements a random displacement of the node positions from the lattice sites. By employing this approach, a good match between simulation results and experimental observations has been found. The decisive impact of the displacement amplitude on the elastic behavior underlies the relevance of *microstructural disorder* or *heterogeneity* in the nanoscale network structure for the elastic behavior. Now the question is how to define and measure a suitable order parameter in an experiment. Although visual inspection of electron micrographs of np-Au microstructure fails to find any topological differences between different samples, various synthesis procedures (free or electrochemical corrosion, annealing, etc.) might presumably result in subtle changes of the order of the nanoscale network that affect its elastic response.

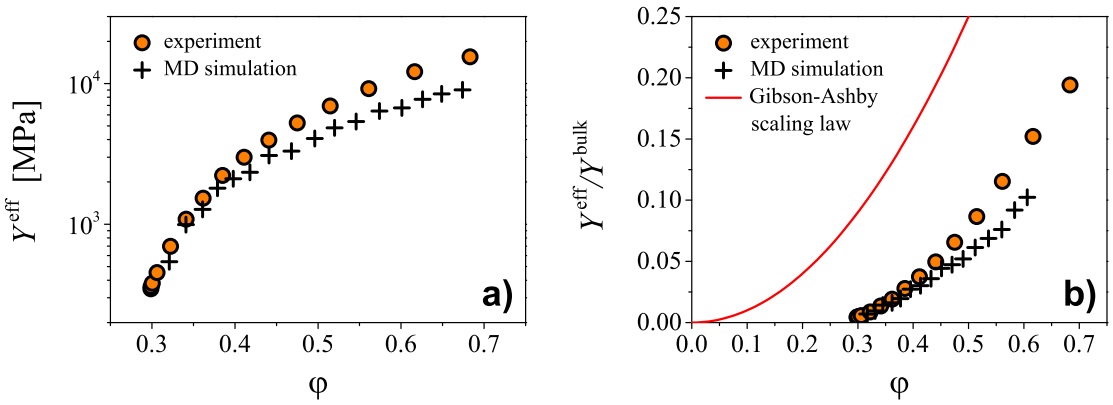

Figure 5.1. Effective elastic properties of np-Au during compressive deformation. (a) Young's modulus, Y^{eff}, as function of the relative density, φ. Experimental data points correspond to a sample with $L_D = 40 \pm 5$ nm (from Fig. 4.3) and the simulation data were obtained by molecular dynamics simulations (MD) using a virtual np-Au sample with $L_D = 3.15$ nm (the MD data are courtesy of Nam Ngô, Helmholtz-Zentrum Geesthacht; the detailed study is presented in [99]). Both data sets represent tangent moduli (for details see Section 3.4.4). (b) Normalized Young's modulus vs. relative density, comparison with Gibson-Ashby scaling law for an open-cell foam. The parameters used in the Gibson-Ashby scaling equation (1.2): the elastic modulus of gold $Y^{bulk} = 80$ GPa and the pre-factor $C_2 = 1$ derived for foams with low density [89].

The MD simulations mentioned in Section 5.1.1 detected the analogous elastic softening while deforming np-Au in compression [99]. Figure 5.1a compares the MD results with one of the tests from the current work. Both the simulation and experiment employed load-unload during compression to evaluate the Young's modulus as the relative density of the material increases. An excellent agreement between two data sets can be seen. Even despite the discrepancy in ligament size, the effective elastic moduli, Y^{eff}, determined from the unloading/reloading segments by both approaches are found to be essentially identical.

As possible origins of the high compliance it has been suggested that, apart from the microstructural disorder, the *surface-induced shear stress* in nanosized ligaments plays a major role in reducing the stiffness of np-Au. The spontaneous nucleation of dislocation driven in np-Au by the surface stress as seen by another MD study [182] implies the deviatoric (or shear) components of the induced stress in the bulk (as was predicted in Ref. [127]). For thin and long nanoligaments with a given value of the surface stress magnitudes of the shear components can approach or even exceed the theoretical shear stress. Furthermore, the heterogeneity of the plastic deformation of np-Au would involve ligaments with a distribution of the shear stress, and hence regions with an elastic instability. The latter would diminish the shear modulus. Full consistency of the experiment from this work with the modeling, thus, allows to employ this explanation as paramount one for the observations here.

To further analyze elastic response of np-Au and separate the effect of the relative density from the capillarity effects, its elastic modulus-relative density relationship has been compared with the Gibson-Ashby scaling law for an open-cell foam (Eq. 1.2, Chapter 1) in Fig. 5.1b. Although this scaling law has been derived and experimentally validated for open-cell materials with macroscale porosity and low density < 0.1 [184], it is widely discussed in literature as a starting point to explain the elastic behavior of np-Au [67, 80, 93, 98, 172, 185]. Most of these studies [66, 93, 97, 172] agree that it fails to predict the elastic modulus of the material, while other investigations find reasonable agreement with their experimental data [80, 98] (Fig. 1.4a). There are also studies that attempt to modify the scaling law to account for the discrepancy of experiment or simulation from the prediction [97, 109, 168, 172].

It is therefore remarkable that the comparison of the stiffness obtained by the experiment in this work and MD simulations in Ref. [99] revealed a significant deviation from the Gibson-

Ashby scaling. This, thereby, firmly underlies that the mechanical behavior of nanoporous metal is weakly linked to one of conventional foams.

From the data in Fig. 4.4 and 4.8, it follows that the elastic modulus of np-Au seems to depend on the ligament size, tending to increase when the structural size decreases. This finding supports one of the discussed trends in Section 1.2.1, namely the stiffening behavior of small-scale material systems. Even though np-Au displays the enhanced stiffness for the smaller ligaments, it is still much more compliant than the Gibson-Ashby model predicts. It can be speculated that this contradiction rests on the geometry of the structural elements of the material and their surface condition (curvature, roughness, surface defects, etc.). Additionally, one can expect the modified elastic properties in nanoporous metal due to action of surface stress, nonlinear bulk or surface excess elasticity effects as has been reviewed in Section 2.2.1. Such effects become especially significant when the surface-to-volume ratio of the nanoscale ligaments increases. Because of the reduced coordination of surface atoms, a surface can posses different elastic modulus than in the bulk, and for nanoporous network with large surface area this can potentially imply altering the overall elastic response by the the local elastic moduli. Therefore, it is necessary to have a theory which would consider the effective elastic property of np-metal taking into account the free surface effects together with the structural disorder, and the nonuniform distributions of ligament sizes. Presently available models that include the surface elasticity aspect [104–106], however, disagree on the magnitude of the contribution. Besides that, there is even a lack of the data on the surface elastic moduli used to describe the elastic response of a single surface (Section 2.2.1).

5.1.3 Nonlinear unloading response

Figure 4.4 shows hysteretic behavior in the unloading/loading curves of the compression test. This inelatic response indicates a partial recovery of the deformation during unloading and is similar to the Bauschinger effect in conventional engineering materials. The phenomena is often observed in nanocrystalline materials [186–188], where it is linked to structural inhomogeneity [189] and to an asymmetric distribution of local yield stresses [190]. One can naturally expect the same mechanisms also for nanoporous metals, in which microstructural heterogeneity originates form of distributions in shape, size, and orientation of the ligaments. Such structural disorder might cause local yielding of the ligaments over a wide range of externally applied stresses and explains the occurrence of the early deviation from linear elastic behavior during load/unload resulting in the development of a large hysteresis.

5.2 Effect of electrode potential on stiffness

5.2.1 Phenomenological description of surface effects on elasticity. Electro-elastic coupling parameter

The *in situ* DMA data presented in Chapter 4 advertise important implications for the surface excess elasticity in elastic behavior of nanomaterials. As the electrochemical modification affects np-Au exclusively at its surface, the changes in the effective elastic response unambiguously testify to the changes in local stiffness at surfaces of the material.

The importance of this observation is based on its nature as a reversible modulation of the elastic modulus of a given sample. During variation of the effective stiffness the geometry of the microstructure remains unchanged. This eliminates artifacts from erroneous or inaccurate reference data, which can emerge when surface contributions are to be derived from absolute values of the elastic response of a nanomaterial or nanoscale object. In such instances, precise data for geometric dimensions, for crystallographic orientation and for the set of elastic coefficients of the material are crucial and not in all instances available. The approach developed here avoids this complication.

The experiments designed in this work propose a new methodology: rather than seeking absolute values of the surface excess elastic modulus, they suggests to explore the reversible changes of elastic response of a high surface area material as its surface state is *cyclically* varied. This has parallels to studies of the surface stress, where experimental reports on direct measurement of its absolute values are scarce [6] but where the variation during adsorption from gas phase and during electrosorption or capacitive charging in electrolyte has been measured with high accuracy and sensitivity [113] (Sections 2.1.2 and 2.3.2). The surface stress is essentially sensitive to the presence of adsorbates, due to the different bonding configuration and physical properties of surfaces with adsorbates as compared to clean surfaces. The precise control of the surface states at a metal-electrolyte interface that can be attained through electric potentials (Section 2.3.1) is exploited in the experimental approach here. In the following, consider an influence of the surface state on a surface excess elastic constant from the phenomenological point of view.

As has been shown in Section 2.3.3 the impact of the surface on the energetics of elastic deformation is described by the surface free energy function $\psi(q, e)$ with two state variables e, the relative change in area by elastic strain, and q, the surface electric charge density. The energy-conjugate variables to e and q are the scalar surface stress, f, and the electrode potential, E, so that $\mathrm{d}\psi = E\mathrm{d}q + f\mathrm{d}e$. The restriction to the scalar e and f and neglecting shear components is appropriate for crystal surfaces that have a threefold (or greater) axis of rotational symmetry [138], such as low-index surfaces of a face-centered cubic lattice in the limit of small strain. The associated surface excess elastic constant is then

$$\mathbb{C} = \frac{\partial^2 \psi}{\partial e^2} = \left.\frac{\mathrm{d}f}{\mathrm{d}e}\right|_q . \tag{5.1}$$

Nevertheless, description of even isotropic surface in the unstrained reference state requires an additional excess elastic constant that characterizes evolution of surface stress anisotropy in response to in-plane shear [126, 191]. Yet reports on surface stress do not yield any experimental signature that could be linked to its anisotropy, practically relating to the scalar f, whereas surface stress anisotropy has only been documented in few exceptional cases (such as Ref. [192] for Si). Hence excess shear stiffness can be ignored in the consideration here, and one will focus on area strain and the associated parameters $f$and $\mathbb{C}$ alone.

There are other two derivatives of ψ that are relevant for the electrode mechanics. One is the electrocapillary coupling coefficient ς [112], which describes variation of f upon charging of the surface, $\varsigma = \partial^2\psi/\partial e\partial q = (\mathrm{d}f/\mathrm{d}q)|_e$ (Section 2.3.2). Another is an *electro-elastic coupling parameter*, λ, that has been similarly introduced in this work to describe excess elastic modulus variation with the superficial charge:

$$\lambda = \frac{\partial^3 \psi}{\partial e^2 \partial q} = \left.\frac{\mathrm{d}\mathbb{C}}{\mathrm{d}q}\right|_e . \tag{5.2}$$

As has been suggested by Miller and Shenoy [25], the significance of the surface excess elasticity contribution to the effective elastic behavior of nanostructures may be parameterized by a simple geometric measure that sets the dimensions of the nanoscale object at which the free surface effect becomes significant. In an attempt at illustrating the magnitude of $\mathbb{C}$, that concept is adopted here as well. To this purpose, consider the straining of an elastically isotropic slab by in-plane forces F_1 and F_2 attached to its two opposite cross-sectional faces as shown in Fig. 5.2. The slab represents a square patch of thin film of edge length l and thickness t, where t defines the structural length scale. In the absence of the effect of surfaces, simple linear elasticity of isotropic media relates the area strain e to the sum of the forces, $F = F_1 + F_2$ via $F = ltBe$, where B denotes the biaxial modulus, $B = Y/(1-\nu)$ with Y, Young's modulus and ν, Poisson's ratio of the bulk of the film. If surface excess elasticity is accounted for, and e is measured with respect to a reference state of the slab at $F = 0$, then

$$F = ltBe + 2l\mathbb{C}e\,, \tag{5.3}$$

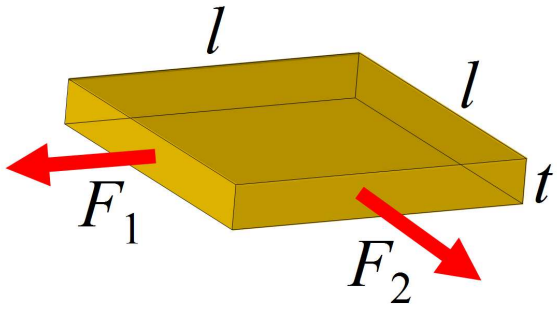

Figure 5.2. Schematic geometry of a cuboid slab, representing a patch of thin film of area $l \times l$ and thickness t, loaded on two opposite cross-sectional faces by the forces F_1 and F_2 [169].

where the extra term takes into account the change in the surface stress that acts along the edges bounding the upper and lower surfaces (hence the factor 2). One may equivalently rewrite Eq. (5.3) as

$$F = l(t + 2\tau)Be\,, \tag{5.4}$$

where τ is defined as the ratio of the surface elastic constant of the bounding surfaces of the slab and the elastic constant of its bulk material

$$\tau = \mathbb{C}/B\,. \tag{5.5}$$

In such representation through Eq. (5.5), τ simply parametrizes the surface excess elastic constant $\mathbb{C}$. Equation (5.4) suggests an intuitive geometric meaning of the parameter τ. If the surface elastic constant of the film material is positive (for $\mathbb{C} > 0$), the effective elastic response of the film of thickness t (and in the presence of the surface effect) would correspond to the response of the thicker equivalent film that has no capillarity effect. And conversely, the negative surface elastic constant ($\mathbb{C} < 0$) would imply the effective elastic response of the thinner equivalent film. The argument can be also applied to other geometries, so that by using the parameter τ, one replaces the surface excess elastic constant with an apparent excess thickness that would instead of $\mathbb{C}$ characterize the significance of the surface contribution to the elastic behavior of small structures. Below, this simple consideration will be profitably applied for interpretation of the results of *in situ* DMA experiments from Chapter 4. It should be emphasized that the apparent excess thickness τ is solely a formal parametrization of the excess stiffness; τ is not related to the actual inward or outward relaxation at the surface or to the physical specific excess volume, which are defined separately (see Refs. [112, 193]).

Based on atomistic simulation using the embedded atom method-potentials (EAM), the value of τ has been estimated for the case of Al and Si surfaces in the order of −100 pm [25]. For gold, with isotropic (polycrystalline) elastic constants $Y = 78$ GPa and $\nu = 0.44$, Eq. (5.5) would associate that τ-value with $\mathbb{C} = -14$ N/m.

5.2.2 Estimation of changes in surface excess elastic constant

The phenomenological description of surface excess elasticity above has introduced the parameters ς and λ, which quantify, respectively, the charge-dependencies of the surface stress and of the surface excess elastic constant $\mathbb{C}$. The observations on potential-induced strain in Fig. 4.12 and 4.13 (Chapter 4) confirm the established finding that ς of clean Au surfaces is of same (negative) sign for capacitive charging and for oxygen species electrosorption [9, 70] (except the OH-adsorption region in 0.5 M H_2SO_4 +10^{-3} M NaBr solution). By contrast, the data for $\Delta Y'$ vs. Q in Fig. 4.7c and f as well for $\Delta Y'/Y_0'$ vs. E in Fig. 4.12a, b, d and 4.13 imply that λ takes on different signs, negative for capacitive surface charging and positive during electrosorption of oxygen species.

To interpret the observation on the sign and establish an exact link between λ and the effective elasticity variation, ΔY^{eff}, one requires continuum theory that describes *i)* the elastic behavior of solid networks with realistic geometry and *ii)* the surface excess elasticity impact on networks with a nanoscale structure size. Although issue *i*) has become a subject of intense research recently and quite detailed models have been developed [97, 109], predictions with the necessary precision of much better than the magnitude of the effect here (2 – 8%) so far are unavailable. Issue *ii*) has been probed by computational studies, yet the examined model geometries are too simplified [105, 106] that do not approximate the real microstructure of np-Au. Besides, even the simpler problem of predicting the strain response to the surface stress is impaired with uncertainties of several 10% [171].

In view of the above concerns, an order-of-magnitude estimate of the change in $\mathbb{C}$ is proposed. The elastic deformation of low-density nanoporous solid, such as np-Au, is dominated by the bending of the struts or ligaments [109]. In other words, the ligaments can be treated as simple Bernoulli beams and one can apply Bernoulli beam theory [194], where the second moment of inertia of the ligaments provides the relevant geometry parameter for the bending stiffness, $I = {}^1\!/_4\pi r^4$ with r a characteristic ligament radius. Taking into account Eqs. (5.4) and (5.5), the change in excess elasticity may be represented by an apparent small variation in ligament radius. The latter may then be identified with a change in the apparent surface specific excess volume τ. One can thus take $\delta I = (\mathrm{d}I/\mathrm{d}r)\delta\tau$, which implies that the relative change in bending stiffness agrees with

$$\frac{\delta I}{I} = \frac{4}{r}\delta\tau, \tag{5.6}$$

By supposing linear elasticity, the relative stiffness variation of the ligament as the representative and single constitutive structural element of the nanoporous network concurs with the relative variation of the macroscopic stiffness. Therefore, the relative changes in Y^{eff} by 7.8 and 1.6% observed, for instance, in 1 M $HClO_4$ in the two potential regions – OH^- electrosorption and capacitive charging (Fig. 4.7) – correspond to numerically identical relative changes in I. In this case, by inserting $r \approx 22$ nm (half the ligament diameter) into Eq. (5.6), one obtains for $\delta\tau$ the values 430 and 88 pm. They are comparable to the absolute value of τ in the order of 100 pm as estimated in Ref. [25].

Based on the derived estimates of $\delta\tau$ one can now assess the corresponding changes in the surface excess elastic constant. Since the estimate of τ uses the relative change in bending stiffness, it is independent of the assumptions on the nature of $\mathbb{C}$. Then, as discussed in Section 5.2.1, one might assume, somewhat arbitrarily, that the excess shear stiffness may be ignored and the excess elasticity is entirely dominated by the constant $\mathbb{C}$. Equation (5.5) thus yields changes in $\mathbb{C}$ in the *in situ* DMA experiments by 60 N/m (electrosorption) and 12 N/m (capacitive charging). For comparison, as follows from the calculations using the embedded-atom-potential approximation, the uniaxial in-plane surface elastic constant of Au(111) is −8.0 N/m [38]. Hence, the estimated changes in $\mathbb{C}$ turn up to be comparable or much larger than the reported absolute values of the surface excess elastic constant evaluated for gold clean surfaces. This emphasizes the significance of the surface state (adsorbate coverage or electric polarization) for the surface excess elasticity.

It should be also noted that $\delta\tau$ value found during OH-adsorption on gold surface emerges to scale with the lattice parameter of gold (~ 408 pm) or almost equals to its two dense-packed layers (the spacing between dense-packed layers is $d_{111} = 235$ pm). In other words, in order to account for the effective stiffening of np-Au samples during adsorption that involves 1 atomic monolayer of OH by the hypothetical process of simply adding extra Au on the surface, one would need to add a layer with the thickness of more than a full lattice parameter or nearly two dense-packed layers of Au. These are enormous effects, if to compare to the actual change in excess volume during capacitive charging of Au in electrolyte, which is in the order of only 1 pm [195, 196].

In a more comprehensive sense, the variation of the surface excess elasticity may be qualitatively understood as the consequence of reversible changes of the bonding strength between the surface atoms. For the case of capacitive charging, the stiffening of a negatively charged surface is consistent with a simple model in which excess electrons will flow into the space between the atoms of the surface layer [197], and as a result, enhancing the attractive interaction between them. This would be expected to increase both the surface stress and the surface excess elastic modulus.

The expectation agrees with the observations for all studied electrolytes here, apart 0.5 M H_2SO_4, where enhancement of the stiffness has been found to occur at the positively charged surface, in the capacitive regime of the voltammogram (Fig. 4.12c). The argument also fails to interpret the stiffening in the case of the electrosorption of oxygen species; there the metal surface is expected to be depleted of electrons due to the strong electron-withdrawing character of the oxygen. Alternatively, the bond forces occurred between the adsorbed OH and Au might contribute to the stiffening of the surface, yet there are good arguments for ignoring such metal-adsorbate interaction and attributing the impact of anion adsorption on noble metal electrode surfaces to the changes in the bonding within the metal atoms only [113, 136, 198]. So far, the state of the art on the capillarity of solids does not to afford a simple explanation for the considerable stiffening of the Au surface during oxygen species electrosorption.

A comparison of the impact of anion adsorption on the effective elastic modulus as shown in Fig. 4.14 and Tab. 4.2 indicates that the potential-induced stiffening gets smaller in the presence of the halides. This observation correlates with the behavior of the surface stress-charge coupling parameter ς that also depends on type of anion, where a noticeably lower ς has been found during chloride and bromide adsorption on Au(111) as compared to weakly binding perchlorate [113]. In that case, the value of the electrocapillary coupling ς is believed to reflect a degree of charge transfer between the adsorbed species and the metal surface, which consequently can lead to changes in metal-metal surface bonds. This therefore allows to assume a strong link between the adsorbate-induced bonding rearrangement at the surface and the elastic modulus.

The oxygen adsorption also has a remarkable effect on the loss modulus, leading to its almost complete suppression (Fig. 4.6b). This observation would be consistent with a picture wherein surface defects (step edges, kinks) rearrange in response to a variation of the heterogeneous strain fields on the surface. The uptake of oxygen by a nominally clean metal surface might result in quenching the rearrangement along with suppressing the mobility of the gold surface atoms. The increasing of the dissipative loss for the clean surface might be caused by the rearrangement of adatoms in varying strain fields at the surface. This agrees well with the reported trend for a preferable decoration of strain fields by adatoms, when the latter are selectively adsorbed on a surface depending on local variations of surface strain [199].

5.3 Effect of electrode potential on flow stress

5.3.1 Phenomenological description of surface effects on plasticity. Coupling of capillary parameters to compression

The *in situ* mechanical tests in the aqueous electrolytes reported in Chapter 4 show that both *surface capacitive charging* and *specific adsorption* considerably influence flow stress of np-Au. At the same time its potential-induced changes, $\Delta\sigma/\Delta E$, scale with the ligament size analogously to the overall flow stress σ. Remarkably, when normalized by the actual value of the compressive stress, the flow stress-electrode potential coupling parameter $\Delta\sigma/\Delta E$ measured in the presence of the weakly adsorbed anions ClO_4^- and SO_4^{2-} exhibits no size-dependance (Fig. 4.17). It is indeed a very extraordinary finding that implies an important

link between phenomena responsible for strengthening by electric potentials and strengthening by structural size.

While theory and simulations acknowledge a prominent role of capillary forces in plastic deformation of nanomaterials ([200] and references therein), experimental studies are not readily able to recognize or separate their significance from other possible contributions. As has been briefly reviewed in Chapter 1, the well-documented size-dependent strength entails numerous mechanisms with no firmly established agreement at this point. In this respect, electrochemical tuning of surface state during mechanical testing implemented in this study emerges as a promising approach. Owing to predictable changes of capillary forces as a function of the electrode potential for metal electrodes (Section 2.3.2), control of the electrical potential along with plastic straining is likely to provide signatures of capillary phenomena involved. In view of lack of appropriate theory that would describe plastic deformation under the applied electric potentials, the *hypothetical mechanisms* as the most relevant for the coupling between the surface state and flow stress are first examined here.

For simplicity, a nanoporous solid is envisioned as a network of identical wires with a length l, circular cross-section and uniform radius r. The surface of each wire is assumed to have an isotropic surface tension and surface stress, and the properties of the wires core are also assumed to be isotropic. A small variation in a relevant surface parameter and the corresponding changes of flow stress of the single wire are denoted by δ. The influence of possible surface parameters are discussed below.

Surface tension

Consider the surface tension γ as a determining factor in controlling the plastic flow in the wire. From the fact that a body tends to lower its free energy by decreasing its surface it follows that γ, which represents the free energy per unit area (Eq. 2.1, Chapter 2), favors *contraction or compression*. This situation is well-illustrated by the zero creep experiment (Section 2.1.2), where the applied stress balances the contracting stress due to surface tension. According to Eq. (2.4) in the underformed state this stress scales with the radius as γ/r, thus attaining substantially large values $0.1 - 1$ GPa for nanoscale ligaments. During plastic straining the wire this stress performs the work of deformation together with the external stress and leads to the reduction of the flow stress, $\delta\sigma$. This is expressed as

$$\delta\sigma \sim -\frac{\delta\gamma}{r}. \tag{5.7}$$

Hence, any increase of the surface tension followed by the subsequent reduction of the surface area will result in a decrease of $\delta\sigma$. The expression (5.7) is similar to the Laplace pressure in a fluid, which is related to its surface tension γ^{F} and the mean curvature by the Young-Laplace equation ($\Delta P = \gamma^{\mathrm{F}}/R$ for an infinitely long cylinder of radius R).

Slip step energy

Another aspect that may point to the contribution of the surface tension to the yield stress is an existence of *steps* at crystal surfaces and their important role for plasticity in small-scale systems [201, 202].

Consider a single-crystalline nanowire under mechanical load. Its plastic flow can be realized via glide of the preexisting (or just nucleated) dislocation on a cross-sectional slip plane. Then, as the load increases, the dislocation moves to another side of the wire and egress at its free surface, producing a step, a plastic shear by one Burgers vector. The free surface energy related to the formation of the free-surface step owing to plastic shear across the nanoligament cross-section is given by $\gamma_{\mathrm{s}} A_{\mathrm{step}}$, where γ_{s} is the specific energy of the newly formed free surface, and A_{step} is the extra surface area of the step. The surface energy of

the step γ_s opposes a cross-gliding of the dislocation at the surface of the crystal [203]. Since surface cross-glide can lead to dislocation multiplication [204], an increase in γ_s would resist moving of dislocations, promoting increase of the flow stress, i.e.

$$\delta\sigma \sim \delta\gamma_s. \tag{5.8}$$

Surface stress

In the situation where the surface stress f is the only parameter that governs resistance to plastic flow, the simplified picture of deforming the wire would be the following.

For clean metal surfaces, f is usually tensile and the surface tends to shrink (Section 2.1.1). As follows from the surface equilibrium equation (Eq. 2.10), this surface stress needs to be balanced by bulk stress in the ligament core so that the initial prestress exist underneath the surface. The shrinkage (or relaxation) lowers the free energy density of the surface ψ but enhances the free energy density of the bulk Ψ^B by introducing the strain energy in the core of the wire. The applied plastic deformation further reduces ψ through decrease of the surface area (and subsequent decrease of the relaxation) and introduces an additional, higher strain energy density in the bulk. The latter, together with the primary stored strain energy, is able to compensate the reduction of the surface energy, thus impeding the compression. Therefore, the action of the surface stress suppresses the plastic deformation in compression and one can write [205]

$$\delta\sigma \sim \frac{\delta f}{r^2}, \tag{5.9}$$

i.e. an increase in the surface stress implies the higher flow stress.

Surface excess elasticity

A local stiffening or weakening of the surface predicted in theory (Sections 1.2.1 and 2.2.1) alone makes the surface excess elastic modulus $\mathbb{C}$ a feasible factor to influence the plastic behavior of a nanoscale solid. Because of different elastic modulus of the surface compare to the bulk, elastic interaction of dislocations with the near-surface region can be much affected. A stiffer or softer surface can act like a film attached to the bulk that mechanically restricts or promotes the motion of dislocations.

Dislocation theory predicts that if a dislocation approaches a clean surface (or a surface with a modulus that is less than that of the crystal core), the dislocation will experience an attraction (an image force) tending to draw it from the crystal [206]. Conversely, the dislocation will feel a repulsion that will draw it from the surface. Thus, when the modulus of the surface exceeds that one of the bulk, an external applied force must overcome the repulsive force (neglecting all other factors) in order to deform the crystal. The stiff surface acts as a barrier or resistance to dislocation emergence, and one might expect to find a dislocation accumulation just under the surface [207]. The strengthening should be then a systematic function of the modulus of the surface, $\mathbb{C}$, or

$$\delta\sigma \sim \delta\mathbb{C}. \tag{5.10}$$

"Adsorption locking"

If the deformation of the wire is carried out in a fluid electrolyte, the superficial free energy density ψ can depend on amount of adsorbing species at the surface [9], which is described by the superficial excess Γ. These species are likely to interact with dislocations at the surface, influencing their multiplication during stressing or egression from the surface. The mechanism of restriction the dislocation motion at surface by chemisorbed adsorbates has been originally suggested by Westwood [53] and was termed *"adsorption locking"*.

It is well-know from studies on electrodes that the adsorption of species preferably occurs at special active sites [132]. Such sites, could be kinks or egression points of dislocation lines of bulk dislocations at the surface, both are frequently observed at metal surfaces [131]. The adsorbates (especially those that are strongly bonded to the surface, Section 2.3.1) that surround the dislocation endpoints can naturally lead to their pinning. Subsequently, this will affect yield and flow behavior. Hence, a dominant effect of the specific adsorption would imply a pronounced scaling of the flow stress σ with the Gibbsian interfacial excess Γ

$$\delta\sigma \sim \delta\Gamma. \tag{5.11}$$

Trends for coupling capillary parameters to compression

Figure 5.3e-h illustrates the trends for the flow stress-electrode potential response $\sigma_0^{-1}(\Delta\sigma/\Delta E)$ based on the discussed above hypotheses. The predictions take into account the variation of each surface parameter γ, f, $\mathbb{C}$, and Γ as a function of the electrode potential E in aqueous electrolytes with non-specifically adsorbing ClO_4^- anion (Fig.5.3a-d) as deducted from *in situ* dilatometry and DMA measurements for np-Au in this work. In accordance with these data

γ: the surface tension passes through a maximum near the potential of zero charge (*pzc*), being compatible with the parabolic shape of the electrocapillary curve (Section 2.3.2). In view of Eq. (5.7), the increase $\Delta\gamma$ up to the *pzc* would entail lowering of the strength in compression. After the *pzc* the opposite behavior would be observed, meaning that γ predicts a sign inversion in the response of the flow stress near the *pzc* (Fig. 5.3e). The argument is consistent with implications of the earlier creep experiments on Au (macroscopic wires) performed in an electrolyte under electric polarization in tension [59]. The study reports a minimum in plastic strain rate near the existence of the electrocapillary maximum of γ and suggests that reduction of the surface tension yields acceleration of the plastic flow at the cathodic and anodic end. In other words, the surface tension promotes compression but impedes tension.

f: the surface stress monotonically decreases in the whole range of the studied electrode potentials. The reduction of Δf would require increasing of the stresses in the bulk, which in turn would continuously counteract an action of the external compressive stress. The mutual compensation between the stresses in the bulk and surface regions might also lead to the absence of the net stress at a dislocation line pinned in the interior of the wire. This then implies no changes in the flow stress behavior in the whole potential window (Fig. 5.3f).

$\mathbb{C}$: the surface excess elastic modulus falls in the capacitive region of the CV but rises upon oxygen electrosorption. The softening of the surface observed at the lesser potentials would promote weakening of the material and the reduction of the flow stress. An inversion of the flow stress-electrode potential response would then occur in the potential interval where the OH-adsorption processes dominates (Fig. 5.3g).

Γ: the Gibbs excess (surface concentration of adsorbed species) increases slowly at more negative potentials, while growing steeply at potentials that corresponds to the OH-layer formation on the surface. Following the "adsorption locking" concept, the gradual increase of the adsorbates on the surface would induce a consecutive pinning of the dislocations and, as a result, would lead to a continuous enlargement of the flow stress (Fig. 5.3h).

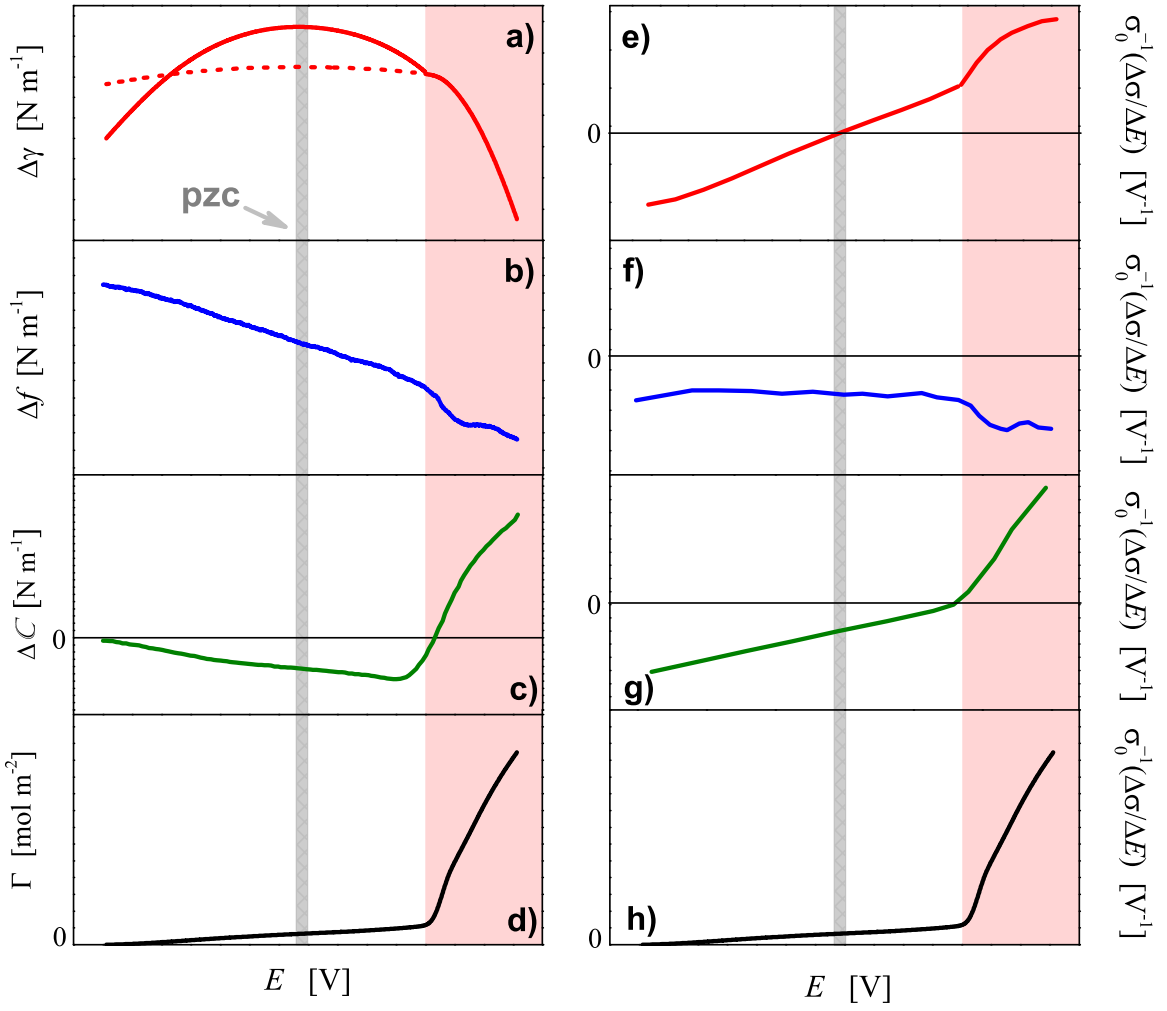

Figure 5.3. Variation of different surface parameters with the applied electrode potential E for np-Au in $HClO_4$ as measured by *in situ* dilatometry and DMA experiments: (a) surface tension γ (red solid line, data were enlarged in the capacitive regime for better readability), (b) surface stress f, (c) surface excess elastic modulus $\mathbb{C}$, (d) superficial excess Γ (scales with the charge accumulated at the metal-electrolyte interface [108]). Note an excellent agreement of γ and f with results for a planar Au electrode in an aqueous NaF solution (see for more details Section 2.3.2). (e-h) Prediction of the flow stress-electrode potential response $\sigma_0^{-1}(\Delta\sigma/\Delta E)$ in compression based on the proposed hypotheses in Section 5.3.1 (schematic). Shaded area represents a region of OH-adsorption. A range of the zero charge potential (pzc) is indicated.

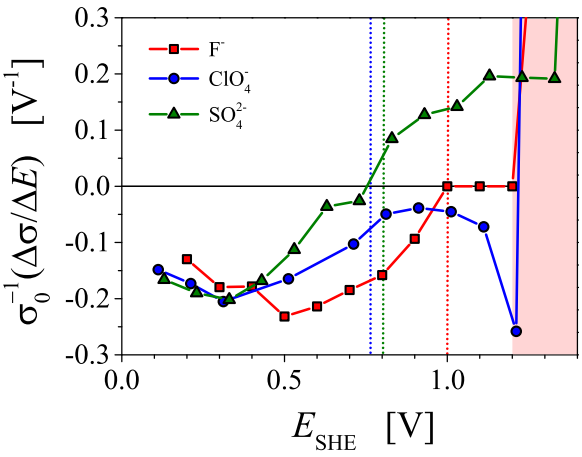

Figure 5.4. Flow stress-electrode potential (normalized) coupling parameter $\sigma_0^{-1}(\Delta\sigma/\Delta E)$ of np-Au (L_D = 40 nm) experimentally obtained in the solutions with weakly adsorbed anions of F^-, ClO_4^-, and SO_4^{2-}. Focus on the capacitive double layer charging regime. Shaded area represents a region of OH-adsorption. The zero charge potential of np-Au (pzc) measured by the immersion method is marked by dotted lines, where a color code for each anion corresponds to one in the legend.

5.3.2 Comparison of the experimental results with theoretical predictions

Figure 5.4 presents the experimental results obtained in the non-specifically adsorbing aqueous electrolytes, focusing on the potentials of the capacitive regime. The comparative analysis of these data and the proposed theoretical predictions summarized in Fig. 5.3(e-h) allow to make the following conclusions about a role of the different processes at the surface on strength of np-Au.

Surface tension

The prediction that rests on the surface tension as relevant parameter that controls the plasticity implies the sign inversion of the normalized coupling parameter $\sigma_0^{-1}(\Delta\sigma/\Delta E)$ at the *pzc*. In the experiment such behavior is observed during compression of np-Au in sulfuric acid and sodium fluoride. Nevertheless, $\sigma_0^{-1}(\Delta\sigma/\Delta E)$ in the presence of other weakly adsorbing ion ClO_4^- undergoes significant changes in the vicinity of the *pzc* as well, precisely following the prediction at the negative voltages. It can therefore be assumed that the mechanism based on the potential-dependent surface tension is not solely involved in the deforming of the np-metal. In general, the outcomes of the hypothesis is compatible with the experimental observations.

Slip step energy

The hypothesis about an impact of the slip step on the surface has exactly opposite prediction to the previous one with no verification by the experiments. Hence, this factor can be excluded from the consideration.

Surface stress

In this case, there is no clear consensus between the hypothesis – which considered surface stress as major parameter in governing the plastic flow in np-Au – and the results of the *in situ* testing (with the exception of very negative potentials). This is in the line with the previous experimental findings revealed by the similar *in situ* measurements on np-Au. Upon OH-electrosorption a numerical estimation of the surface stress f contribution to the plastic

deformation indicates its negligible impact, appearing to be unsuccessful in accounting for the experimentally observed changes in the strength [15]. Additionally, that study points out that in the capacitive region the changes in the flow and surface stress are also not consistent.

"Adsorption locking"

Within "adsorption locking" scenario it is natural to expect increase in yield stress due to OH-adsorption. There is experimental evidence in the literature that prove this hypothesis. For instance, a strong pinning effect of hydroxyl ions on surface dislocations has been confirmed by creep tests of pure Au [60]. Similar but smaller effect has been reported by analogous experiments on Au in the presence of anions with different adsorption strength, where it has been concluded that the dislocation pinning strength of the adsorbed anions obeys the following sequence [208]:

$$\mathrm{OH} \gg \mathrm{ClO_4^-} > \mathrm{SO_4^{2-}} > \mathrm{Cl^-} = \mathrm{I^-} = 0, \tag{5.12}$$

Yet the experimental results for the $\sigma_0^{-1}(\Delta\sigma/\Delta E)$ trend during anion adsorption, including weakly (F^-, ClO_4^-, SO_4^{2-}) as well as strongly (Cl^-, Br^-) adsorbing species are unable to support relevance of the "adsorption locking" mechanism. A study of halides adsorption Cl^-, Br^-, and I^- on Au(111) electrode surface suggests an increase of the surface concentrations already at negative potentials, which then attains a quasi plateau at more positive values [108]. This "early" adsorption explains absence of any changes in the coupling parameter $\sigma_0^{-1}(\Delta\sigma/\Delta E)$ upon adsorption of the two halides (Cl^- and Br^-) at the negative potentials. As a result, this hinders an analysis of the surface concentration or Gibbs excess Γ impact on plasticity of nanoporous metal.

Surface excess elasticity

In the specific case of $HClO_4$ electrolyte, the empirical data support the trend governed by the surface excess elasticity mechanism. Moreover, from the data in Fig. 4.14 and 4.18 (Chapter 4), it is apparent that the potential-induced changes in the effective elastic modulus and flow stress of np-Au correlate with each other. Weakening (decrease of the stiffness) observed within the capacitive regime coincides with softening (decrease of the strength) in the same range of the potentials. The same behavior applies to the region where OH-adsorption takes place. However, in the case of H_2SO_4 electrolyte, no weakening of np-Au occurs during the capacitive processes, whereas the strength decreases there (up to the evaluated *pzc*, in the middle of the double-layer regime). This makes it difficult to explain the plastic behavior of the high surface area material by the surface excess elasticity mechanism.

In principle, one can anticipate a decisive influence of the excess elastic moduli on dislocation behavior near a surface, which can be crucial for the deformation behavior of nanostructures. For instance, there are theoretical approaches that consider the elastic behavior of an edge and screw dislocation in a core-shell nanowire within the theory of surface elasticity [209, 210]. According to these studies, the surface with positive (negative) shear modulus causes an extra non-classical repelling (attracting) image force on the two types of the dislocations. This additional image force becomes more considerable when the dislocation approaches the surface and can change the nature of the equilibrium positions of the dislocations.

Overall, it can be concluded that the assessment of the different arguments in Section 5.3.2 based on the experimental data so far support one hypothesis, which predict a substantial impact of the surface tension on the plastic deformation of np-Au during compression. Although the influence of the "adsorption locking" mechanism can be clearly seen in the case the OH-electroadsorption regime, direct evidence of the correlation between the anions adsorption and the flow stress-electrode potential response $\sigma_0^{-1}(\Delta\sigma/\Delta E)$ is however lacking. Also, the surface

excess elasticity impact needs to be verified by systematic measurements. At the same time, the empirical observations rule out a contribution of the surface stress to the plastic behavior. Since a significant effect of the surface stress on yielding of nanostructures is suggested by most of the current theoretical investigations, this conclusion therefore is remarkable.

Chapter 6

Summary and Outlook

6.1 Summary

The experimental findings of this study provide a new insight into the impact of the local surface properties on the overall mechanical response of bulk high-surface area materials. As a model nanomaterial nanoporous Au (np-Au) has been employed in the experiments. Due to its remarkable morphology – the homogeneous network of nanoligaments interpenetrated by an open pore space – it offers studying not only the size-dependent mechanical properties, but also the effects of chemical or electrochemical environment on the mechanical performance.

In the present thesis work, mechanical tests of macroscopic bulk np-Au samples were designed to probe the response of effective stiffness and plastic flow to the surface state. A key approach rested on performing deformation experiments in electrolyte *in situ* under potential control. In fact, when the pores of nanoporous metal are imbibed with electrolyte, the entire surface can be addressed through the electrode potential and the superficial charge density and/or adsorbate coverage controlled. In this way, the surface properties and, thereby, the effective macroscopic materials behavior can be tuned. The *in situ* experiments implemented in a dynamic mechanical analyzer (DMA) and mechanical testing device revealed novel findings in elastic and plastic deformation of the nanoporous metal that are summarized below.

6.1.1 Electrochemically-controlled stiffness and effects of surface excess elasticity

A central result of this thesis is the first demonstration that the effective elastic modulus of np-Au in contact with an electrolyte can be reversibly tuned by the electrode potential. The effective macroscopic stiffness underwent large reversible changes during cyclic variation of the surface state under potential control in aqueous electrolytes. It has been shown that adsorption of ≤ 1 atomic monolayer of oxygen species as well as a capacitively controlled excess of electrons at the surface stiffen the material while oxygen desorption/electron depletion enhance the compliance. The relative changes in macroscopic stiffness for the two processes reached $\sim 8\%$ and $\sim 2\%$, respectively.

Since the electrode potential affects exclusively the surface, these observations provide the first conclusive evidence for the impact of surface excess elasticity on the effective elastic response of nanostructures. They also show that this behavior is crucially dependent on the state of the surface, clean or adsorbate covered. The strong impact of small quantities of adsorbate may explain some of the discrepancies in earlier attempts to explore surface excess elasticity, in which the adsorbate coverage was not characterized.

To quantify the changes in the surface excess elasticity, $\mathbb{C}$, to variation of the surface charge, q, an electro-elastic coupling parameter, $\lambda = \mathrm{d}\mathbb{C}/\mathrm{d}q$, was introduced. Relative changes in the effective stiffness of up to 8% imply the variation of a surface excess elastic constant

in the order of 60 N/m, much larger than the absolute value of that constant deduced from previous atomistic simulation studies of clean surfaces.

As a direct consequence of the importance of surface elasticity, these findings also reveal a novel functionality of nanoporous metals, namely their *electrochemically tunable stiffness*. This supports the notion of modification of properties of nanometer-sized structures by means of electric signals [8, 11, 15].

Apart important establishing of electrochemically modulated elastic modulus, the work significantly contributes to studies of elastic response of "dry" np-Au, where there has been little discussion so far. The noticeable observation here is that np-Au exhibits high compliance that was observed for the first time using two independent experimental techniques: load-unload tests in a mechanical tensing machine and DMA.

6.1.2 Electrochemically-controlled strength and size effects in plasticity

In situ compression tests in electrolyte suggest a similar effect of the electrode potential on the flow stress, where the relative variations respectively for oxygen electrosorption and capacitive charging reached ~ 80% and ~ 6%. The study focuses on plastic deformation upon the processes at the ligament/electrolyte interface in aqueous electrolytes during its capacitive charging. In such a regime, an influence of two capillary forces – surface tension and surface stress – on mechanical properties is expected to be pronounced. Indeed, the experiments detected two reproducible and clear trends in variation of flow stress in aqueous solutions of $HClO_4$ and H_2SO_4. In case of the former the flow stress-electrode potential coupling parameter $\Delta\sigma/\Delta E$ as a function of the potential has a tendency to diminish near the point of zero charge whereas for the latter there is a different behavior prevails with $\Delta\sigma/\Delta E$ inverting its sign to positive values. Comparative analysis of these experimental results with the proposed hypothesis about the impact of different surface parameters on the plastic deformation enables to conclude that surface stress is not the dominant factor in controlling the plasticity of np-Au. Instead, the analysis points towards surface tension as relevant parameter. This is contrary to theoretical studies where the influence of surface stress on strength of nanowires is considered to be decisive.

Another important finding emerged from the work is that the potential-induced flow stress variations in np-Au depend on the structural size in the same way as the flow stress. This allows to assume the same mechanism for the size-dependent strength as for one modulated by the potential. Further research in this field would assist in identifying microscopic phenomena that govern the size-dependent mechanical behavior of nanostructures. The approach implemented in the thesis probes the mechanical properties while reversibly changing the surface state was proved to be promising in studying the size effects on crystal plasticity.

6.2 Outlook: Actuation of nanoporous Au under compressive load

The thesis reports two remarkable observations: effective elastic modulus and flow stress of np-Au infiltrated with aqueous solutions can be controlled by the electrode potential. Oxygen adsorption along with negative charging of the surface of the ligaments enlarge both the stiffness and strength while oxygen desorption/negative charging reduces the mechanical properties. The surface modification by exactly similar processes and in the same solutions leads also to another phenomena – the change of macroscopic dimensions. Np-metal expands during adsorption of oxygen and contracts when the oxygen layer is reduced, suggesting it for actuation applications [7].

Since the potential-induced variation of the three quantities – modulus of elasticity, flow stress, and length change – occurs in np-Au at the same time, it is of interest to study how

they correlate with each other. Investigation of impact of the externally applied mechanical stresses on the performance of np-Au as actuator could assist in understanding of this correlation. Furthermore, characterization the actuation properties under load is also important for practical applications.

An advantage of the *in situ* DMA technique is that changes in both – potential-induced length and effective modulus – can be monitored in one experiment simultaneously. Figure 6.1a shows a profile of the compressive stress measured in *in situ* DMA setup together with the change in the longitudinal sample length and the storage modulus during the OH-adsorption-desorption process. The response of the sample at 1-2 MPa – expansion at positive potential and shrinkage at negative – very well agrees with the previous reports on dilatometry of np-Au at almost zero force. A further enlargement of the applied stress up to 3 MPa causes a noticeable contraction of the actuation amplitude followed by its complete suppressing at 4 MPa. Surprisingly, that applying even a larger stress (5-6 MPa) induces an inversion of sign of the actuation: the sample shortens during adsorption of the OH-species and lengthens while retaining to the clean adsorbate-free state. It is remarkable that the actuation amplitude restores its initial behavior when the stresses are reduced again (although the absolutes values cannot be recovered since the sample undergoes irreversible plastic deformation and subsequent densification). In contrast, the predeformed sample (up to stresses much higher than were applied by the DMA) exhibits no sign-inversion and the actuation amplitude remains almost identical (Fig. 6.1b). It is necessary to emphasize that the amplitude of the storage modulus variation for both cases practically is the same. Thus, the electrically-induced strain does not depend on stiffness variation of the material. Since the capacitive processes during analogous experiment cause no sign-inversion of the length change even in the case of the non-predeformed sample, one can assume that the observation rests entirely on an impact of OH-electrosorption on the surface stress behavior under the external stresses. This observation is an intriguing one, which could be usefully explored in further research.

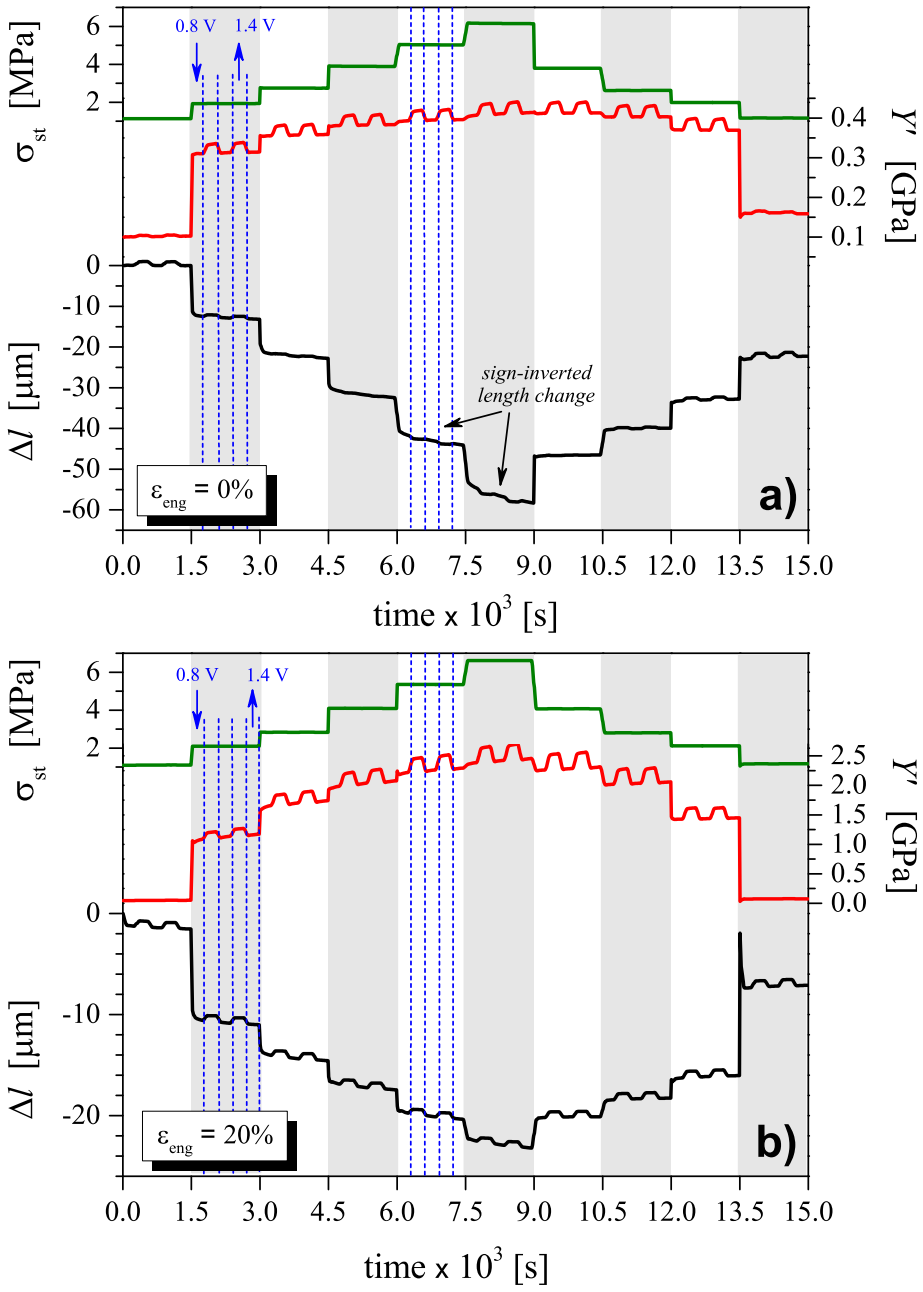

Figure 6.1. Variation of the length change of np-Au (L_D = 40 nm) under compressive stress and electrode potential in 1 M $HClO_4$ as measured by DMA: (a) as-prepared sample with no predeformation (ε_{eng} = 0), (b) predeformed sample (ε_{eng} = 0.20). A static stress σ_{st} profile (green, upper left ordinate), storage modulus Y' (red, upper right ordinate), length change Δl (black, lower left ordinate). Vertical blue dashed lines denote the applied voltage steps during each constant static force segment. Here, expansion and contraction of the sample induced by the potential steps correspond to a clean (0.8 V) and adsorbate-covered surface states (1.4 V vs. SHE).

References

[1] R.M. Latanision and J.T. Fourie, editors. *Surface effects in crystal plasticity*. Series E: Applied Science – No. 17. Noordhoff International Publishing, 1977.

[2] J. Biener, A. Wittstock, T. F. Baumann, J. Weissmüller, M. Bäumer, and A. V. Hamza. Surface chemistry in nanoscale materials. *Materials*, 2(4):2404–2428, 2009.

[3] R. Birringer, H. Gleiter, H.-P. Klein, and P. Marquardt. Nanocrystalline materials an approach to a novel solid structure with gas-like disorder? *Physics Letters A*, 102(8): 365–369, 1984.

[4] H. Lüth. *Solid surfaces, interfaces and thin films; 4th rev. and exp. ed.* Advanced texts in physics. Springer, Berlin, 2001.

[5] M. T. McDowell, A. M. Leach, and K. Gall. Bending and tensile deformation of metallic nanowires. *Modelling and Simulation in Materials Science and Engineering*, 16(4): 045003, 2008.

[6] D. Sander. Surface stress: Implications and measurements. *Current Opinion in Solid State & Materials Science*, 7(1):51–57, 2003.

[7] H.-J. Jin and J. Weissmüller. Bulk nanoporous metal for actuation. *Advanced Engineering Materials*, 12(8):714–723, 2010.

[8] H. Gleiter, J. Weissmüller, O. Wollersheim, and R. Würschum. Nanocrystalline materials: A way to solids with tunable electronic structures and properties? *Acta Materialia*, 49(4):737–745, 2001.

[9] J. Weissmüller. Electrocapillarity of solids and its impact on heterogeneous catalysis. In R.C. Alkire, L. Kibler, D.M. Kolb, and J. Lipkowski, editors, *Electrocatalysis: Theoretical Foundations and Model Experiments*, Advances in Electrochemical Science and Engineering, pages 163–219. Wiley VCH, Weinheim, Germany, 2013.

[10] H. Gleiter, Th. Schimmel, and H. Hahn. Nanostructured solids – From nano-glasses to quantum transistors. *Nano Today*, 9(1):17–68, 2014.

[11] J. Weissmüller, R. N. Viswanath, D. Kramer, P. Zimmer, R. Würschum, and H. Gleiter. Charge-induced reversible strain in a metal. *Science*, 300(5617):312–315, 2003.

[12] E.-M. Steyskal, M. Besenhard, S. Landgraf, Y. Zhong, J. Weissmüller, P. Pölt, M. Albu, and R. Würschum. Sign-inversion of charging-induced variation of electrical resistance of nanoporous platinum. *Journal of Applied Physics*, 112(7):073703, 2012.

[13] S. Ghosh. Charge-response of magnetization in nanoporous Pd-Ni alloys. *Journal of Magnetism and Magnetic Materials*, 323(5):552–556, 2011.

[14] Y. Xue, J. Markmann, H. Duan, J. Weissmüller, and P. Huber. Switchable imbibition in nanoporous gold. *Nature Communications*, 5, 2014.

[15] H.-J. Jin and J. Weissmüller. A material with electrically tunable strength and flow stress. *Science*, 332(6034):1179–1182, 2011.

[16] X.-L. Ye and H.-J. Jin. Electrochemical control of creep in nanoporous gold. *Applied Physics Letters*, 103(20):201912, 2013.

[17] H. Sadeghian, F. van Keulen, and H. Goosen. Mechanics of nanoelectromechanical systems: Bridging the gap between experiment and theory. *Advances in Micro/Nano Electromechanical Systems and Fabrication Technologies*, 2013.

[18] S. Cuenot, C. Fretigny, S. Demoustier-Champagne, and B. Nysten. Surface tension effect on the mechanical properties of nanomaterials measured by atomic force microscopy. *Physical Review B*, 69(16):165410, 2004.

[19] S. G. Nilsson, X. Borrisé, and L. Montelius. Size effect on Young's modulus of thin chromium cantilevers. *Applied Physics Letters*, 85(16):3555–3557, 2004.

[20] G. Y. Jing, H. L. Duan, X. M. Sun, Z. S. Zhang, J. Xu, Y. D. Li, J. X. Wang, and D. P. Yu. Surface effects on elastic properties of silver nanowires: Contact atomic-force microscopy. *Physical Review B*, 73(23):235409, 2006.

[21] P. Poncharal, Z.L. Wang, D. Ugarte, and W.A. De Heer. Electrostatic deflections and electromechanical resonances of carbon nanotubes. *Science*, 283(5407):1513–1516, 1999.

[22] Q.H. Jin, T. Li, Y.L. Wang, X.L. Gao, and F.F. Xu. Confirmation on the size-dependence of Young's modulus of single crystal silicon from the TEM tensile tests. In *Proceedings of IEEE Sensors*, pages 2530–2533, 2010.

[23] X. Li, T. Ono, Y. Wang, and M. Esashi. Ultrathin single-crystalline-silicon cantilever resonators: Fabrication technology and significant specimen size effect on Young's modulus. *Applied Physics Letters*, 83(15):3081–3083, 2003.

[24] L. G. Zhou and H. Huang. Are surfaces elastically softer or stiffer? *Applied Physics Letters*, 84(11):1940–1942, 2004.

[25] R. E. Miller and V. B. Shenoy. Size-dependent elastic properties of nanosized structural elements. *Nanotechnology*, 11(3):139–147, 2000.

[26] Diao J., K. Gall, and M. L. Dunn. Atomistic simulation of the structure and elastic properties of gold nanowires. *Journal of the Mechanics and Physics of Solids*, 52(9): 1935–1962, 2004.

[27] S. J. A. Koh and H. P. Lee. Molecular dynamics simulation of size and strain rate dependent mechanical response of fcc metallic nanowires. *Nanotechnology*, 17(14):3451, 2006.

[28] J. He and C. M. Lilley. Surface effect on the elastic behavior of static bending nanowires. *Nano Letters*, 8(7):1798–1802, 2008.

[29] F. Song, G. L. Huang, H. S. Park, and X. N. Liu. A continuum model for the mechanical behavior of nanowires including surface and surface-induced initial stresses. *International Journal of Solids and Structures*, 48(14-15):2154–2163, 2011.

[30] L. Y. Chen, G. Richter, J. P. Sullivan, and D. S. Gianola. Lattice anharmonicity in defect-free Pd nanowhiskers. *Physical Review Letters*, 109(12):125503, 2012.

[31] L. Qiao and X. Zheng. Effect of surface stress on the stiffness of micro/nanocantilevers: Nanowire elastic modulus measured by nano-scale tensile and vibrational techniques. *Journal of Applied Physics*, 113(1):013508, 2013.

[32] B. Wu, A. Heidelberg, and J.J. Boland. Mechanical properties of ultrahigh-strength gold nanowires. *Nature Materials*, 4(7):525–529, 2005.

[33] H. Petrova, J. Perez-Juste, Z. Zhang, J. Zhang, T. Kosel, and G. V. Hartland. Crystal structure dependence of the elastic constants of gold nanorods. *J. Mater. Chem.*, 16: 3957–3963, 2006.

[34] M. T. McDowell, A. M. Leach, and K. Gall. On the elastic modulus of metallic nanowires. *Nano Letters*, 8(11):3613–3618, 2008.

[35] R. Dingreville, J. Qu, and M. Cherkaoui. Surface free energy and its effect on the elastic behavior of nano-sized particles, wires and films. *Journal of the Mechanics and Physics of Solids*, 53(8):1827–1854, 2005.

[36] R. C. Cammarata. Surface and interface stress effects in thin films. *Progress in Surface Science*, 46(1):1–38, 1994.

[37] J. Diao, K. Gall, and M.L. Dunn. Surface-stress-induced phase transformation in metal nanowires. *Nature Materials*, 2(10):656–660, 2003.

[38] V. B. Shenoy. Atomistic calculations of elastic properties of metallic fcc crystal surfaces. *Physical Review B*, 71(9):11, 2005.

[39] H. S. Park, W. Cai, H. D. Espinosa, and H. Huang. Mechanics of crystalline nanowires. *MRS Bulletin*, 34:178–183, 3 2009.

[40] H. Liang, M. Upmanyu, and H. Huang. Size-dependent elasticity of nanowires: Nonlinear effects. *Physical Review B*, 71(24):241403, 2005.

[41] H. L. Duan, J. Wang, and B. L. Karihaloo. Theory of elasticity at the nanoscale. *Advances in Applied Mechanics*, 42:1–68, 2008.

[42] M.D. Uchic, D.M. Dimiduk, J.N. Florando, and W.D. Nix. Sample dimensions influence strength and crystal plasticity. *Science*, 305(5686):986–989, 2004.

[43] J. R. Greer, W. C. Oliver, and W. D. Nix. Size dependence of mechanical properties of gold at the micron scale in the absence of strain gradients. *Acta Materialia*, 53(6): 1821–1830, 2005.

[44] J. R. Greer and W. Nix. Nanoscale gold pillars strengthened through dislocation starvation. *Physical Review B*, 73:245410, 2006.

[45] C. A. Volkert and E. T. Lilleodden. Size effects in the deformation of sub-micron Au columns. *Philosophical Magazine*, 86(33-35):5567–5579, 2006.

[46] A. T. Jennings and J. R. Greer. Heterogeneous dislocation nucleation from surfaces and interfaces as governing plasticity mechanism in nanoscale metals. *Journal of Materials Research*, 26:2803–2814, 2011.

[47] D. Kiener and A.M. Minor. Source-controlled yield and hardening of Cu(100) studied by *in situ* transmission electron microscopy. *Acta Materialia*, 59(4):1328–1337, 2011.

[48] T. A. Parthasarathy, S. I. Rao, D. M. Dimiduk, M. D. Uchic, and D. R. Trinkle. Contribution to size effect of yield strength from the stochastics of dislocation source lengths in finite samples. *Scripta Materialia*, 56(4):313–316, 2007.

[49] Ch. R. Weinberger and W. Cai. Surface-controlled dislocation multiplication in metal micropillars. *Proceedings of the National Academy of Sciences*, 105(38):14304–14307, 2008.

[50] O. Kraft, P.A. Gruber, R. Mönig, and D. Weygand. Plasticity in confined dimensions. *Annual Review of Materials Research*, 40:293–317, 2010.

[51] P. Rehbinder. Verminderung der Ritzhärte bei Adsorption grenzflächenaktiver Stoffe. *Zeitschrift für Physik*, 72(3-4):191–205, 1931.

[52] E.D. Shchukin, L.A. Kochanova, and V.I. Savenko. On the mechanism of environment-induced plasticizing under contact interactions. In R.M. Latanision and R.J. Courtel, editors, *Advances in the mechanics and physics of surfaces*, volume 1, pages 111–152. Harwood Academic Publishing, 1981.

[53] A. R. C. Westwood. The Rebinder effect and the adsorption-locking of dislocations in lithium fluoride. *Philosophical Magazine*, 7(76):633–649, 1962.

[54] E.N.D.C. Andrade and R.F.Y. Randall. The Rehbinder effect. *Nature*, 164(4183):1127, 1949.

[55] M. Aponte-Roman, B. Mohanty, and A. B. Mann. Chemomechanical effects of self-assembled monolayers on gold films. *Acta Materialia*, 68(0):52–60, 2014.

[56] P. Rehbinder and E. Wenstrom. Electrocapillary effects in the reduction of the rigidity and hardness of metals. *Acta Physicochimica*, 19:36–50, 1944.

[57] R.M. Latanision, H.Jr. Opperhauser, and A.R.C. Westwood. Electrocapillarity and the microhardness of zinc monocrystal electrodes. In *Proceedings of the 5th International Congress on Metallic Corrosion, NACE, Houston, TX*, pages 111–114, 1974.

[58] D. N. Staicopolus. "Electrocapillary" studies on solid metals. *Journal of The Electrochemical Society*, 108(9):900–904, 1961.

[59] A. Pfützenreuter and G. Masing. Zunahme der Geschwindigkeit des Plastischen Fliessens von Metallen im Elektrolyten bei der Electrochemischen Polarisation. *Zeitschrift für Metallkunde*, 51(12):361–370, 1951.

[60] C. J. van der Wekken. The effect of cathodic polarization on the creep rate of gold. *Journal of The Electrochemical Society*, 129(4):706–711, 1982.

[61] R.M. Latanision, H. Opperhauser Jr., and A.R.C. Westwood. The influence of surface charge density on the fracture of zinc single crystal electrodes. *Scripta Metall.*, 12(5): 475–479, 1978.

[62] W. Klinkenberg, K. Lücke, and G. Masing. Die Beschleunigung des Fliessens von Metallen in Paraffinöl durch Polare Zusatze. *Zeitschrift für Metallkunde*, 44(8):362–369, 1953.

[63] S. G. Corcoran, S. R. Brankovic, N. Dimitrov, and K. Sieradzki. Nanoindentation of atomically modified surfaces. In *1997 MRS Fall Meeting – Symposium NN – Thin Films-Stresses & Mechanical Properties VII*, volume 505, pages 77–84, 1998.

[64] S. Eisner and A.A. Ottlyk. Electrocapillary effect on the modulus of elasticity of metals. *Nature*, 198(4887):1296, 1963.

[65] R.C. Newman, S.G. Corcoran, J. Erlebacher, M.J. Aziz, and K. Sieradzki. Alloy corrosion. *MRS Bulletin*, 24(7):24–28, 1999.

[66] J. Biener, A. V. Hamza, and A. M. Hodge. Deformation behavior of nanoporous metals. In F. Yang and J. C. M. Li, editors, *Micro and Nano Mechanical Testing of Materials and Devices*, chapter 6, pages 118–135. Springer US, 2008.

[67] J. Weissmüller, R. C. Newman, H.-J. Jin, A. M. Hodge, and J. W. Kysar. Nanoporous metals by alloy corrosion: Formation and mechanical properties. *MRS Bulletin*, 34: 577–586, 2009.

[68] R. Li and K. Sieradzki. Ductile-brittle transition in random porous Au. *Physical Review Letters*, 68(8):1168–1171, 1992.

[69] S. Parida, D. Kramer, C. A. Volkert, H. Rosner, J. Erlebacher, and J. Weissmüller. Volume change during the formation of nanoporous gold by dealloying. *Physical Review Letters*, 97(3):035504, 2006.

[70] H.-J. Jin, S. Parida, D. Kramer, and J. Weissmüller. Sign-inverted surface stress-charge response in nanoporous gold. *Surface Science*, 602(23):3588–3594, 2008.

[71] Y. Ding, Y.-J. Kim, and J. Erlebacher. Nanoporous gold leaf: "Ancient Technology"/Advanced Material. *Advanced Materials*, 16(21):1897–1900, 2004.

[72] H.-J. Jin, D. Kramer, Y. Ivanisenko, and J. Weissmüller. Macroscopically strong nanoporous Pt prepared by dealloying. *Advanced Engineering Materials*, 9(10):849–854, 2007.

[73] Z. Zhang, Y. Wang, Z. Qi, W. Zhang, J. Qin, and J. Frenzel. Generalized fabrication of nanoporous metals (Au, Pd, Pt, Ag, and Cu) through chemical dealloying. *The Journal of Physical Chemistry C*, 113(29):12629–12636, 2009.

[74] E. Detsi, Sellès M. S., Onck P. R., and J. Th. M. De Hosson. Nanoporous silver as electrochemical actuator. *Scripta Materialia*, 69(2):195–198, 2013.

[75] L. Sun, C.-L. Chien, and P. C. Searson. Fabrication of nanoporous nickel by electrochemical dealloying. *Chemistry of Materials*, 16(16):3125–3129, 2004.

[76] H.-J. Jin, X. L. Wang, S. Parida, K. Wang, M. Seo, and J. Weissmüller. Nanoporous Au-Pt alloys as large strain electrochemical actuators. *Nano Letters*, 10(1):187–194, 2010.

[77] X. Y. Lang, H. Guo, L. Y. Chen, A. Kudo, J. S. Yu, W. Zhang, A. Inoue, and M. W. Chen. Novel nanoporous Au-Pd alloy with high catalytic activity and excellent electrochemical stability. *The Journal of Physical Chemistry C*, 114(6):2600–2603, 2010.

[78] C. Xu, L. Wang, X. Mu, and Y. Ding. Nanoporous PtRu alloys for electrocatalysis. *Langmuir*, 26(10):7437–7443, 2010.

[79] H. Li, A. Misra, J. K. Baldwin, and S. T. Picraux. Synthesis and characterization of nanoporous Pt-Ni alloys. *Applied Physics Letters*, 95(20):201902, 2009.

[80] J. Biener, A. M. Hodge, A. V. Hamza, L. M. Hsiung, and J. H. Satcher. Nanoporous Au: A high yield strength material. *Journal of Applied Physics*, 97(2):024301, 2005.

[81] J. Biener, A. M. Hodge, J. R. Hayes, C. A. Volkert, L. A. Zepeda-Ruiz, A. V. Hamza, and F. F. Abraham. Size effects on the mechanical behavior of nanoporous Au. *Nano Letters*, 6(10):2379–2382, 2006.

[82] A. M. Hodge, J. R. Hayes, J. A. Caro, J. Biener, and A. V. Hamza. Characterization and mechanical behavior of nanoporous gold. *Advanced Engineering Materials*, 8(9): 853–857, 2006.

[83] A. M. Hodge, J. Biener, J. R. Hayes, P. M. Bythrow, C. A. Volkert, and A. V. Hamza. Scaling equation for yield strength of nanoporous open-cell foams. *Acta Materialia*, 55 (4):1343–1349, 2007.

[84] M. Hakamada and M. Mabuchi. Mechanical strength of nanoporous gold fabricated by dealloying. *Scripta Materialia*, 56(11):1003–1006, 2007.

[85] C. A. Volkert, E. T. Lilleodden, D. Kramer, and J. Weissmüller. Approaching the theoretical strength in nanoporous Au. *Applied Physics Letters*, 89(6):061920, 2006.

[86] J. Zhu, E. Seker, H. Bart-Smith, M. R. Begley, R. G. Kelly, G. Zangari, W.-K. Lye, and M. L. Reed. Mitigation of tensile failure in released nanoporous metal microstructures via thermal treatment. *Applied Physics Letters*, 89(13):133104, 2006.

[87] D. Lee, X. Wei, X. Chen, M. Zhao, J. Hone, E. G. Herbert, W. C. Oliver, and J. W. Kysar. Microfabrication and mechanical properties of nanoporous gold at the nanoscale. *Scripta Materialia*, 56(5):437–440, 2007.

[88] E. Andrews, W. Sanders, and L. J. Gibson. Compressive and tensile behaviour of aluminum foams. *Materials Science and Engineering: A*, 270(2):113–124, 1999.

[89] L. J. Gibson and M. F. Ashby. *Cellular solids: structure and properties*. Cambridge solid state science series. Cambridge University Press, 2nd edition, 1997.

[90] R.N. Viswanath, S.R. Polaki, R. Rajaraman, S. Abhaya, V.A. Chirayath, G. Amarendra, and C.S. Sundar. On the scaling behavior of hardness with ligament diameter of nanoporous Au: Constrained motion of dislocations along the ligaments. *Applied Physics Letters*, 104(23), 2014.

[91] L.A. Zepeda-Ruiz, B. Sadigh, J. Biener, A.M. Hodge, and A.V. Hamza. Mechanical response of freestanding Au nanopillars under compression. *Applied Physics Letters*, 91 (10), 2007.

[92] J. Biener, A. M. Hodge, and A. V. Hamza. Microscopic failure behavior of nanoporous gold. *Applied Physics Letters*, 87(12):121908, 2005.

[93] T. J. Balk, Ch. Eberl, Y. Sun, K. J. Hemker, and D. S. Gianola. Tensile and compressive microspecimen testing of bulk nanoporous gold. *JOM*, 61(12):26–31, 2009.

[94] H.-J. Jin, L. Kurmanaeva, J. Schmauch, H. Rösner, Y. Ivanisenko, and J. Weissmüller. Deforming nanoporous metal: Role of lattice coherency. *Acta Materialia*, 57(9):2665–2672, 2009.

[95] Y. Sun, J. Ye, Z. Shan, A. M. Minor, and T. J. Balk. The mechanical behavior of nanoporous gold thin films. *JOM*, 59(9):54–58, 2007.

[96] R. Dou and B. Derby. Deformation mechanisms in gold nanowires and nanoporous gold. *Philosophical Magazine*, 91(7-9):1070–1083, 2011.

[97] X.-Y. Sun, G.-K. Xu, X. Li, X.-Q. Feng, and H. Gao. Mechanical properties and scaling laws of nanoporous gold. *Journal of Applied Physics*, 113(2):023505, 2013.

[98] D. Farkas, A. Caro, E. Bringa, and D. Crowson. Mechanical response of nanoporous gold. *Acta Materialia*, 61(9):3249–3256, 2013.

[99] B.-N. D. Ngô, A. Stukowski, N. Mameka, J. Markmann, K. Albe, and J. Weissmüller. Anomalous compliance and early yielding of nanoporous gold. *Acta Materialia*, 93: 144–155, 2015.

[100] E. Seker, J.T. Gaskins, H. Bart-Smith, J. Zhu, M.L. Reed, G. Zangari, R. Kelly, and M.R. Begley. The effects of post-fabrication annealing on the mechanical properties of freestanding nanoporous gold structures. *Acta Materialia*, 55(14):4593–4602, 2007.

[101] E. Seker, J.T. Gaskins, H. Bart-Smith, J. Zhu, M.L. Reed, G. Zangari, R. Kelly, and M.R. Begley. The effects of annealing prior to dealloying on the mechanical properties of nanoporous gold microbeams. *Acta Materialia*, 56(3):324–332, 2008.

[102] A. Mathur and J. Erlebacher. Size dependence of effective Young's modulus of nanoporous gold. *Applied Physics Letters*, 90(6):061910, 2007.

[103] A.M. Hodge, R.T. Doucette, M.M. Biener, J. Biener, O. Cervantes, and A.V. Hamza. Ag effects on the elastic modulus values of nanoporous Au foams. *Journal of Materials Research*, 24(04):1600–1606, 2009.

[104] X.-Q. Feng, R. Xia, X. Li, and B. Li. Surface effects on the elastic modulus of nanoporous materials. *Applied Physics Letters*, 94(1):011916, 2009.

[105] R. Xia, X. Li, Q. Qin, J. Liu, and X.-Q. Feng. Surface effects on the mechanical properties of nanoporous materials. *Nanotechnology*, 22(26):265714, 2011.

[106] Z. X. Lu, C. G. Zhang, Q. Liu, and Z. Y. Yang. Surface effects on the mechanical properties of nanoporous materials. *Journal of Physics D-Applied Physics*, 44(39):395404, 2011.

[107] P. Simon and Y. Gogotsi. Materials for electrochemical capacitors. *Nature Materials*, 7 (11):845–854, 2008.

[108] J. Lipkowski, Z. Shi, A. Chen, B. Pettinger, and Ch. Bilger. Ionic adsorption at the Au(111) electrode. *Electrochimica Acta*, 43(19-20):2875–2888, 1998.

[109] N. Huber, R. N. Viswanath, N. Mameka, J. Markmann, and J. Weißmüller. Scaling laws of nanoporous metals under uniaxial compression. *Acta Materialia*, 67(0):252–265, 2014.

[110] W.W. Mullins. Solid surface morphologies governed by capillarity. In *Metal Surfaces: Structure, Energetics and Kinetics, papers presented at a joint seminar of the American Society for Metals and the Metallurgical Society of AIME, October 27 and 28, 1962*, pages 17–66. Metals Park, Ohio, American Society for Metals, 1963.

[111] H.J. Butt, K. Graf, and M. Kappl. *Physics and Chemistry of Interfaces*. Wiley, 2013.

[112] J. Weissmüller and D. Kramer. Balance of force at curved solid metal-liquid electrolyte interfaces. *Langmuir*, 21(10):4592–4603, 2005.

[113] W. Haiss. Surface stress of clean and adsorbate-covered solids. *Reports on Progress in Physics*, 64(5):591–648, 2001.

[114] D. Sander and H. Ibach. 4.4 Surface free energy and surface stress. In A.P. Bonzel, editor, *Adsorbed Layers on Surfaces. Part 2: Measuring Techniques and Surface Properties Changed by Adsorption*, volume 42A2 of *Landolt-Börnstein – Group III Condensed Matter*, pages 303–312. Springer Berlin Heidelberg, 2002.

[115] John W. Cahn. Thermodynamics of solid and fluid surfaces. In *The Selected Works of John W. Cahn*, pages 379–399. John Wiley & Sons, Inc., 2013.

[116] H. P. Bonzel and A. Emundts. Absolute values of surface and step free energies from equilibrium crystal shapes. *Physical Review Letters*, 84:5804–5807, 2000.

[117] E.I. Gershman and S.N. Zhevnenko. Method of *in situ* measuring surface tension of a solid-gas interface. *The Physics of Metals and Metallography*, 110(1):102–107, 2010.

[118] L. Vitos, A.V. Ruban, H.L. Skriver, and J. Kollár. The surface energy of metals. *Surface Science*, 411(1–2):186–202, 1998.

[119] H. Udin, A.J. Schaler, and J. Wulff. The surface tension of solid copper. *Transactions of the American Institute of Mining and Metallurgical Engineers*, 185(2):186–190, 1949.

[120] F. H. Buttner, H. Udin, and J. Wulff. The surface tension of solid gold. *Transactions of the American Institute of Mining and Metallurgical Engineers*, 191(12):1209–1211, 1951.

[121] V.K. Kumikov and Kh.B. Khokonov. On the measurement of surface free energy and surface tension of solid metals. *Journal of Applied Physics*, 54(3):1346–1350, 1983.

[122] H. Udin. *Surface tension of solid copper*. PhD thesis, Massachusetts Institute of Technology, 1949.

[123] S. Swaminarayan, R. Najafabadi, and D.J. Srolovitz. Polycrystalline surface properties from spherical crystallites: Ag, Au, Cu and Pt. *Surface Science*, 306(3):367–380, 1994.

[124] C.R. Weinberger and W. Cai. Plasticity of metal nanowires. *Journal of Materials Chemistry*, 22(8):3277–3292, 2012.

[125] W.R. Tyson and W.A. Miller. Surface free energies of solid metals: Estimation from liquid surface tension measurements. *Surface Science*, 62(1):267–276, 1977.

[126] M. E. Gurtin and A. I. Murdoch. Continuum theory of elastic-material surfaces. *Archive for Rational Mechanics and Analysis*, 57(4):291–323, 1975.

[127] J. Weissmüller and J. W. Cahn. Mean stresses in microstructures due to interface stresses: A generalization of a capillary equation for solids. *Acta Materialia*, 45(5): 1899–1906, 1997.

[128] H.L. Duan, J. Wang, B.L. Karihaloo, and Z.P. Huang. Nanoporous materials can be made stiffer than non-porous counterparts by surface modification. *Acta Materialia*, 54 (11):2983–2990, 2006.

[129] P. Müller. Fundamentals of stress and strain at the nanoscale level: Toward nanoelasticity. In *Mechanical Stress on the Nanoscale*, pages 27–59. Wiley VCH, 2011.

[130] H.C. Gatos and J. Lagowski. Space charge layers. In R.M. Latanision and J.T. Fourie, editors, *Surface effects in crystal plasticity*, Series E: Applied Science – No. 17, pages 221–300. Noordhoff International Publishing, 1977.

[131] H. Ibach. *Physics of surfaces and interfaces*. Springer, Berlin, 2006.

[132] W. Schmickler and E. Santos. *Interfacial electrochemistry, 2nd ed.* Springer, Berlin, 2010.

[133] C. G. Zoski, editor. *Handbook of Electrochemistry.* Elsevier, 2007.

[134] A. J. Bard and L. R. Faulkner. *Electrochemical Methods: Fundamentals and Applications.* John Wiley & Sons, 2001.

[135] W. Haiss. *Charakterisierung elektrochemisch erzeugter Adsorbatschichten auf Goldeinkristalloberflächen mit Hilfe der in situ Rastertunnelmikroscopie.* PhD thesis, Technische Universität Berlin, 1994.

[136] M. Smetanin, R. N. Viswanath, D. Kramer, D. Beckmann, T. Koch, L. A. Kibler, D. M. Kolb, and J. Weissmüller. Surface stress-charge response of a (111)-textured gold electrode under conditions of weak ion adsorption. *Langmuir*, 24(16):8561–8567, 2008.

[137] R. N. Viswanath, D. Kramer, and J. Weissmüller. Variation of the surface stress-charge coefficient of platinum with electrolyte concentration. *Langmuir*, 21(10):4604–4609, 2005.

[138] R. Shuttleworth. The surface tension of solids. *Proceedings of the Physical Society of London Section A*, 63(365):444–457, 1950.

[139] A. Dursun, D.V. Pugh, and S.G. Corcoran. Dealloying of Ag-Au alloys in halide-containing electrolytes. Affect on critical potential and pore size. *Journal of the Electrochemical Society*, 150(7):B355–B360, 2003.

[140] B. E. Conway. Electrochemical oxide film formation at noble-metals as a surface-chemical process. *Progress in Surface Science*, 49(4):331–452, 1995.

[141] D. Cattarin, S.and Kramer, A. Lui, and M. M. Musiani. Preparation and characterization of gold nanostructures of controlled dimension by electrochemical techniques. *The Journal of Physical Chemistry C*, 111(34):12643–12649, 2007.

[142] *NOVA Getting started. User manual.* Metrohm Autolab, 2013.

[143] R.G. Kelly, A.J. Young, and R.C. Newman. Characterization of the coarsening of dealloyed layers by EIS and its correlation with stress-corrosion cracking. In *ASTM Special Technical Publication*, number 1188, pages 94–112, 1993.

[144] S. Cattarin, D. Kramer, A. Lui, and M. Musiani. Formation of nanostructured gold sponges by anodic dealloying. EIS investigation of product and process. *Fuel Cells*, 9 (3):209–214, 2009.

[145] E. Rouya, S. Cattarin, M. L. Reed, R. G. Kelly, and G. Zangari. Electrochemical characterization of the surface area of nanoporous gold films. *Journal of The Electrochemical Society*, 159(4):K97–K102, 2012.

[146] J. Erlebacher, M.J. Aziz, A. Karma, N. Dimitrov, and K. Sieradzki. Evolution of nanoporosity in dealloying. *Nature*, 410(6827):450–453, 2001.

[147] F. Kertis, J. Snyder, L. Govada, S. Khurshid, N. Chayen, and J. Erlebacher. Structure processing relationships in the fabrication of nanoporous gold. *JOM*, 62(6):50–56, 2010.

[148] J. Erlebacher. An atomistic description of dealloying porosity evolution, the critical potential, and rate-limiting behavior. *Journal of the Electrochemical Society*, 151(10): C614–C626, 2004.

[149] L. Chen, X. Lang, and M. Chen. Dealloyed nanoporous metals. In Q. Xu, editor, *Nanoporous Materials: Synthesis and Applications*, chapter 5, pages 125–182. CRC Press, 2013.

[150] B. G. Ateya, F. M. Al-Kharafi, and F. M. Bayoumi. Selective corrosion of alloys. unpublished, 2014. URL http://www.researchgate.net/publication/228709942_Selective_Corrosion_of_Alloys.

[151] H. Goebel and P. von Blanckenhagen. Study of surface diffusion on gold with an atomic force microscope. *Surface Science*, 331-333(pt B):885–890, 1995.

[152] M. Giesen, G. Beltramo, S. Dieluweit, J. Müller, H. Ibach, and W. Schmickler. The thermodynamics of electrochemical annealing. *Surface Science*, 595(1-3):127–137, 2005.

[153] A. J. Forty and P. Durkin. A micromorphological study of the dissolution of silver-gold alloys in nitric acid. *Philosophical Magazine A*, 42(3):295–318, 1980.

[154] N.A. Senior and R.C. Newman. Synthesis of tough nanoporous metals by controlled electrolytic dealloying. *Nanotechnology*, 17(9):2311–2316, 2006.

[155] M. Smetanin, Q. Deng, D. Kramer, S. Mohanan, U. Herr, and J. Weissüller. Reply to the 'Comment on "Response of the potential of a gold electrode to elastic strain" by Á. Horváth, G. Nagy and R. Schiller, Phys. Chem. Chem. Phys., 2010, 12'. *Physical Chemistry Chemical Physics*, 12(26):7291–7292, 2010.

[156] M. Pourbaix, editor. *Atlas of electrochemical equilibria in aqueous solutions*. Pergamon Press, 1966.

[157] Y. Zhong, J. Markmann, H.-J. Jin, Y. Ivanisenko, L. Kurmanaeva, and J. Weissmüller. Crack mitigation during dealloying of $Au_{25}Cu_{75}$. *Advanced Engineering Materials*, 16 (4):389–398, 2014.

[158] S. Trasatti and O.A. Petrii. Real surface area measurements in electrochemistry. *Journal of Electroanalytical Chemistry*, 327(1-2):353–376, 1992.

[159] P.S. Germain, W.G. Pell, and B.E. Conway. Evaluation and origins of the difference between double-layer capacitance behaviour at Au-metal and oxidized Au surfaces. *Electrochimica Acta*, 49(11):1775–1788, 2004.

[160] J.O'M. Bockris, S.D. Argade, and E. Gileadi. The determination of the potential of zero charge on solid metals. *Electrochimica Acta*, 14(12):1259–1283, 1969.

[161] G.J. Clark, T.N. Andersen, R.S. Valentine, and H. Eyring. Comparison of the immersion and open-ciruit scrape methods for determining the potential of zero charge of metal electrodes. *Journal of the Electrochemical Society*, 121(5):618–622, 1974.

[162] Standard test method for Young's modulus, tangent modulus, and chord modulus, 2004.

[163] P.-A. Eggertsen and K. Mattiasson. On the modeling of the unloading modulus for metal sheets. *International Journal of Material Forming*, 3(SUPPL. 1):127–130, 2010.

[164] R.N. Viswanath and J. Weissmüller. Electrocapillary coupling coefficients for hydrogen electrosorption on palladium. *Acta Materialia*, 61(16):6301–6309, 2013.

[165] Y. C. K. Chen-Wiegart, S. Wang, W. Chu, Y. S.and Liu, I. McNulty, P. W. Voorhees, and D. C. Dunand. Structural evolution of nanoporous gold during thermal coarsening. *Acta Materialia*, 60(12):4972–4981, 2012.

[166] K. Hu, M. Ziehmer, K. Wang, and E. T. Lilleodden. Investigation of the coarsening behaviour of nanoporous gold based on representative volumes. In *79th Annual Meeting of the DPG and DPG-Frühjahrstagung of the Condensed Matter Section (SKM)*. Deutsche Physikalische Gesellschaft e. V., March 15 – 20, 2015. URL http://www.dpg-verhandlungen.de/year/2015/conference/berlin/part/mm/session/52/contribution/3.

[167] K. Wang and J. Weissmüller. Composites of nanoporous gold and polymer. *Advanced Materials*, 25(9):1280–1284, 2013.

[168] N.J. Briot, T. Kennerknecht, C. Eberl, and T.J. Balk. Mechanical properties of bulk single crystalline nanoporous gold investigated by millimetre-scale tension and compression testing. *Philosophical Magazine*, 94(8):847–866, 2014.

[169] N. Mameka, J. Markmann, H.-J. Jin, and J. Weissmüller. Electrical stiffness modulation – Confirming the impact of surface excess elasticity on the mechanics of nanomaterials. *Acta Materialia*, 76:272–280, 2014.

[170] D. M. Kolb and J. Schneider. Surface reconstruction in electrochemistry – Au(100)-(5x20), Au(111)-(1x23) and Au(110)-(1x2). *Electrochimica Acta*, 31(8):929–936, 1986.

[171] L. H. Shao, H.-J. Jin, R. N. Viswanath, and J. Weissmüller. Different measures for the capillarity-driven deformation of a nanoporous metal. *Europhysics Letters*, 89(6):66001, 2010.

[172] R. Liu and A. Antoniou. A relationship between the geometrical structure of a nanoporous metal foam and its modulus. *Acta Materialia*, 61(7):2390–2402, 2013.

[173] O. M. Magnussen. Ordered anion adlayers on metal electrode surfaces. *Chemical Reviews*, 102(3):679–726, 2002.

[174] H. Angerstein-Kozlowska, B.E. Conway, A. Hamelin, and L. Stoicoviciu. Elementary steps of electrochemical oxidation of single-crystal planes of Au. Part I. Chemical basis of processes involving geometry of anions and the electrode surfaces. *Electrochimica Acta*, 31(8):1051–1061, 1986.

[175] A. J. Bard, G. Inzelt, and F. Scholz, editors. *Electrochemical Dictionary, 2nd ed.* Springer, Berlin, 2012.

[176] H. Angerstein-Kozlowska, B.E. Conway, B. Barnett, and J. Mozota. The role of ion adsorption in surface oxide formation and reduction at noble metals: General features of the surface process. *Journal of Electroanalytical Chemistry and Interfacial Electrochemistry*, 100(1–2):417–446, 1979.

[177] M.J. Nicol. The anodic behaviour of gold. Part I. Oxidation in acidic solutions. *Gold Bulletin*, 13(2):46–55, 1980.

[178] A. Hamelin. Cyclic voltammetry at gold single-crystal surfaces. Part 1. Behaviour at low-index faces. *Journal of Electroanalytical Chemistry*, 407(1-2):1–11, 1996.

[179] D.D. Bodé Jr., T. N. Adersen, and H. Eyring. Anion and pH effects on the potentials of zero charge of gold and silver electrodes. *Journal of Physical Chemistry*, 71(4):792–797, 1967.

[180] Z. Shi, J. Lipkowski, M. Gamboa, P. Zelenay, and A. Wieckowski. Investigations of SO_4^{2-} adsorption at the Au(111) electrode by chronocoulometry and radiochemistry. *Journal of Electroanalytical Chemistry*, 366(1-2):317–326, 1994.

[181] J. Weissmüller, H.-L. Duan, and D. Farkas. Deformation of solids with nanoscale pores by the action of capillary forces. *Acta Materialia*, 58(1):1–13, 2010.

[182] D. A. Crowson, D. Farkas, and S. G. Corcoran. Mechanical stability of nanoporous metals with small ligament sizes. *Scripta Materialia*, 61(5):497–499, 2009.

[183] L. Thilly, S.V. Petegem, P.-O. Renault, F. Lecouturier, V. Vidal, B. Schmitt, and H. Van Swygenhoven. A new criterion for elasto-plastic transition in nanomaterials: Application to size and composite effects on Cu-Nb nanocomposite wires. *Acta Materialia*, 57(11):3157–3169, 2009.

[184] L. J. Gibson and M. F. Ashby. The mechanics of three-dimensional cellular materials. *Proceedings of the Royal Society of London. A. Mathematical and Physical Sciences*, 382 (1782):43–59, 1982.

[185] A.M. Hodge and J. T. Balk. Mechanical properties of nanoporous gold. In A. Wittstock, J. Biener, J. Erlebacher, and M. Bäumer, editors, *Nanoporous Gold: From an Ancient Technology to a High-Tech Material*, RSC Nanoscience & Nanotechnology No. 22, chapter 4, pages 51–68. The Royal Society of Chemistry, 2012.

[186] J. Rajagopalan and M.T. A. Saif. Effect of microstructural heterogeneity on the mechanical behavior of nanocrystalline metal films. *Journal of Materials Research*, 26: 2826–2832, 11 2011.

[187] J. Lohmiller, R. Baumbusch, O. Kraft, and P. A. Gruber. Differentiation of deformation modes in nanocrystalline Pd films inferred from peak asymmetry evolution using *in situ* x-ray diffraction. *Physical Review Letters*, 110:066101, 2013.

[188] L. Thilly, P. O. Renault, S. Van Petegem, S. Brandstetter, B. Schmitt, H. Van Swygenhoven, V. Vidal, and F. Lecouturier. Evidence of internal Bauschinger test in nanocomposite wires during *in situ* macroscopic tensile cycling under synchrotron beam. *Applied Physics Letters*, 90(24):241907, 2007.

[189] J. Rajagopalan, J. H. Han, and M. T. A. Saif. Plastic deformation recovery in freestanding nanocrystalline aluminum and gold thin films. *Science*, 315(5820):1831–1834, 2007.

[190] L. Li, P. M. Anderson, M.-G. Lee, E. Bitzek, P. Derlet, and H. Van Swygenhoven. The stress-strain response of nanocrystalline metals: A quantized crystal plasticity approach. *Acta Materialia*, 57(3):812–822, 2009.

[191] M. E. Gurtin, J. Weissmüller, and F. Larché. A general theory of curved deformable interfaces in solids at equilibrium. *Philosophical Magazine a-Physics of Condensed Matter Structure Defects and Mechanical Properties*, 78(5):1093–1109, 1998.

[192] J. J. Métois, A. Saúl, and P. Müller. Measuring the surface stress polar dependence. *Nature Materials*, 4(3):238–242, 2005.

[193] P. Nozières and D. E. Wolf. Interfacial properties of elastically strained materials.1. Thermodynamics of a planar interface. *Zeitschrift Für Physik B-Condensed Matter*, 70 (3):399–407, 1988.

[194] S. P. Timoshenko and J. N. Goodier. *Theory of Elasticity*. McGraw-Hill, New York, 2nd edition, 1951.

[195] R. J. Nichols, T. Nouar, C. A. Lucas, W. Haiss, and W. A. Hofer. Surface relaxation and surface stress of Au(111). *Surface Science*, 513(2):263–271, 2002.

[196] Y. Umeno, C. Elsaesser, B. Meyer, P. Gumbsch, and J. Weissmüller. Reversible relaxation at charged metal surfaces: An ab initio study. *Europhysics Letters*, 84(1):13002, 2008.

[197] J. M. Albina, C. Elsasser, J. Weissmüller, P. Gumbsch, and Y. Umeno. Ab initio investigation of surface stress response to charging of transition and noble metals. *Physical Review B*, 85(12):125118, 2012.

[198] W. Haiss, R. J. Nichols, J. K. Sass, and K. P. Charle. Linear correlation between surface stress and surface charge in anion adsorption on Au(111). *Journal of Electroanalytical Chemistry*, 452(2):199–202, 1998.

[199] M. Gsell, P. Jakob, and D. Menzel. Effect of substrate strain on adsorption. *Science*, 280(5364):717–720, 1998.

[200] W.X. Zhang, T.J. Wang, and X. Chen. Effect of surface/interface stress on the plastic deformation of nanoporous materials and nanocomposites. *International Journal of Plasticity*, 26(7):957–975, 2010.

[201] B. Hyde, H.D. Espinosa, and D. Farkas. An atomistic investigation of elastic and plastic properties of Au nanowires. *JOM*, 57(9):62–66, 2005.

[202] E. Rabkin and D.J. Srolovitz. Onset of plasticity in gold nanopillar compression. *Nano Letters*, 7(1):101–107, 2007.

[203] J. J. Gilman. The mechanism of surface effects in crystal plasticity. *Philosophical Magazine*, 6(61):159–161, 1961.

[204] W. G. Johnston and J. J. Gilman. Dislocation multiplication in lithium fluoride crystals. *Journal of Applied Physics*, 31(4):632–643, 1960.

[205] J. Weissmüller. Nanoscale mechanical behavior: Role of capillarity. In *MRS Fall Meeting*, Boston, MA, USA, 30 November – 5 December 2014.

[206] R. Bullough. Microplasticity. In R.M. Latanision and J.T. Fourie, editors, *Surface effects in crystal plasticity*, Series E: Applied Science – No. 17, pages 321–381. Noordhoff International Publishing, 1977.

[207] R.M. Latanision. Surface effects in crystal plasticity: General overview. In R.M. Latanision and J.T. Fourie, editors, *Surface effects in crystal plasticity*, Series E: Applied Science – No. 17, pages 3–47. Noordhoff International Publishing, 1977.

[208] C. J. van der Wekken. Surface dislocation pinning by adsorbed ions and water molecules. *Journal of The Electrochemical Society*, 131(11):2481–2483, 1984.

[209] M. Yu. Gutkin, S. R. Kalehbasti, and H. M. Shodja. Surface/interface effects on elastic behavior of an edge dislocation in the shell of a core-shell nanowire. *European Journal of Mechanics - A/Solids*, 41(0):86–100, 2013.

[210] H. Ahmadzadeh-Bakhshayesh, M. Yu. Gutkin, and H. M. Shodja. Surface/interface effects on elastic behavior of a screw dislocation in an eccentric core-shell nanowire. *International Journal of Solids and Structures*, 49(13):1665–1675, 2012.

Publications & Conferences

Publications

1. N. Huber, R.N. Viswanath, N. Mameka, J. Markmann, and J. Weißmüller.
Scaling laws of nanoporous metals under uniaxial compression.
Acta Materialia, 67, 252-265 (2014).

2. N. Mameka, J. Markmann, H.-J. Jin, and J. Weissmüller.
Electrical stiffness modulation – Confirming the impact of surface excess elasticity on the mechanics of nanomaterials.
Acta Materialia, 76, 272-280 (2014).

3. B.-N. D. Ngô, A. Stukowski, N. Mameka, J. Markmann, K. Albe, and J. Weissmüller.
Anomalous compliance and early yielding of nanoporous gold.
Acta Materialia, 93, 144-155 (2015).

4. N. Mameka, K. Wang, J. Markmann, E. T. Lilleodden, and J. Weissmüller.
Nanoporous gold – Testing macro-scale samples to probe small-scale mechanical behavior.
Materials Research Letters, 4, 27-36 (2016).

Conference contributions

1. N. Mameka, J. Markmann, and J. Weissmüller.
Study of viscoelastic properties of nanoporous gold using dynamic mechanical analysis.
Poster presentation.
76th Annual Meeting of the DPG and DPG Spring Meeting (German Physical Society), 25–30 March 2012, Berlin, Germany.

2. N. Mameka, J. Markmann, and J. Weissmüller.
Study of viscoelastic properties of nanoporous gold using dynamic mechanical analysis.
Poster presentation.
3rd International Conference on Multifunctional, Hybrid & Nanomaterials, 3–7 March 2013, Sorrento, Italy.

3. N. Mameka, J. Markmann, and J. Weissmüller.
Elastic and plastic behavior of nanoporous gold as a function of the surface state.
Oral presentation.
DPG Spring Meeting (German Physical Society), 10–15 March 2013, Regensburg, Germany.

4. N. Mameka, J. Markmann, and J. Weissmüller.
   Surface excess elasticity in nanostructures: Fact or fiction?
   Oral presentation.
   DPG Spring Meeting (German Physical Society), 30 March–4 April 2014, Dresden, Germany.

5. N. Mameka, J. Markmann, and J. Weissmüller.
   Elasticity and plasticity of nanoporous metals can be tuned by electric potentials.
   Poster presentation (best poster award).
   Gordon Research Conference on Thin Film & Small Scale Mechanical Behavior, 13–18 July 2014, Waltham, MA, USA.

6. N. Mameka, J. Markmann, and J. Weissmüller.
   Elasticity and plasticity of nanoporous metals can be tuned by electric potentials.
   Oral presentation.
   1st International Symposium on Nanoporous Materials by Alloy Corrosion, 28 September–2 October 2014, Bosen, Germany.

7. N. Mameka, J. Markmann, and J. Weissmüller.
   ***In situ* mechanical testing of nanoporous gold: New insights into plasticity of nanostructures.**
   Oral presentation.
   79th Annual Meeting of the DPG and DPG Spring Meeting (German Physical Society), 15–20 March 2015, Berlin, Germany.

8. N. Mameka and J. Markmann.
   Mechanical behaviour of nanoporous gold can be controlled by surface modification.
   Oral presentation (invited talk).
   4th International Symposium on Energy Challenges and Mechanics (ECM4) – Working on small scales, 11–13 August 2015, Aberdeen, Scotland, UK.